UNIVERSIDADE FEDERAL DE SÃO CARLOS
CENTRO DE CIÊNCIAS EXATAS E DE TECNOLOGIA
DEPARTAMENTO DE QUÍMICA
PROGRAMA DE PÓS-GRADUAÇÃO EM QUÍMICA

Deposição de Nanocristais Coloidais: da Síntese à Aplicação na Fotoeletroquímica da Oxidação da Água

Ricardo H. Gonçalves

Tese apresentada como parte dos requisitos para obtenção do título de DOUTOR(A) EM CIÊNCIAS, área de concentração: Físico-Química

Orientador: Edson R. Leite

São Carlos - SP
2016

UNIVERSIDADE FEDERAL DE SÃO CARLOS
CENTRO DE CIÊNCIAS EXATAS E DE TECNOLOGIA
DEPARTAMENTO DE QUÍMICA
PROGRAMA DE PÓS-GRADUAÇÃO EM QUÍMICA

Colloidal Nanocrystals Deposition: From the Synthesis to the Application in Photoeletrochemistry Water Splitting

Ricardo H. Gonçalves

Submitted in Partial Fulfillment of the Requirements for the Degree of Doctor of Philosophy

Supervisor: Edson R. Leite

São Carlos - SP
2016

Ficha catalográfica elaborada pelo DePT da Biblioteca Comunitária UFSCar
Processamento Técnico
com os dados fornecidos pelo(a) autor(a)

Gonçalves, Ricardo Henrique
G635c Colloidal Nanocrystals Deposition : from the synthesis to the application in photoeletrochemistry water splitting / Ricardo Henrique Gonçalves. -- São Carlos : UFSCar, 2016.
101 p.

Tese (Doutorado) -- Universidade Federal de São Carlos, 2016.

1. Electrochemistry. 2. Hematite. 3. Nanocrystals. 4. Photoeletrochemistry. 5. Microscopy. I. Título.

UNIVERSIDADE FEDERAL DE SÃO CARLOS

Centro de Ciências Exatas e de Tecnologia
Programa de Pós-Graduação em Química

Folha de Aprovação

Assinaturas dos membros da comissão examinadora que avaliou e aprovou a Defesa de Tese de Doutorado do candidato Ricardo Henrique Gonçalves, realizada em 24/05/2016:

Prof. Dr. Edson Roberto Leite
UFSCar

Prof. Dr. Koiti Araki
USP

Prof. Dr. Romeu Cardozo Rocha Filho
UFSCar

Profa. Dra. Daniela Zanchet
UNICAMP

Prof. Dr. Caio Marcio Paranhos da Silva
UFSCar

Colloidal Nanocrystals Deposition: From the Synthesis to the Application in Photoeletrochemistry Water Splitting

Abstract. An excellent and potentially efficient route towards storing solar energy is to convert light into chemical energy in the form of chemical bonds, which is a form of artificial photosynthesis. Considering the abundance of H_2O on the planet, water splitting is a natural pathway for artificial photosynthesis. Hematite is a n-type semiconductor with high chemical stability in alkaline media and promising material for photoelectrochemical water splitting. This thesis describes critical parameters involved in the Colloidal Nanocrystals Deposition (CND) process to produce hematite photoanodes with high efficiency for solar-to-hydrogen conversion.

In chapter 2, a fundamental study reveals that the interface solid-solid is a parameter that has strong influence on the performance of the photoanode. The gap between the FTO substrate and hematite thin film was observed by HRTEM images and it can be overcome during a sintering stage. In the this same chapter, the solid-solid interface analysis was correlated with the photoresponse and it has showed that hematite thin film treated at 1000 ºC also improved the response of this photoande. This result was explained based on the grain growth and associated with the mass distribution on the FTO surface.

In chapter 3, the CND process was improved using a magnet to assist the nanocrystals deposition and the oxidation of magnetite (Fe_3O_4) to maghemite (γ-Fe_2O_3) to avoid the presence of Fe^{2+}. In this approach, Sn was used as a doping element and has showed a significant improve on the photoresponse of the hematite. The STEM-EDS analysis showed that Sn has the ability to segregate on the hematite grain boundary during sintering process at high temperature, avoiding grain growth.

The results showed in chapter 4 were essential to understand the thickness effect on the photocurrent of thin film produced by CND process. In this case, changing the nanocrystals concentration has direct effect on the thickness of the hematite thin film. The FTO roughness also showed significant influence on the orientation of hematite grain along the direction <110>. In this study, was possible to calculate the maximum theoretical efficiency for the hematite photoanode obtained by this method. The thickness control and homogeneity of the thin film give a great perspective for technological application of this process.

The *in situ* heating TEM demonstrated that nanocrystals has abnormal grain growth and also a superplastic phenomenon, as revealed in chapter 5. In this chapter, Sn was deposited on γ-Fe_2O_3 impeding atom dislocation on the grain boundary and consequently inhibits the growth process. This experiment was an approach to mimic the sintering process performed in the CND process.

The electrocatalyst described in chapter 6 has shown to be promising for OER. The strategy to use a Prussian blue analogue to deposit a thin layer of nickel-iron hexacyanoferrate and convert into nickel-iron oxyhydroxide has led to an excellent homogeneity and low overpotential for OER. This result is comparable with IrO_2 and RuO_2 that are electrocatalysts with high electrochemical performance. Catalyst supports were also evaluated, such as FTO, palladium and PGS. The PGS substrate has been an excellent support for this purpose and led to results comparable to palladium substrate.

TABLE OF CONTENTS

List of Figures

List of Table

List of Abbreviations and Symbols

Abbreviations

ADF	annular dark field
ALD	atomic layer deposition
ATO	antimony tin oxide
AM 1.5	air mass solar simulation
BF	bright field
APCVD	atmospheric pressure chemical vapor deposition
CND	colloidal nanocrystals deposition
DSA	dimensionally stable anode
EDS	energy dispersive X-ray spectroscopy
EIS	electrochemical impedance spectroscopy
FE	field emission
FIB	focus ion beam
FF	fill factor
FTO	fluorine doped tin oxide
HRTEM	high Resolution Transmission Electron Microscopy
HER	hydrogen evolution reaction
IGT	institute of Gas Technology
IPCE	incident photon to current efficiency
JCPDS	joint Committee on Powder Diffraction Standards
ND	donor density
OER	oxygen evolution reaction
PEC	photoelectrochemical cell
PLD	pulsed Laser deposition
PGS	pyrolytic Graphite Sheet
PTFE	polytetrafluoroethene
PV	photovoltaic panel
RHE	reversible hydrogen electrode
SCLJ	semiconductor-liquid junction
SC	space charge
SEM	scanning electron microscopy
SR	steam reforming
STEM	scanning transmission electron microscopy
TCO	transparent conductive oxide
TEM	transmission electron Microscopy
Uv-vis	ultraviolet –Visible light spectrum
XRD	X ray diffraction

Symbols

Symbol	Definition
L_p	hole diffusion length
$i_{ph(w)}$	photocurrent
V_{oc}	open-circuit voltage
E_{ft}	flat-band potential
W	depletion layer
E_i	Fermi level
f(E)	Fermi function
j	current density
D_p	hole diffusion constant
$P_{(w)}$	power density
J_{photo}	photocurrent density
$\varphi_{p,SC}$	lifetime of charge on surface
φ_H	transfer of hole-electron on the interface
φ_{diff}	diffusion of redox particles
η_{abs}	absorption efficiency
η_{bulk}	electron-hole separation yield
$\eta_{surface}$	charge kinetic transfer efficiency
η_{STH}	solar to hydrogen conversion efficiency
η_{redox}	overpotential
V_{RHE}	volts vs. RHE
α	optical absorption
ϕ	incident photon flux
L_p	hole diffusion length
q	elementary charge
μ_{water}	thermodynamic redox potential
V_{op}	operational potential
iR_{cell}	cell resistance potential
P_{light}	solar irradiance
T	Tesla
h^+	holes at the potential of the Fermi level in the electrode

Acknowledgements

In this thesis, I would like to perpetuate the research that I sincerely believe that have relevant information and also include the name of people that made fundamental contribution for me. Thus, I need to express my sincere acknowledgements. First, I would like to thank Professor Edson R. Leite and Thomas E. Mallouk that permitted me to work in their group and gave me all the freedom to find my real challenge, trusting in my ability and creativity.

During the laboratory life, I figured out that friendship is the most valuable contribution to get success and life experience. Thus, I thank the undergraduate students who worked with me, Rafael Zerbinatti, Renato, Rodrigo Fiel, Lucas and Gustavo. I would like also to acknowledge Mario Soares for the collaborative work, discussions and comments. I would like to thank Renata S. Lang and Rocio E. Rojas-Hernandez for being a great collaborator and friendship. I thank Johanna Engel for those precious discussions about hematite photoanode.

Many students and staffs of LIEC have provided me a friendship during the coffee break. This list includes Ademir, Adriano, Barbosa, Bruno, Cintia, Cleocir, Edney, Fernando, Julio, Laecio, Marco, Mateus, Narcisio, Roman, Rorivaldo, Tatiane, and Tiago.

As a visiting student at Penn State University I had the opportunity to find nice people like, Chris Li, Nick Mccool, Erik Jewell, Tao, Dekai, Ritash, Chris, An, Alisya and Kelvin. Thank you very much for sharing your knowledge, friendship and patience with my speaking limitation.

I cannot forget to thank my friends of Maringa State University, Guilherme Miranda, Thelma, Rafael Silva and Fernando Carvalho.

I am grateful to Brandon Merket for teaching me English and little bit of the American culture. We had many funny days of fishing, playing billiard and buying junk food on Walmart.

Finally, it is pleasure to mention Amarilis de Moraes, as a special girl that gave me an important support and have understood the essence of this challenge in my life. It has been a long time living far away and she always gave me motivation to continue studying and finishing this challenge.

Ricardo H. Goncalves
April 2016
Sao Carlos-SP

Chapter 1. General Introduction

1.1 Solar Energy and Hydrogen Fuel

The sun was always a fascinating instrument of nature that drives life and climate conditions in the Earth. It is not an overstatement to say that solar radiation is the source for many secondary energy carriers, such as petroleum, biofuel, hydroelectric and wind power station. It has been a huge challenge to Science and Engineering to develop a sustainable and efficient conversion mechanism, of this solar radiation energy directly into electricity and storage. In the current scenario, photovoltaic panel (PV) have been the most promising technology to collect this solar radiation. The cost of fabrication and installation has been considerably expensive and also has a lack of silicon supplier in the global market. However, PV panel has a lifespan of 25 years.[1] At the same time, the photovoltaic manufacturing has had a significant growth, over past decades, and coming down the production cost of these devices. The enormous progress in this field is the result of substantial investment in solar energy research centers and government subsidies to become this technology commercially competitive.[2-4]

Efficiency and low-cost was always the fundamental parameter in solar energy research. The solar spectral irradiance was a critical parameter developed as a calibrated reference to measure and compare the photovoltaic efficiency.[5] In 1980, the spectral irradiance Air Mass (AM) 1.5 was selected as a standard solar light to be simulated. This decision had as reference a report published by Gonzalez *et al*,[6] showing that 50% of solar spectral irradiance, necessary for photovoltaic operation, occurs above and below standard AM 1.5. The spectrum intensity was measured in reference of solar zenith angle 48.2º, considering 1.5 times the normal path length of the atmosphere.[6,7] Figure 1.1a shows the spectral irradiance versus the wavelength for the standard solar illumination AM 1.5, the integration of this spectrum correspond approximately 100 $mW.cm^{-2}$.[7] Figure 1.1b is a demonstrative schema of spectral irradiance AM 1.5 and AM 1.0.

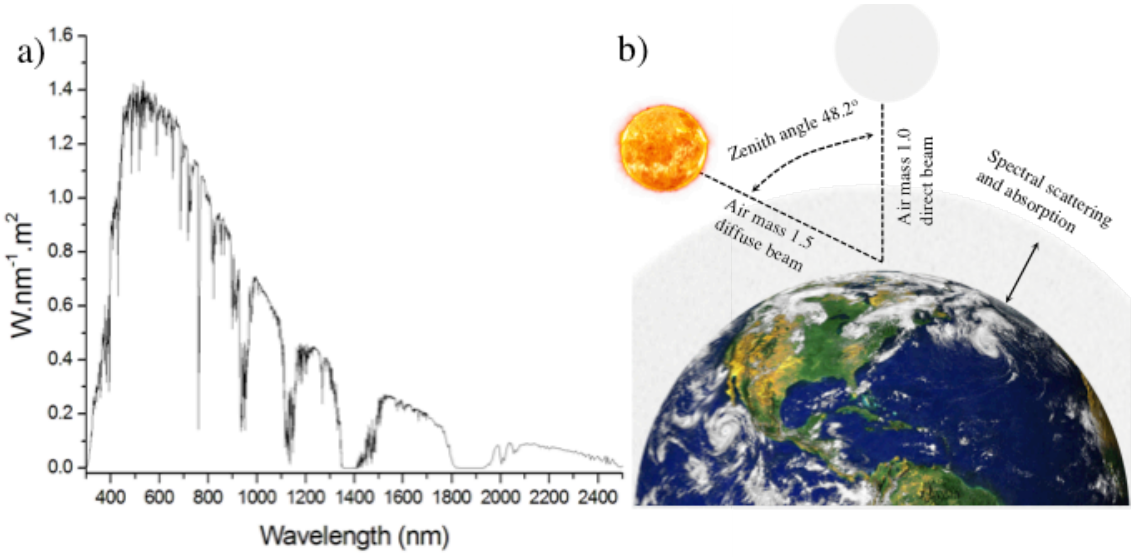

Figure 1.1 Solar radiation transmitted through the atmosphere. a) Standard solar spectral irradiance AM 1.5. b) Illustrative schema of air mass 1.0 and 1.5.

The theoretical solar light to electrical output efficiency of silicon solar cells is thermodynamically limited at 35% and under experimental conditions achieves 25% of efficiency, which became very attractive for electrical power generation. The operational performance of photovoltaic solar cells also depends of weather conditions, season and time of day.[8] Unfortunately, these cells cannot store energy and neither provides a steady supply. For a long time, hydrogen gas and batteries have been mentioned as the most important alternative for energy storage from PV devices.[9] For example, a photovoltaic power station could assist hydrogen gas generation or charge a giant battery. However, there are many fundamental questions to be analyzed in terms of efficiency, cost and environmental impact.

Nowadays, hydrogen gas has been receiving a huge attention as an alternative solution for fossil fuel. Steam reforming (SR) of natural gas has been efficiently used to produce hydrogen gas. This process consists in chemical reacting natural gas, such as methane, with water at high temperatures (700 -1100 ºC).[10] For example, methane molecules react with water molecule to produce carbon monoxide and hydrogen gas. In a second step, carbon monoxide is oxidized in steam to produce more hydrogen gas and carbon dioxide.[11] At low temperature, the excess of water and carbon dioxide is deposited and the hydrogen gas can be easily separated. The substantial cost of hydrogen fuel compared to petroleum has been the main obstacle to overcome.[12] This hydrogen gas has been consumed mainly in the chemical industry, such as ammonia, hydrochloride acid and petrochemical. For this reason, hydrogen gas, as fuel, opens an important economy discussion.[13]

The fossil origin of methane has been a disadvantage of SR and also the tons of carbon dioxide eliminated, as byproduct. The electrolysis of water is considered the most promising process to generate hydrogen gas.[14] Despite two centuries after this discovery,[15-18] there are many technological implications to make this process competitive. Firstly, precious metals, such as platinum, iridium, ruthenium and palladium are efficiently used as anode and cathode.[19] Second, this conventional water electrolysis needs an electrical power source, increasing significantly the cost in comparison with SR process.[20] Third, the storage and transport hydrogen gas require a sophisticated technology to hold high pressures.[21] Currently, the technology behind of hydrogen storage has achieved an excellent performance in terms of safety and cost.[22] In 1974, Exxon and the Institute of Gas Technology (IGT) independently published results of a research to evaluate hydrogen gas as an alternative automobile fuel. Similar results showed that hydrogen fuel only become economically viable when obtained by solar and nuclear energy.[23,24] Thus, the main challenge has been to obtain an efficient process for energy storage via solar-to-hydrogen conversion.

The huge perspective for hydrogen gas has been focused as a renewable energy carrier for fuel cell-electric vehicle.[25] However, the lithium-ion battery has also achieved excellent performance in electrical vehicles, opening a competitiveness discussion about sustainable energy source. What will be the future energy carrier? Hydrogen fuel, battery or biofuel.

1.2 Electrochemistry of Semiconductor Oxide

The important distinction between a semi-metal and a metal under illumination is the stability of photoexcited charges. The electrons of a semiconductor have the ability to absorb photons or thermal energy to promote them to the conduction band and generate electron vacancies in the valence band, called holes (h^+).[26] This electron-hole pair recombination in semiconductors have high lifetime when compared with photoelectrons in metal surface.[27] Semiconductors can be classified as intrinsic and extrinsic. Indeed, intrinsic semiconductors are perfect crystals that have a small fraction of free electrons with a thermal energy to be injected in the conduction band.[28] On the other hand, extrinsic semiconductors have impurities known as doping. This doping process depends crucially of the valence state of the atoms added and they can be classified as N- and P-type semiconductors. For example, if the atom doping has ability to donate electrons or increase the fraction of free electrons in the valence band, then it can be considered N-type

semiconductor. Thus, the majority charge carriers are electrons. On the contrary, in P-type semiconductors, the atoms added have ability to accept electrons and decrease the fraction of free electron, in the valence band. In this case, the majority charge carriers are holes.[28,30]

The Fermi function $f(\varepsilon)$ has been an excellent statistical tool to understand electronic and thermal behavior in semiconductors under equilibrium. $f(\varepsilon)$ is a probabilistic function of energy state (E) that can be occupied by electrons, see equation 1.1. The Fermi level (ε_F) is the energy state that has 1/2 probability to be filled.[31,32]

$$f(E) = \frac{1}{e^{(E-E_F)/kT} + 1} \tag{1.1}$$

For an intrinsic semiconductor, the Fermi level is located in the middle of a band gap. It implies that there is a lower probability of electron jump near the conduction band P-type semiconductor has the Fermi level near to the valence band due to the addition of acceptor doping. For a N-type semiconductor, the Fermi level is relatively higher when compared with intrinsic Fermi level (ε_i) due to the addition of donor doping.[33] It is important to mention that the electrical behavior was the experimental parameter to classify the semiconductors and the Fermi level is the mathematical tool to explain this electrical behavior. Figure 1.2 shows an exacerbated Fermi function plot for the intrinsic and extrinsic semiconductors.

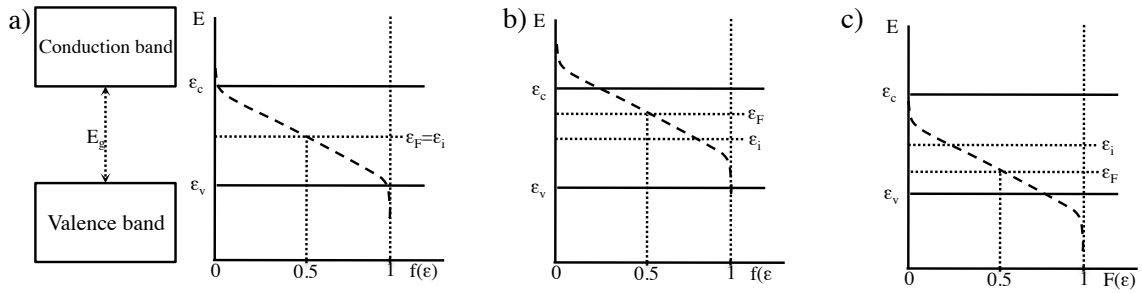

Figure 1.2 Energy level diagram for a semiconductor versus the Fermi-Dirac distribution function. a) Intrinsic semiconductor, b) N-type semiconductor, c) P-type semiconductor.

These definitions of extrinsic semiconductors and the Fermi level are fundamental to estimate the free electron-hole concentration in the conduction and valence band and to explain the photoelectrochemical behavior of these semiconductors in solution. Semiconductor liquid junction (SLJ) is the interface between the semiconductor and the electrolyte. The SLJ equilibrium is established with the alignment of the redox Fermi level of the electrolyte ($\varepsilon_{F/redox}$) and the Fermi level of the semiconductor.[34] To satisfy this

condition, the valence and conduction band edges are bent to achieve a band edges level at the interface ($^{*}\varepsilon_{v/c}$) proportionally with the exchange of charge carriers across the SLJ, at equilibrium.[35] Figure 1.3 shows the energy diagram for an N-type semiconductor before and after contact with electrolyte. The region of band bending is known as space charge (SC) or depletion layer (W). Generally, the photogenerated charges are accelerated to the surface due to the electric field from the double layer. In addition, the band bending can be altered by impurities in the depletion layer, electrode polarization and electrolyte pH.

The flat band potential (E_{ft}) is known as the difference between ($^{*}\varepsilon_{v}$- ε_{v}) or the potential to align the band bending, as showed in Figure 1.3. Under flat band conditions, the photogenerated electron-hole are recombined and do not reach the solid-liquid interface.[35,36] Obviously, this annihilation is a consequence of the absence of the photopotential or an unfavorable polarization. Figure 1.3b shows an energy diagram and Fermi level alignment for a semiconductor before and after it reaches thermal equilibrium on the SLJ, in dark condition.

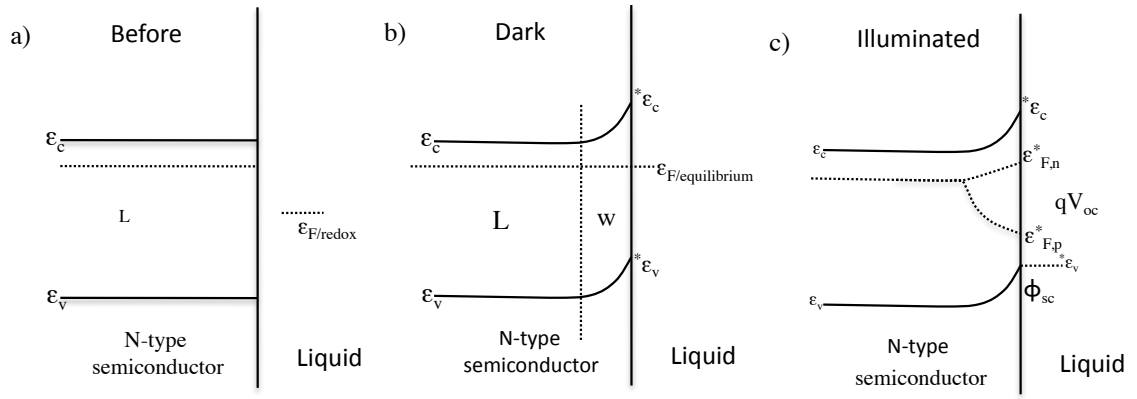

Figure 1.3 Energy level diagram of an N-type semiconductor-liquid junction. a) Before the SLJ b) after equilibrium established in dark condition c) space charge with a quasi-Fermi level, under illumination.

It is well known that semiconductors under illuminated conditions have their thermal equilibrium perturbed due photoelectron generation. Then, the Fermi level splits up into two quasi-Fermi levels, denoted as ($^{*}\varepsilon_{f,n}$) for electrons and ($^{*}\varepsilon_{f,p}$) for holes, as can be seen in Figure 1.3c. The difference between ($^{*}\varepsilon_{F,p}$-$^{*}\varepsilon_{f,n}$) is given by qV_{oc} that defines the maximum open-circuit voltage (V_{oc}).[38]

The thermodynamic requirement to water splitting without a potential applied must satisfy two conditions under photoexcitation state. First, the qV_{oc} must be higher than 1.23 eV and evidently the band gap must be higher than this value. Second, the redox Fermi

level must follow inequalities of the energy level position. To reach this condition, the quasi Fermi level $^{*}\varepsilon_{F,n}$ of the anodic reaction must be smaller than $\varepsilon_{F,oxi}$ and for the cathodic reaction the proceed the quasi Fermi level $^{*}\varepsilon_{F,p}$ must be higher than $\varepsilon_{F,red}$.[39] Figure 1.4 shows the quasi-Fermi level diagram of N-type semiconductor as a photoanode for water splitting. The schema in Figure 1.4a demonstrates a charge transfer reaction on a semiconductor with a high band gap, under photoexcitation state. On the other hand, if the band gap E_g is higher than 1.23 eV and qV_{oc} is lower than this value, then an external potential must be applied to exceed the thermodynamic requirement to water splitting. As shown in Figure 1.4b, photoelectron transfer in a n-type semiconductor has an energy barrier due to the difference between the quasi-Fermi level and the redox-Fermi level ($^{*}\varepsilon_{F,p}$-$\varepsilon_{F,red}$).

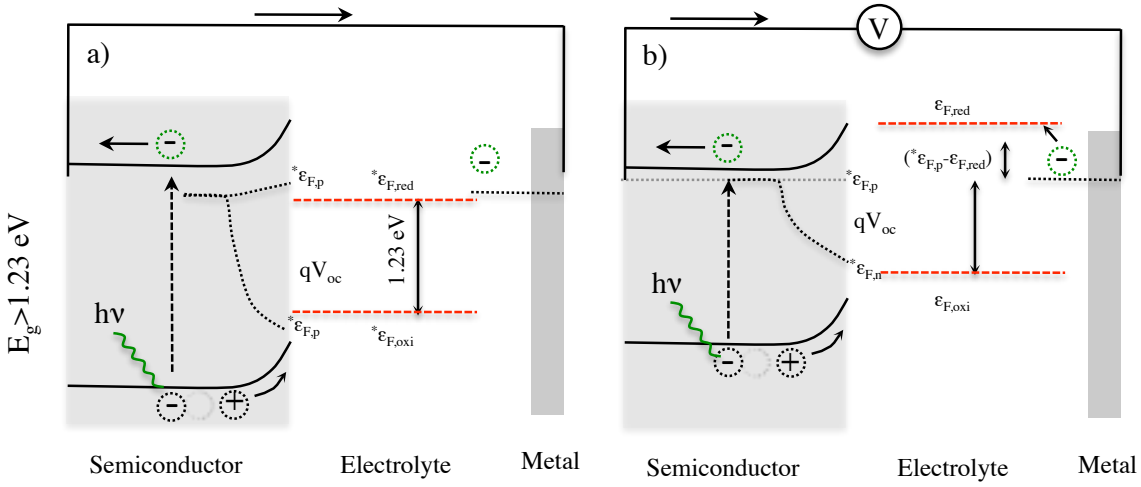

Figure 1.4 Energy levels for a) unassisted and b) assisted electron transfer for water into n-type semiconductor.

Under experimental conditions, unassisted photoelectron transfer proceeds for a semiconductor with high band gap energy or in multijunction. For example, $SrTiO_3$ has a band gap of 3.25 eV and a favorable band edge position for water splitting.[40] However, this semiconductor absorbs only ultraviolet radiation which results in a low efficiency, as can be seen in the next topic.

Generally, semiconductors with assisted electron transfer receive more attention. Figure 1.5 shows an example of photocurrent versus applied potential for a N-type semiconductor in illuminated and dark conditions. In these hypothetic plots can be commented three important points ca be highlighted. The first point, the flat-band potential can be determined between the cathodic polarization and the onset potential of the photocurrent. As mentioned previously, in the flat-band potential there is no electrons

acceleration to the solid-liquid interface. Therefore, electron-hole recombination predominates. The flat-band potential can be achieved when the band bending energy is equal the valence band energy.

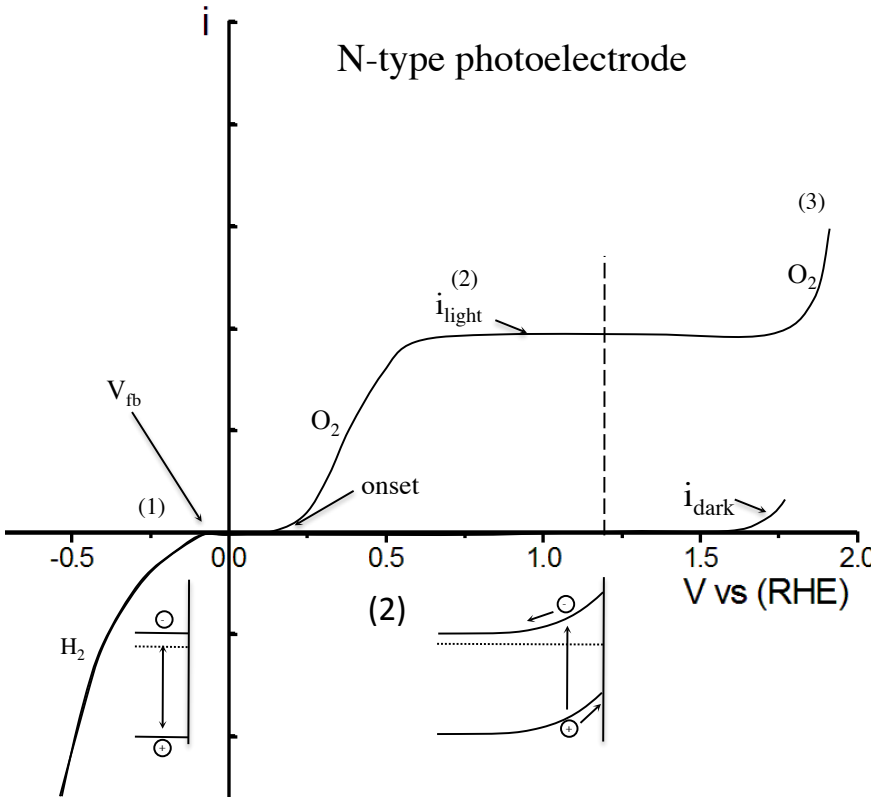

Figure 1.5 Linear sweep polarization of an N-type semiconductor in illuminated and dark condition.

The second point corresponds to the photoexcited reaction current, also known as photocurrent and which is proportional to light intensity. In 1959, Gartner proposed a way to describe the photocurrent of a N-P junction as a function of the absorption coefficient, excluding charge transfer kinetics. The model is based on the integration of electron-hole pairs generated by incident photons [$g(x)= \alpha\phi\exp(-\alpha x)$]. Where α is the optical absorption, x is the beam path penetration into the semiconductor, and ϕ is the photon flux. The Gartner model established that the total photocurrent is the result of photoexcited carriers within the depletion layer and photoexcited carriers in the bulk that migrate into the depletion layer. The photocurrent provided in the depletion layer ($i_{ph(w)}$) considering that the incident photon can fully penetrate the depletion layer width (W).[41] This photocurrent can be described by integration of equation 1.2.

$$i_{ph(w)} = q\int_0^W g(x)dx = -q\phi(e^{-\alpha W} - 1) \tag{1.2}$$

The photocharge diffusion from the bulk to the depletion layer can be solved by a diffusion equation under boundary conditions.[41] The photocurrent equation for hole diffusion can be described by equation 1.3.

$$i_{ph(diff)} = q\phi\frac{\alpha L_p}{1+\alpha L_p}e^{-\alpha W} + qp_0\frac{D_p}{L_p} \tag{1.3}$$

where L_p is the hole diffusion length in the N-type semiconductor, D_p is the hole diffusion constant and p_0 is the equilibrium hole density in dark condition. In 1979, Butler adjusted the Gartner model for a semiconductor liquid junction neglecting the last term of $i_{ph(diff)}$, considering a semiconductor with a larger band gap. The Butler-Gartner model is given by equation 4.[42]

$$J_{photo} = q\phi\left(1 - \frac{e^{-\alpha W}}{1+\alpha L}\right) \tag{1.4}$$

The shift of onset potential, in Figure 1.5, apparently means a contradiction in thermodynamic equilibrium potential of water splitting (see a brief discussion in the next topic). Therefore, it is important to highlight that the photon energy absorbed in the semiconductor is conserved in the photopotential (qV_{oc}).[38] Evidently, the photopotential and applied potential should be higher than 1.23 V to attain water photoelectrolysis.

The third point in Figure 1.5, the electromotive force is sufficiently high to transfer electrons across the band gap and redox-Fermi level and to conduct the water electrolysis without any illumination. In dark condition, the Butler-Volmer model is adequate to predict the charge transfer kinetic.

1.3 Photoelectrochemical water splitting

PV solar cells are excellent devices to generate electricity, obviously in the presence of solar light, but completely inefficient at night or in a rainy day. Thus, there is a tremendous challenge to develop an efficient system to store the photon energy. Photoelectrochemical (PEC) water splitting has been an ambitious strategy that combines a

semiconductor and solar light to split water molecules into hydrogen and oxygen. For Allen J. Bard, photoelectrochemical water splitting is considered the "holy grail" of electrochemistry, due to the huge challenge of discovering an electrochemical system robust for water splitting into hydrogen and oxygen gas. This system must be chemically stable with a long period of live, absorb the maximum available sunlight and have at least 10% of solar-to-hydrogen conversion efficiency. [43]

A PEC cell is constituted essentially of a photoanode and a cathode or of a photocathode and an anode or can also be the junction of a photoanode and a photocathode.[44] Figure 1.6 shows the illustration of a PEC, for study proposal, with one working electrode in the middle, a reference electrode in the left and a counter electrode in the right side of the cell. In the front view, there is a transparent quartz window, which do not absorbs wavelengths of visible and ultraviolet light.

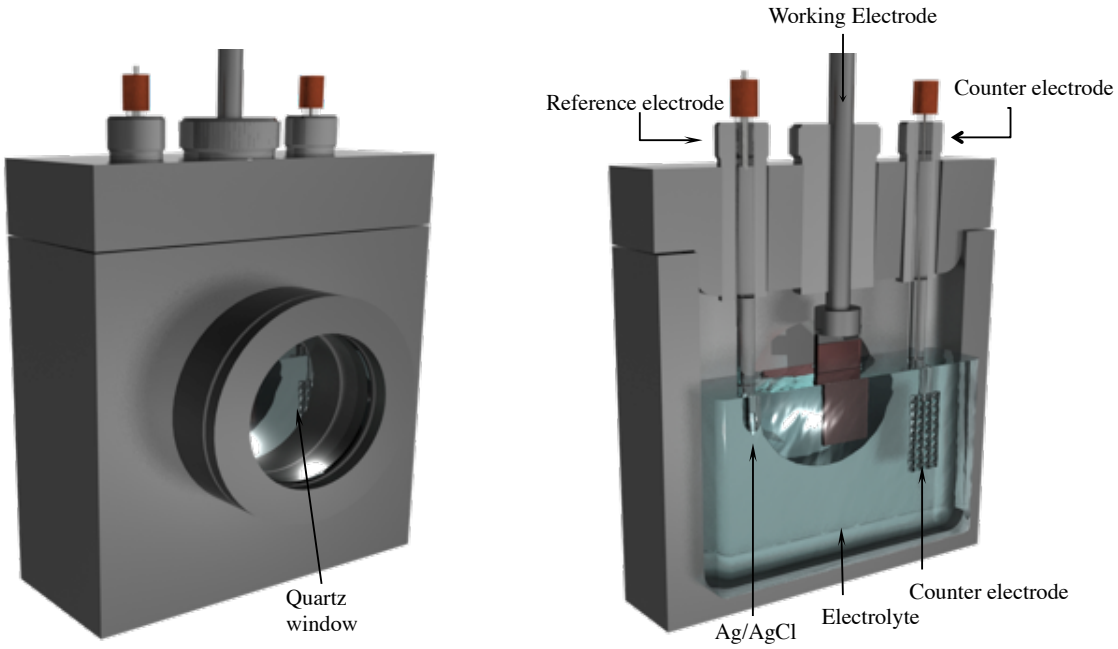

Figure 1.6 Illustration of perspective and cross-sectional view of a photoelectrochemical cell with three electrodes.

Photoelectrochemical water splitting can be carried out in acid or basic medium.[45-47] It depends on the chemical stability and photoactivity of the semiconductor in the electrolyte. The electrolyte pH also determinates the electrochemical reaction mechanism for hydrogen or oxygen gas evolution.[45] For example, at low pH (see chemical equation 1) hydrogen gas is formed by protons reduction at the cathode and consequently water oxidation at the anode.

(1)

$$2H_2O + 4h^+ \rightleftharpoons 4H^+ + O_2 \qquad 1.229 \text{ V vs. RHE}$$

$$4H^+ + 4e^- \rightleftharpoons 2H_2 \qquad 0 \text{ V vs RHE}$$

On the other hand, at high pH water molecules are reduced at the cathode and hydroxyl ions are oxidized at the anode (see chemical equation 2). The same reaction mechanism is valid for photoelectrodes. Therefore, it is crucial to understand the Pourbaix diagram of a semiconductor to select the pH range and determine the electrochemical mechanism.[48]

(2)

$$4H_2O + 4e^- \rightleftharpoons 2H_2 + 4OH$$

$$4OH^- + 4h^+ \rightleftharpoons 2H_2O + O_2$$

The spontaneous process of water formation via the exergonic reaction of H_2 and O_2 has a standard molar Gibbs free energy of -237.2 kJ/mol.[49] The reversible electromotive force to drive water splitting is 1.23 V derived from ($V_{rev}= \Delta G/nF$), under standard conditions. In other words, it means that the free energy provided to split water is conserved in the chemical bonds of the product and released in the spontaneous reaction of water formation.[49,50] More specifically, this released energy can be converted into heat or in electromotive force, for example, a fuel cell operated with hydrogen and oxygen gas.

In experimental conditions, the electrodes can be considered an interface to convert the electromotive force to chemical potential. Therefore, the thermodynamic water splitting does not predict this interface between electrodes with electrochemical species. Thus, the difference between this thermodynamic potential (μ_{redox}) and the operational potential V_{op} ($V_{redox}- \mu_{redox}$) is known as overpotential (η).[51]

The PEC and photovoltaic cell association is a typical configuration to build devices that are operated with a small external potential and the light energy absorbed in a semiconductor. For example, Figure 1.7 show an illustration of three electrochemical system for water splitting.

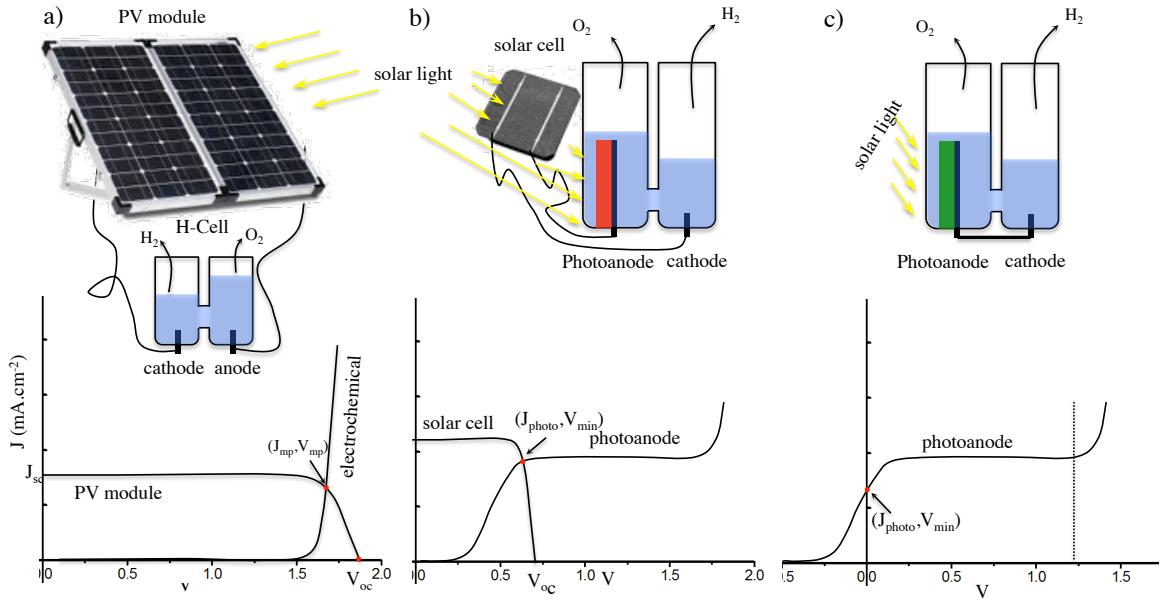

Figure 1.7 Electrochemical cell configuration to produce hydrogen gas via water splitting. a) Conventional water electrolysis assisted by PV module, b) PV-PEC system, and c) wireless PEC cell.

The first system is a conventional electrolytic cell assisted by a PV module. In this case, the total efficiency ($\eta_{PV\text{-}EC}$) of water electrolysis is limited to the maximum power of the PV module, considering a constant standard solar light illumination of AM 1.5 and also a low overpotential for the hydrogen and oxygen evolution reaction, (HER) and (OER) respectively.[52,53] A single solar cell frequently has a low open circuit potential and cannot provide the minimum operational potential for water electrolysis. In addition, the PV module can provide this partial potential but with limited current density due to the multi series-connected cell.[54] The PV-EC efficiency is given by equation 1.5.

$$\eta_{pv-ec} = \eta_{pv}\,\eta_{ec} \tag{1.5}$$

The solar cell efficiency (η_{PV}) can be calculated through the ratio between the maximum electrical power (P_{max}) and the solar irradiance (P_{light}). P_{max} is expressed by the maximum point potential (V_{mp}) and the maximum point current density (J_{mp}). These maximum points can be determined by the open circuit potential (V_{oc}) and the short current (J_{sc}), which is the short-circuit current density. And the ratio ($V_{mp}.J_{mp}/V_{oc}.J_{sc}$) gives the fill factor (FF).[55-57] Then, the η_{PV} efficiency is expressed by equation 1.6.

$$\eta_{pv} = \frac{FF\,V_{oc}\,J_{sc}}{P_{light}} \tag{1.6}$$

The efficiency η_{EC} depends only an operational potential (V_{op}). This V_{op} covers the thermodynamic redox potential (μ_{water}) of water splitting, the overpotentials η_{HER} and η_{OER} and the cell resistance potential iR_{cell}.[58] Thus, the η_{EC} efficiency is given by equation 1.7.

$$\eta_{EC} = \frac{\mu_{water}}{V_{op}} = \frac{\mu_{water}}{1.23V + \eta_{OER} + \eta_{HER} + iR_{cell}} \quad (1.7)$$

It is evident that V_{op} must be higher than μ_{water}. Therefore, the V_{mp} must be at least equal to V_{op} to obtain the maximum current density in the electrolytic cell. The $\eta_{PV\text{-}EC}$ efficiency can be expressed by equation 1.8.

$$\eta_{pv-ec} = \frac{FF.V_{oc}.J_{sc}}{P_{light}}.\frac{\mu_{water}}{V_{op}} \quad (1.8)$$

For second and third examples in Figure 1.7, the efficiency is influenced by the photoelectrode performance in the direct solar-to-hydrogen and oxygen conversation. Figure 1.7b shows an illustration of a PV-PEC system and a hypothetical plot of current versus applied potential (V_{ap}). The overall solar-to-hydrogen efficiency (η_{STH}) can be obtained by the ratio P_{PEC}/P_{light}. The PEC power (P_{PEC}) is given by $J_{photo}(\mu_{water} - V_{ap})$.[59] It should also be mentioned that η_{STH} does not depend on η_{PV}. The photopotential of PV cell should be adjusted to achieve the minimum V_{ap}, considering that J_{photo} is generated by the photoelectrodes. The last example, Figure 1.7c, has been a huge challenge in this field. The value of η_{STH} for a wireless PEC cell can be calculated with the same equation mentioned in the case of Figure 1.7b. However, in this example, there is no V_{ap} and the efficiency equation can be given simply by $J_{ph}.\ \mu_{water}/P_{light}$.[60]

In spite of these promising perspectives of PEC to produce hydrogen fuel, there are many critical parameters to be overcome. As mentioned previously, the PEC must have long lifespan, low cost and at least 10% of solar-to-hydrogen conversion.

1.4 Solar to Hydrogen Conversion Efficiency

The theoretical solar light to hydrogen conversion efficiency depends essentially on the band gap and on the non-degenerate state. The semiconductor band gap is correlated with the maximum light absorption and the photoactivities are expressed in terms of charge separation and charge injection or transfer.[61] These parameters are essential to estimate the

solar energy conversion efficiency. The maximum theoretical photocurrent density (J_{ph}) is given by equation 1.9.

$$J_{ph} = \eta_{ab} . \eta_{bulk} . \eta_{surface} \quad (1.9)$$

where (η_{abs}) is the absorption efficiency associated with the maximum light absorbed from the solar spectrum. The η_{bulk} is the electron-hole separation yield that can reach the solid-solid and solid-liquid interface. The main parameter that affects η_{bulk}, is the charge transport.[61,62] And of course, the charge transport is influenced by many other parameters, such as grain boundary, element doping, impurities, crystallographic structure and orientation, crystallite size and allotropy. On the other hand, $\eta_{surface}$ is responsible for the charge transfer kinetic on the interface, both solid-solid and solid-liquid.[61,62] The value of $\eta_{surface}$ depends on three processes: lifetime of charges photogenerated on the surface, the charge transfer kinetic across the compact layer and the diffusion of redox particles in the electrolyte. In the other words, the total overpotential can be written as the sum of $\varphi_{p,SC}$ (lifetime of charge on surface), φ_H (transfer of hole-electron on the interface) and φ_{diff} (diffusion of redox particles).[63]

Assuming that η_{bulk} and η_{surf} have 100% of efficiency. Thus, J_{ph} can be deducted as a function of J_{ab}. The correlation between J_{ph} and the optical absorption coefficient can be obtained through the Gartner model. The ratio $J_{ph}/q\phi$ describes the Incident Photo-to-Current conversion Efficiency, abbreviated as IPCE in equation 1.10.

$$IPCE = \frac{J_{ph}}{q\phi} = 1 - \frac{e^{-\alpha W}}{1 + \alpha L} \quad (1.10)$$

The light power density P_{light} can be obtained by multiplying the photon flux by the energy of a single photon (hc/λ). In this case, IPCE can be expressed as a function of $J_{ph}/P_{(w)}$ and given by equation 1.11.

$$IPCE = \frac{J_{ph}}{P_{light}} . \frac{hc}{q\lambda} \quad (1.11)$$

The theoretical maximum photocurrent of a semiconductor can be calculated by the IPCE equation.[65] To achieve an IPCE of 100%, it is necessary to assume that all incident photons are absorbed and converted to photocurrent. To consider this hypothesis, the light power density must be expressed as a function of the spectral irradiance given by ($E_\lambda . \lambda$)

and considering that the semiconductor has a high absorption coefficient, sufficient thickness to absorb this spectral irradiance and a large depletion layer. In this condition, J_{ph} can be integrated from 300 to 1100 nm and expressed as

$$J_{ph} = \eta_{ab} = \int_{300}^{1100} \frac{1}{1240} . E_{\lambda} . \lambda . d(\lambda) \qquad (1.12)$$

Equation 1.12 is fundamental to predict the maximum current density of semiconductor in function of band gap. Figure 1.8 shows the theoretical photocurrent density in function of photon energy from 1.2 eV to 4.1 eV. This range was selected because most semiconductors have a band gap between these values. For example, silicon with a band gap of 1.1 eV can achieve the maximum photocurrent of 36 $mA.cm^{-2}$.[66] On other hand, TiO_2 can achieve 1.78 $mA.cm^{-2}$ due to the band gap of 3.2 eV.[67] The value of η_{STH} can also be estimated using this plot in Figure 1.8 and the equation (J_{photo}. μ_{water} /P_{light}). In this aspect, the TiO_2 with a value of 1.78 $mA.cm^{-2}$ can achieved no more than 2.2% of solar-to-hydrogen efficiency.

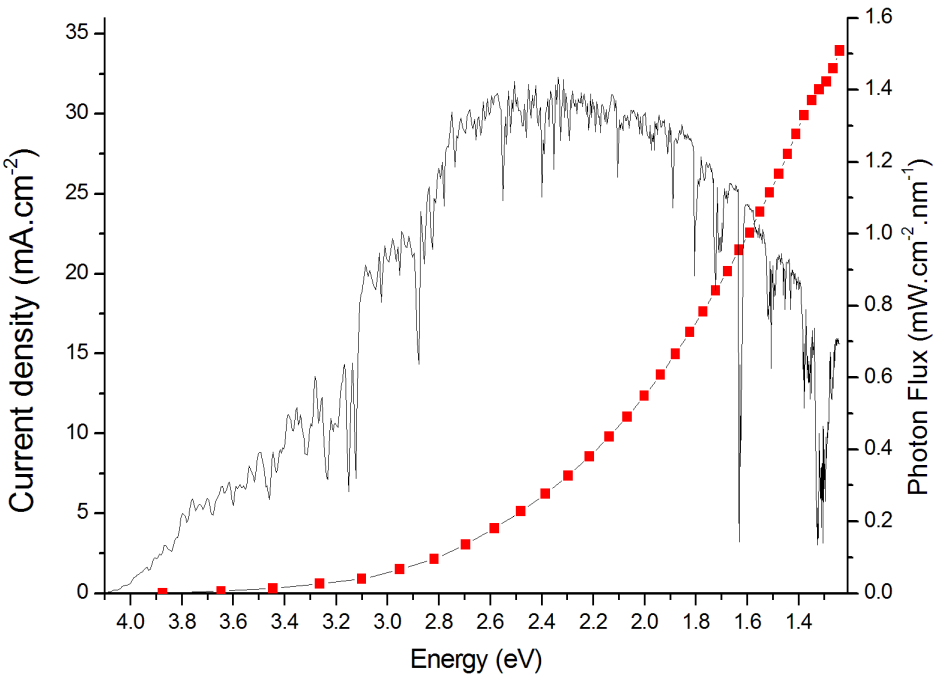

Figure 1.8 Maximum theoretical photocurrent density versus energy (eV) (red dots). Spectral irradiance at AM 1.5 (black line).

As mentioned previously, there is not a general equation to predict the flat-band potential. However, this flat-band potentials can be determined experimentally by Mott-Schottky plots. For example, flat-band potential of many single-crystal semiconductors

were reported. From one combination of the experimental flat-band potential and the maximum theoretical J_{photo} can build a plot that represents a hypothetical J_{ph} *vs*. V_{RHE} curve, as can be seen in Figure 1.9.

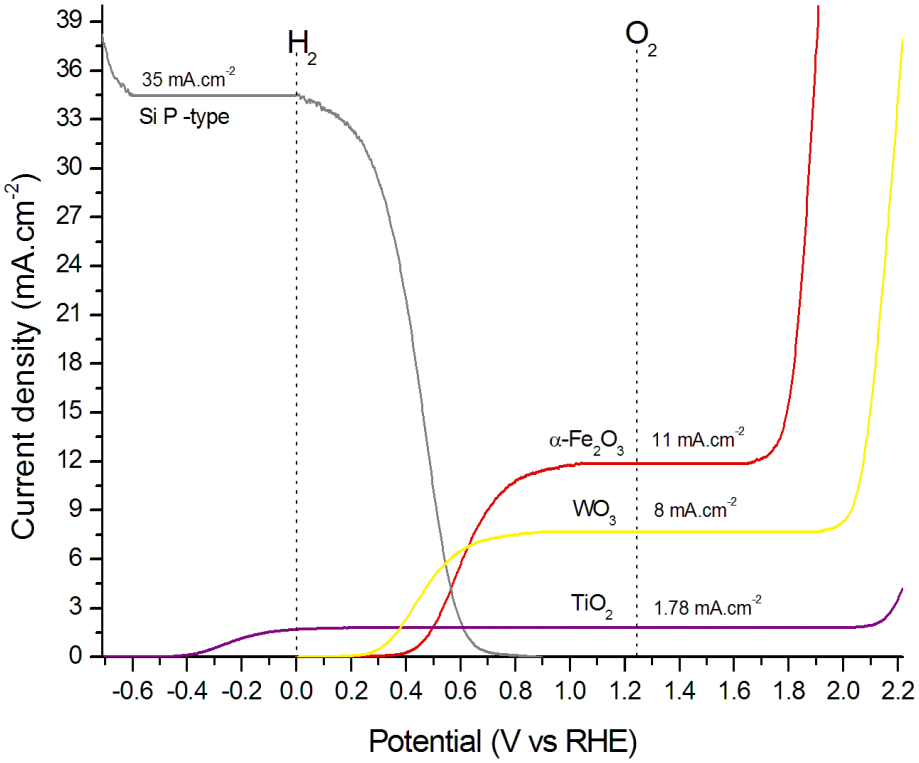

Figure 1.9 Hypothetical combination of the experimental flat-band potential and maximum theoretical J_{ph} of different semiconductors (indicated in the figure).

1.5 Hematite Thin Film: as a Photoanode

Hematite has been considered as an excellent candidate for PEC. That is because this semiconductor oxide has a band gap of 2.2 eV,[68] which implies that it has the ability to absorb part of visible light, as can be seen in Figure 1.9. The key requisite that makes this oxide semiconductor appropriate for this application is its electrochemical stability, in high pH electrolytes, and the abundance of iron. Theoretically, hematite can achieve 14% of solar-to-hydrogen efficiency, which correspond to 11 $mA.cm^{-2}$. However, the hematite photoanode has been experimentally a challenge for photoelectrochemistry due to its poor charge transport that has limited the performance of solar-to-hydrogen conversion.

Obviously, the doping process should control this charge transport. However, it has been hard to figure out an effective doping element for hematite. To overcome this situation, some research groups have been focused in developing new route strategies to design nanostructured or mesoporous thin films. These strategies have the advantage of increasing the surface area and the thickness control.

The charge transfer kinetics has also been an important parameter that directly affects the efficiency. In general, the overpotential for a semiconductor is defined as the difference between the flat-band potential and the photocurrent onset. The main strategy to improve the charge transfer kinetic has been the depositof catalysts on the hematite surface.

1.5.1 Colloidal Deposition Process

The colloidal nanocrystals deposition process (CND) is a versatile method to process hematite thin films. This method is based on the nanocrystals synthesis and deposition on the FTO substrate. In this case, magnetite (Fe_3O_4) or maghemite (γ-Fe_2O_3) nanocrystals are synthesized by the thermal decomposition method to achieve a diameter of approximately 5 to 8 nm.[69] The colloidal stability is an important factor to obtain a highly homogeneous thin film and control of thickness. Gonçalves *et al*[70] produced mesoporous hematite thin film by a thermal treatment of a magnetite on the FTO substrate. The hematite photoanode reached 1.1 $mA.cm^{-2}$ at 1.23 V_{RHE}. This photocurrent density was obtained after the deposition of 6 layers of magnetite nanocrystals and consecutive thermal treatments at 820 ºC.[69] Figure 1.10 shows a schematic diagram of the CND process. The high and low magnification of TEM images shows monodispersive synthesis of magnetite nanocrystals. The photograph (Figure. 1.10e) of the hematite photoanode can be seen in Figure 1.10d and STEM cross-sectional image shows the FTO substrate and the hematite grown as a mesoporous columnar structure. The disadvantages of this process are the multilayer and small area deposition that make hard to scale-up the process and also the low STH efficiency.

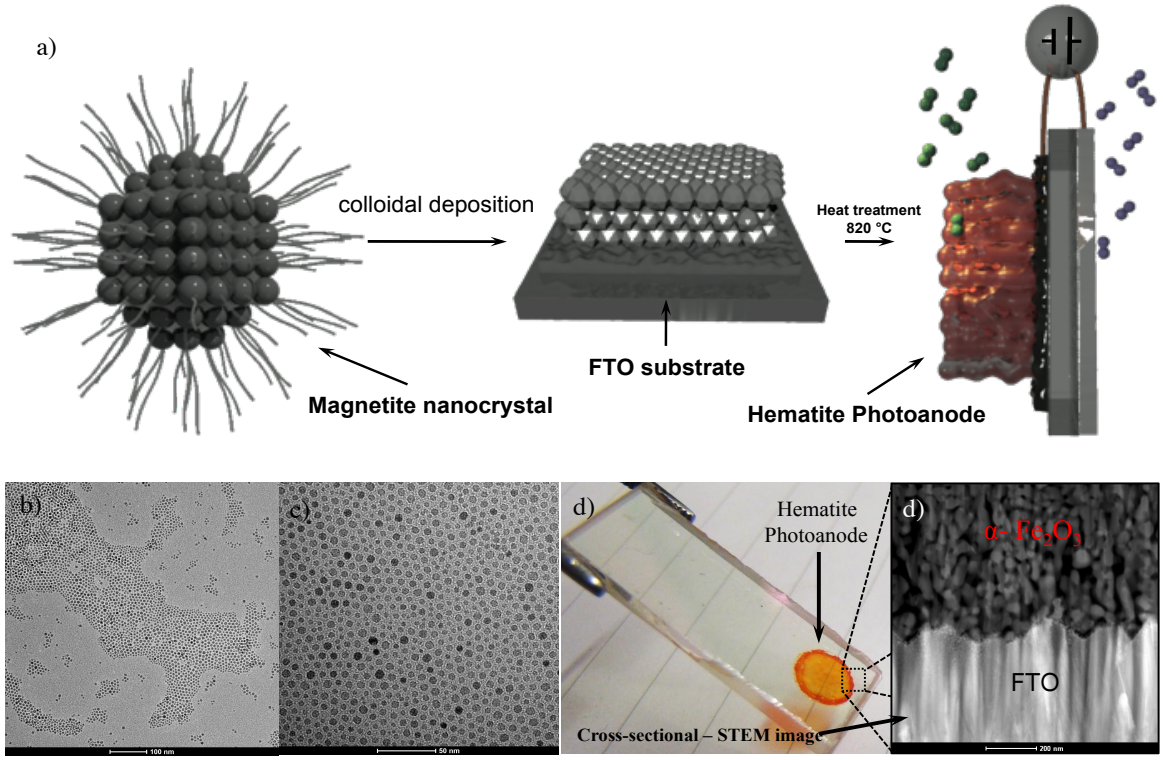

Figure 1.10 General views of CND process a) schema of CND in three steps. b) Low magnification TEM image, c) the high magnification TEM image. d) Photograph of hematite deposited on FTO. e) STEM cross-sectional image of the hematite thin film. Ref. [69] with permission from the American Chemical Society.

This CND process also was adapted for WO_3 thin film deposition. Colloidal WO_3 nanowires were deposited on a FTO substrate and treated at 650 ºC for few seconds. The WO_3 photoanode also achieved impressive photoresponse and excellent electrochemical stability.[71]

1.5.2 Atmospheric Pressure Chemical Vapor Deposition

Atmospheric Pressure Chemical Vapor Deposition (APCVD) has also been a highlighted technique for hematite deposition. The basic idea of this process is to drag an iron precursor from a chamber to a hot plate at atmospheric pressure. This precursor is quickly decomposed and transformed into hematite.[72] The dendritic hematite thin film is grown up to 900 nm of thickness and cooled down. The best-optimized results of a hematite photoanode were 3.0 $mA.cm^{-2}$ at 1.23 V_{RHE} under standard solar illumination, with a layer of iridium oxide. This result corresponds to 4% of STH efficiency coupling with solar cell.[73]

The results of Michael Gratzel's group have been a benchmark for using this deposition process. For example, Scott Warren[74] published an important article with

promising experimental results and theoretical modeling for hematite photoanode. In spite of excellent results, this technique has a systematic protocol to attain reproducible deposition.[75,76]

1.5.3 Pulsed Laser and Atomic Layer Deposition

Pulsed Laser and Atomic Layer Deposition, (PLD) and (ALD) respectively, are sophisticated techniques for semiconductor, catalyst or organic compound deposition on a substrate. ALD is a technique that drags a volatile precursor, such as iron t-butoxide or iron pentacarbonyl, to a controlled atmosphere chamber.[77] In this chamber, the precursors are quickly decomposed on the heated substrate to form a hematite nanostructure. Dunwei Wang group has been working with nanostructured hematite known as nanonet, where a thin layer of hematite is grown on $TiSi_2$ nanonet/FTO. This structure deposited by ALD has attained 1.6 $mA.cm^{-2}$ at 1.23 V_{RHE} and also good electrochemical stability.[78]

PLD technique has impressive control of thickness and epitaxial control. Generally, the precursor is a compact solid. Thus, the laser beam is focused in this precursor known as target. The laser beam has enough energy to evaporate atoms on the main chamber. These evaporated atoms are deposited on the heated substrate under a controlled atmosphere. The PLD technique has the ability to produce compact thin films by epitaxial growth.[79] In spite of excellent homogeneity and crystallographic control; PLD yields hematite photoanodes of low performance. However, the obtained hematite thin films are excellent for fundamental studies, such as electrochemical impedance spectroscopy characterization.

1.5.4 Hydrothermal and Sol Gel Process

The hydrothermal process is an important route to grow hematite thin films on a FTO substrate. This strategy is based on the precursor hydrolysis and hydrothermal process. Generally, this chemical reaction is carried out in a pressurized container under heating. The hematite structure grows with as nanorod morphology and has excellent photoelectrochemical performance. Sung Lee's group has recently published a wormlike hematite photoanode with a photoresponse of 4.32 $mA.cm^{-2}$ at 1.23 V_{RHE} under standard solar light illumination.[80,82]

1.6 References

1. Jordan D. C.; Kurtz, S. R. Photovoltaic Degradation Rates — *An Analytical Review*. *Progress in Photovoltaics: Research and Applications*. 21,12-29, **2013**.

2. Hermann S., The Solar Economy: Renewable Energy for a Sustainable Global Future. ISBN: 1-84407-075-1, **2002**.

3. Pleatsikas, C.J.; Hudson, E.A.; Goettle, R. Solar energy and the U.S. economy. *West view Press*, **1982**.

4. Ross RG, Jr.; Smokler MI. Flat-Plate Solar Array Project Final Report. *Report DOE/JPL-* 1012-125, October **1986**.

5. Gueymard, C.; Myers, D.; Emery, K. Proposed reference irradiance spectra for solar energy systems testing. *Solar Energy*, 73, 6, 443-467, **2002**.

6. Gonzalez, C.C.; Ross, R.G. Performance measurement reference conditions for terrestrial photovoltaics. *International Solar Energy Society*. AS/ISES, **1980**.

7. Hulstrom, R.; Bird R.; Riordan, C.; Spectral Solar Irradiance Data Sets for Selected Terrestrial Conditions. *Solar Cells*, 15, 365-391, **1985**.

8. Tiedje, T.; Yablonovitch, E.; Cody, G. D.; Brooks, B. G. Limiting Efficiency of Silicon Solar Cells. *IEEE Transactions on Electron Devices*, 31, 5, **1984**.

9. Pellow, M. A.; Emmott, C.J. M.; Barnhart, C. J.; Benson, S. M. Hydrogen or Batteries for grid Storage. A net energy Analysis. *Energy Environ. Sci*., 8, 1938, **2015**.

10. Padro, C.E.G.; Putsche, V. Survey of the Economics of Hydrogen Technologies. *National Renewable Energy Laboratory*. September, **1999**.

11. Midilli, A.; Ay, M.; Dincer, I.; Rosen, M.A. On hydrogen and hydrogen energy strategies: I: current status and needs. *Renew Sustain Energy Rev*, 9, 255–271, **2005**.

12. Committee on Alternatives and Strategies for Future Hydrogen Production and Use, National Research Council. *The Hydrogen Economy: Opportunities, Costs, Barriers, and R&D Needs*. Washington, D.C.: The National Academy Press. **2004**.

13. Skelton, L. W. The solar-hydrogen energy economy: Beyond the age of fire. Int. *J. Hydrogen Energy*, 10, 2, 81-88, **1985**.

14. Levie, R. de. The electrolysis of water. *Journal of Electroanalytical Chemistry*, 476, 92–93, **1999**.

15. A. Paets van Troostwijk, J.R. Deiman, Sur une manière de décomposer l'Eau en Air inflammable et en Air vital. *Obs. Phys*. 35, **1789**.

16. Kreuter W, and Hofmann H, Electrolysis: the important energy transformer in a world of sustainable energy. *Int. J. Hydrogen Energy* 23(8): 661-666, **1998**.

17. Trasatti, S. Water electrolysis: who first?. *Journal of Electroanalytical Chemistry,* 476, 90–91, **1999**.

18. Trasatti, S. 1799–1999: Alessandro Volta's 'Electric Pile': Two hundred years, but it doesn't seem like it. *Journal of Electroanalytical Chemistry,* 460, 1–4, **1999**.

19. Markovic´, N. M.; Grgur, B. N.; Ross, P. N. Temperature-dependent hydrogen electrochemistry on platinum low-index single-crystal surfaces in acid solutions. *J. Phys. Chem. B*, 101, 5405, **1997.**

20. Independent Review. Current State-of-the-Art Hydrogen Production Cost Estimate Using Water Electrolysis. U.S. Department of Energy Hydrogen Program, **2009**.

21. Amos, W.A. Costs of Storing and Transporting Hydrogen. *NREL*, **1998**.

22. Klebanoff, L., Hydrogen Storage Technology: Materials and Application. *Taylor& Francis Group*, LLC, **2013**.

23. Alternative fuels for automotive transportation--A feasibility study, U.S. Environmental Protection Agency Report No. EPA-460/3-74-012. Chicago: Institute of Gas Technology, **1974**.

24. Kant, F. H. Feasibility study of alternative fuels for automotive transportation, U.S. Environmen- tal Protection Agency Report No. EPA-460/3-74-O09. Linden, New Jersey: Exxon Research and Engineering Co., June **1974**.

25. Kromer, M.; Heywood, J. (). Electric Powertrains: Opportunities and Challenges in the U.S. Light-Duty Vehicle Fleet. LFEE 2007-03 RP. Cambridge, MA: *Sloan Automotive Laboratory, Laboratory for Energy and the Environment, Massachusetts Institute of Technology*. **2007**

26. Shockley, W. Electrons and Holes in Semiconductors. Princeton, NJ: *Van Nostrand*, **1950**.

27. Sinton, RA, Swanson RM. Recombination in highly injected silicon. *Electron Devices, IEEE Transactions on*. 34,1380 – 1389, **1987.**

28. Shive, J. N. The properties, physics, and design of semiconductor devices, D. *Van Nostrand Company*, INC, **1959**.

29. Goudet G.; Meuleau, C. Semiconductors: their theory and practice. *Macdonald & Evans; Fair Lawn, N.J., Essential Books*, **1957**.

30. Kittel, C. Introduction to Solid State Physics 8th Edition. Wiley, **2005**.

31. Leighton, R. B. Principles of Modern Physics. *McGraw-Hill*. 340. **1959.**

32. Reif, F. Fundamentals of Statistical and Thermal Physics. *McGraw–Hill*. **1965**.

33. Sato, N. Electrochemistry at Metal and Semiconductor Electrodes. *Elsevier*, **1988**.

34. Williams, F.; Nozik, A. J. Solid-state perspectives of the photoelectrochemistry of semiconductor-electrolyte junctions. *Nature*, 312, 1, **1984**.

35. Gerischer, H. Physical Chemistry: An Advanced Treatise, edited by H. Eyring et al. (Academic, New York,), Vol. IX, p. 463, **1970**.

36. Bolts, J. M.; Wrlghton, M. S. Correlation of Photocurrent-Voltage Curves with Flat-Band Potential for Stable Photoelectrodesfor the Photoelectrolysisof Water. *The Journal of Physical Chemistry*, 80, 24, **1976**.

37. Shockley, W.; Queisser. H. J. Detailed Balance Limit of Efficiency of p-n Junction Solar Cells. *Journal of Applied Physics,* 32, 510, **1961**.

38. Huang, S. Y.; Schlichthorl, G.; Nozik, A. J.; Gratzel, M.; Frank, A. J. Charge recombination in dye-sensitized nanocrystalline TiO_2 solar cells. *J. Phys. Chem. B*, 101, 2576, **1997**.

39. Reineke, R.; Memming, R. Comparability of Redox reactions at n- and p-type semiconductor electrodes. 1. The quasi-Fermi Level concept. *J. Phys. Chem.*, 96, 3, 1310–1317, **1992**.

40. Wrighton, M. S.; Arthur B. Ellis, Peter T. Wolczanski, David L. Morse, Harmon B. Abrahamson, David S. Ginley. Strontium titanate photoelectrodes. Efficient photoassisted electrolysis of water at zero applied potential. *J. Am. Chem. Soc.,* 98, 10, 2774–2779, **1976**.

41. Gärtner, W. W. Depletion-Layer Photoeffects in Semiconductors. *Physical Review*, 116, 1, **1959**.

42. Ginley, D. S. and Butler, M. A. Charge-Transfer Processes in Photoelectrochemical Cells, ACS Symp. Ser. 146 (Photoeff. at Semicond.-Electrolyte Interfaces): 79-101, **1981**

43. Bard, A. J.; Fox, M. A. Artificial photosynthesis: solar splitting of water to hydrogen and oxygen, *Acc. Chem.Res.,* 28, 3, **1995.**

44. Walter, M. G.; Warren, E. L.; McKone, J. R.; Boettcher, S. W.; Mi, Q.; Santori, E. A.; Lewis, N. S. Solar Water Splitting Cells. *Chem. Rev.,* 110, 6446– 6473, **2010**.

45. Van de Krol, R., Liang, Y.; Schoonman, J. Solar hydrogen production with nanostructured metal oxides. *J Mater Chem,* 18, 2311, **2008.**

46. Grimes, C.A.; Varghese, O. K.; Ranjan, S., Light, Water, Hydrogen. The Solar generation of Hydrogen by Water Photoelectrolysis. New York, **2008**.

47. Bard, A.J.; Wrighton, M.S. Thermodynamic Potential for the Anodic Dissolution of n-Type Semiconductors *J. Electrochem. Soc.,* 124, 1706, **1977**.

48. Kung, H. H.; Jarrett, H. S.; Sleight, A. W.; Ferretti, A. Semiconducting oxide anodes in photoassisted electrolysis of water. *J. Appl. Phys.* 48, 2463, **1977**.

49. Bard, A. J.; Parsons, R.; Jordan, J. Standard Potentials in Aqueous Solutions (Marcel Dekker, New York. **1985**.

50. Ohta, T. Solar-hydrogen energy systems. Oxford and New York, Pergamon Press, 25-33, **1979**.

51. Bard, A. J.; Inzelt, G.; Scholz, F. Electrochemical Dictionary 2nd, Revised and Extended Edition, *Springer*, **2012**.

52. Eisenstadt, M.M.; Cox, K.E. Hydrogen production from solar energy. *Solar Energy*, 17, 59, **1975**.

53. Estève, D.; Ganibal, C.; Steinmetz, D.; Vialaron, A. Performance of a photovoltaic electrolysis system. *International Journal of Hydrogen Energy*, 7, 9, **1982**.

54. Dini, D. Hydrogen production through solar energy water electrolysis. *International Journal of Hydrogen Energy*, 8, 11–12, **1983.**

55. Kelly, N.A.; Gibson T.L.; Cai M, Spearot J.A.; Ouwerkerk, D.B. Development of a renewable hydrogen economy: Optimization of existing technologies. *Int J Hydrogen Energy*, 35, 892–899, **2010**.

56. Henry, C. Limiting efficiencies of ideal single and multiple energy-gap terrestrial solar cells. *J. Appl. Phys.*, 51, 4494–4500, **1980**.

57. Shockley W, Queisser H Detailed balance limit of efficiency of p-n junction solar cells. *J. Appl. Phys.* 32:510–519. **1961**.

58. Surendranath, Y; Bediako, D.K.; Nocera, D.G. Interplay of oxygen-evolution kinetics and photovoltaic power curves on the construction of artificial leaves. *Proc. Natl. Acad. Sci.* 109, 39, 15617–15621, **2012**.

59. Parkinson, B. A. *On the Efficiency and Stability of Photoelectrochemical Devices, Acc. Chem. Res., 17, 431–437, **1984**.*

60. Bockris, J.O.M.; Murphy, O.J. Photoconversion Efficiencies for Photo-assisted Electrolysis of Water. *Appl. Phys. Commun.*,2, 3, 203, **1983**.

61. Bolton, J. R.; Strickler, S.J.; Connolly, J. S. Limiting and realizable efficiencies of solar photolysis of water. *Nature,* 316, 495 -500. **1985**.

62. Dotan, H.; Sivula, K.; Grätzel, M.; Rothschild, A.; Warren, S. C. Probing the Photoelectrochemical Properties of Hematite (α-Fe_2O_3) Electrodes Using Hydrogen Peroxide as a Hole Scavenger. *Energy Environ. Sci.* 4, 958– 964, **2011**.

63. Myamlin, V. A. ; Pleskov, Y. V. Electrochemistry of Semiconductors, Plenum Press, New York **1967**.

64. Gerischer, H.; Kolb, D. M.; Sass, J. K. The study of solid surfaces by electrochemical methods *Adv. in Phys*., 27, 437, **1978**.

65. David, S.; Buttler, M.A. semiconductor Electrodes. 329, *Elservier*, **1988**.

66. Green, M.A.; Emery, K.; Hishikawa, Y.; Warta, W., Dunlop, E.D. Solar cell efficiency tables *Prog. Photovolt. Res. Appl*. 21:1–11, **2013**.

67. Fujishima, A.; Honda, K. Electrochemical Photolysis of Water at a Semiconductor Electrode, *Nature* 238, 37, **1972**.

68. Marusak, L. A.; Messier, R.; White, W. B. Optical absorption spectrum of hematite, Fe_2O_3 near IR to UV, *J. Phys. Chem. Solids* ,41, 981–984, **1980**.

69. Le Formal F, Gratzel M, Sivula K. Controlling photoactivity in ultrathin hematite films for solar water splitting. *Adv Funct Mater*. 20:1099–1107, **2010**.

70. Goncalves, R. H.; Lima, B. H. R.; Leite, E. R. Magnetite Colloidal Nanocrystals: A Facile Pathway To Prepare Mesoporous Hematite Thin Films for Photoelectrochemical Water Splitting, *J. Am. Chem. Soc*., 133, 6012–6019, **2011.**

71. Goncalves, R. H.; Leite, L. D. T.; Leite, E. R. Colloidal WO_3 nanowires as a versatile route to prepare a photoanode for solar water splitting, *ChemSusChem*, 5, 2341–2347, **2012**.

72. Cesar, I.; Sivula, K.; Kay, A.; Zboril, R.; Gratzel, M. Influence of feature size, film thickness, and silicon doping on the performance of nanostructured hematite photoanodes for solar water splitting, *J. Phys. Chem. C,* 113, **2009**.

73. Warren, S. C.; Voitchovsky, K.; Dotan, H.; Leroy, C. M.; Cornuz, M.; Stellacci, F.; Hebert, C.; Rothschild, A.; Gratzel, M. Identifying champion nanostructures for solar water-splitting, *Nat. Mater*., 12, 842–849, **2013**.

74. Tilley, D. S.; Cornuz, M.; Sivula, K.; Gratzel, M. Light-Induced Water Splitting with Hematite: Improved Nanostructure and Iridium Oxide Catalysis, *Angew. Chem., Int. Ed*., 49, 1–5, **2010.**

75. Sivula, K.; Le Formal, F.; Gratzel, M. WO_3-Fe_2O_3 Photoanodes for Water Splitting: A Host Scaffold, Guest Absorber Approach, *Chem Mater 21*, 2862, **2009**.

76. Kay, A.; Cesar, I.; Graetzel, M. New benchmark for water photooxidation by nanostructured α-Fe_2O_3 films. *J. Am. Chem. Soc, 128*, 15714, **2006**.

77. Hahn, N. T.; Ye, H.; Flaherty, D.W.; Bard, A. J.; Mullins, C. B. Reactive Ballistic Deposition of α-Fe_2O3 Thin Films for Photoelectrochemical Water Oxidation. *ACS Nano*, 4, 1977, **2010.**

78. Zandi, O.; Klahr, B. M.; Hamann, T. W. Electrolysis of Liquid Ammonia for Hydrogen. Generation, *Energy Environ. Sci*., 6, 634–642, **2013**.

79. Lin, Y.; Zhou, S.; Sheehan, W. S.; Wang, D. Nanonet-based hematite hetero-nanostructures for efficient solar water splitting. *J. Am. Chem. Soc.,* 133, 2398–2401, **2011**.

80. Engel, J.; Tuller, H. L. The Electrical Conductivity of Thin Film Donor Doped Hematite: From Insulator to Semiconductor by Defect Modulation, *Physical Chemistry Chemical Physics*, 16, 23, 11374, **2014**.

81. Beermann, N.; Vayssieres, L.; Lindquist, S.; Hagfeldt, A. Photoelectrochemical studies of oriented nanorod thin films of hematite, *Journal of the Electrochemical Society*, 147, 7, 2456–2461, **2000**.

82. Xi, L.; Chiam, S. Y.; Mak, W. F.; Tran, P. D.; Barber, J.; Joachim Loo, S. C.; Wong, L. H. A novel strategy for surface treatment on hematite photoanode for efficient water oxidation. *Chem. Sci.,* 4, 164–169, **2013.**

83. Kim, J. Y.; Magesh, G.; Youn, D.H.; Jang, J.-W.; Kubota, J.; Domen, K.; Lee, J. S., Single-crystalline, wormlike hematite photoanodes for efficient solar water splitting, *Scientific Reports* ,3, 2681, **2013**.

Chapter 2. Nanostructural Characterization of Mesoporous Hematite Thin Film Photoanode Used for Water Splitting

Reproduced **by**
permission of Cambridge Journals (Journal of Materials Research, 29, 01, 2014)

2.1 Introduction

Solar energy can provide sufficient power for all of our energy needs if it can be efficiently harvested. An elegant and potentially efficient route to storing solar energy is to convert light into chemical energy in the form of chemical bonds, which is a form of artificial photosynthesis process. Considering the abundance of H_2O on the planet, water splitting is a natural pathway for artificial photosynthesis. Hematite (α-Fe_2O_3) is a candidate material to be used as a photoanode for water splitting due to intrinsic properties such as suitable band gap (2.0-2.2 eV) for visible light absorption, chemical and photoelectrochemistry stability, abundance and low cost.[1-4] However, there are enormous challenges to be overcome before this material is available for technological applications. The main challenges in the implementation of this material are: a) a large over-potential for water oxidation; b) a relatively low absorption coefficient requiring thick films (in the range of 400-800 nm) for efficient light absorption; c) a poor majority carrier conductivity (electrons), and d) a short diffusion length of the minority charge (hole).[5-8] Actually, many of these problems contribute in a direct or indirect way to the electron-hole recombination process. In recent years, a decrease in the electron-hole recombination and an increase in the surface area through the use of a nanostructured hematite film has been the focus of researchers to obtain a high-performance photoanode.[8-10] Indeed, the electron-hole recombination can be minimized in very thin films; however, low light absorption produces low efficiency.[11,12] Thus, two strategies can be used to improve the photocurrent in thick films with a maximum of visible light absorption. The first strategy is based on modifying the electronic structure by doping hematite.[13-15] For instance, Ling et al. demonstrated that a hematite thin film doped with Sn (IV) can improve the performance of a hematite photoanode by changing carrier concentrations and carrier mobility.[16] Sivula et al. also showed that unintentional doping by tin (Sn^{4+}) during the high temperature sintering process can improve the photocurrent of a hematite film processed by a colloidal route.[17] The second alternative is to use the anisotropic conductivity of pure hematite which shows higher conductive along the (001) basal plane.[18-21] For example, this

preferential orientation can be induced in a pure and doped hematite thin film using special deposition methods such as chemical vapor deposition,[22-24] atomic ballistic deposition,[25] nanorod goethite growth[26] or nanocrystal colloidal deposition.[27] A high temperature also has a strong effect on the texture of a hematite thin film deposited on a transparent conductor oxide (TCO) which is independent of the method used.[25,27] However, due to the necessity to use a TCO substrate (mainly SnO_2:F (FTO) on glass), the growth of oriented hematite in a specific crystallographic direction is not a simple task.

The recent development of different synthetic routes to process pure and doped hematite photoanodes with controlled dimension and morphology offer practical solutions to improve the overall water oxidation activity. In particular, the processing of a hematite photoanode by nanoparticle deposition followed by a sintering step has attracted special attention due to its high photocurrent[16] and low over-potential for water oxidation. [27] Apart from this performance progress, many fundamental questions and open issues remain. For instance, there is no consensus about the beneficial impact on photoanode performance of preferential growth along the [110] axis. It is also not clear if the unintentional doping (by tin ions), which occurs during the high temperature sintering process, is important to promote the increase of water oxidation activity. Another point to be explored is the interface quality between the hematite film and the FTO substrate. Transmission electron microscopy (TEM) and STEM with analytical capabilities are powerful tools that can provide new information for these fundamental issues. Thus, in this study an in-depth TEM/STEM analysis of hematite photoanode was performed with high water oxidation activity. This study will provide new insights into the importance of textured structure and unintentional doping on hematite photoanode performance and also will provide pioneer analysis of the hematite/FTO interface.

2.2 Experimental Section

2.2.1 Materials

The FTO quartz substrate ware purchased from Solaronix S.A. Iron acetylacetonate (99.999%) and oleyl alcohol ($C_{18}H_{36}O$) were purchased from Aldrich Chemical Co.

2.2.2 Thin Film preparation method

The hematite thin film was prepared using the method described in reference 27. In a typical process, 4 $mg.mL^{-1}$ of magnetite nanocrystals solution (in chloroform) was dropped on TCO substrate, with a circular mask (0.19 cm^2), and dried at 50 ^oC. The magnetite film was sintered during 10 min. at 550 ^oC. This deposition/sintering process was repeated twice. For the film sintered at 1000 ^oC, we used a pre-sintered film at 550 ^oC (with 3 layers). After that, the pre-sintered film was treated at 1000 ^oC during 4 min, introducing the sample in the tubular furnace quickly.

2.2.3 FIB sample preparation

After photocurrent measurement, the hematite photoanode was washed with distilled water several times, and dried. The FIB sample was produced from the hematite photoanode films sintered at 550 ^oC and 1000 ^oC. The sample preparation was performed in a Helios Nanolab, DualBeam (FIB/SEM), FEI Company.

2.2.4 TEM/STEM Characterization

The TEM and STEM/EDS characterization were acquired on TECNAI F20 X-Twin, operating at 200 kV. For EDS map, a spot size of ~ 1.5 nm was used. For the composition profile, the spectrum was recorded to assure 1000 counts on the region of interest and quantified using Cliff-Lorimer k-factor

2.2.5 Photoelectrochemical Characterization

Photocurrent measurements were carried out in a standard three-electrode cell using the hematite film as the working electrode (0.19 cm^2) (Ag/AgCl in a KCl saturated solution as the reference electrode and platinum wire as a counter electrode). A 1.0 M NaOH (Aldrich, 99.99% in high pure water, pH=13.6, 25^oC) solution was used as the electrolyte. A scanning potentiostat (Potentiostat/Galvanostat μAutolab III) was used to measure the dark and illumination currents at a scan rate of 50mV/s. Sunlight (100 mW/cm^2) was simulated with a 450W xenon lamp (Osram, ozone free) and an AM1.5

filter. The light intensity was set at 100mW/cm^2. The incident photo-to-current conversion efficiency (IPCE) was measured as a function of the excitation wavelength (λ) using a 300 Xe lamp coupled to a Jobin-Ivon monochromator (typical light intensity of 940 μW/cm^2 at 500 nm). The IPCE was calculated by considering the following equation 2.1:[28]

$$IPCE=I(\lambda).1240/E(\lambda).\lambda \qquad (2.1)$$

where I(λ) is the photocurrent density (μA.cm^{-2}) and E(λ) is irradiance (μW.cm^{-2}).

2.3 Results and Discussion

Hematite thin films were produced by a magnetite nanocrystals deposition process.[27] The film was sintered at 550 ^{o}C and 1000 ^{o}C with rapid annealing to minimize damage to the substrate. Due to the high sintering temperature, FTO was deposited over pure silica glass as a TCO substrate. However, it is important to point out that the photocurrent data of the film sintered at 1000^{o}C showed low reproducibility. In this way, the film that showed the best photocurrent performance was used for further study. A high sintering temperature was intentionally used to intensify the tin diffusion on hematite film to understand the effect of this parameter on the texture and nanostructure of the film. The interface analysis characterization by TEM/STEM demands a cross-sectional analysis of the film/substrate. Due to the mesoporous nature of the hematite film, the conventional sample preparation technique is not appropriate to obtain thin samples. Thus, a focus ion beam (FIB) system was used to prepare high quality cross-sectional samples for HRTEM and STEM with energy dispersive X-ray spectroscopy (EDS) analysis. For HRTEM and STEM/EDS analyses, a TECNAI F20 FEI microscope was used which was operated at 200 kV. TEM/STEM analyses were performed on the same samples used for the photoelectrochemical characterization.

Figure 2.1a shows current potential curves of films sintered at 550^{o}C and 1000^{o}C under front-side illumination. Figure 2.1a illustrates that the photoanode prepared at 550^{o}C revealed very low activity for water oxidation (see inset); however, the photoanode sintered at 1000 ^{o}C resulted in very high activity. As a general trend, the hematite photoanode sintered at a high temperature under illumination produced a sharp increase in the photocurrent around 1.0 V_{RHE} which reached a plateau before the onset of the dark current. This photoanode reached a photocurrent of 1.8 mA.cm^{-2} at 1.23 V_{RHE} and 3.5

mA.cm^{-2} at 1.4 V_{RHE}. The incident photon conversion efficiency (IPCE) measurement (see Figure 2.1b) confirms the high efficiency of the mesoporous photoanode under front-side illumination. The film sintered at 1000 ^{o}C has IPCE values at 1.23 V of 24% around 400 nm.

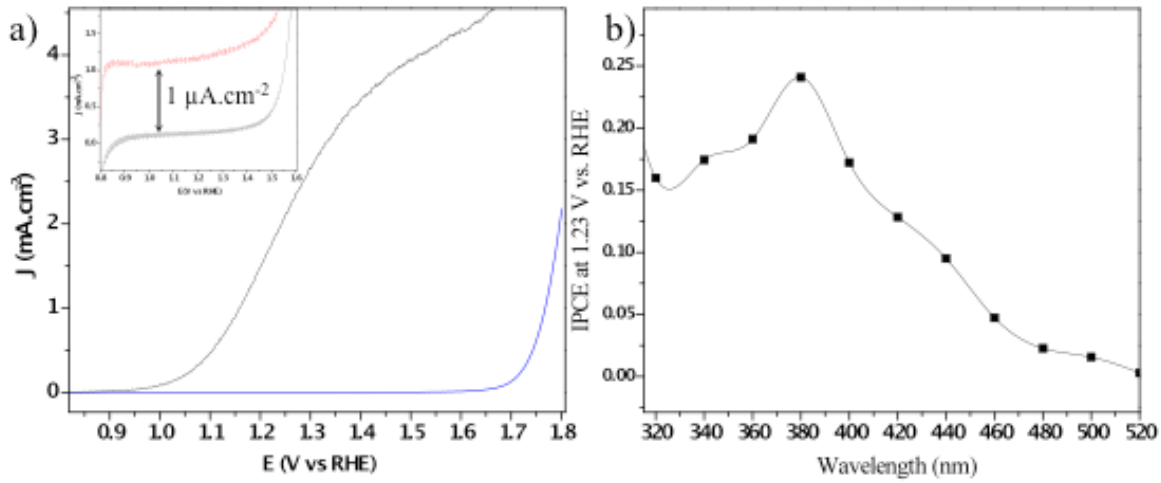

Figure 2.1 a) Current potential curves of films sintered at 1000 ^{o}C under front-side under illumination and in the dark (blue line). The inset shows in detail the film sintered at 550 ^{o}C; b) the incident photon conversion efficiency (IPCE) measurement for the film sintered at 1000 ^{o}C.

The photoelectrochemical characterization clearly shows the influence of sintering temperature on the hematite photoanode activity. To understand this dependence, a detailed structural, chemical and nanostructure characterization of the films sintered at 550^{o}C and 1000 ^{o}C was performed.

The top-view characterization by field emission scanning electron microscopy (FE-SEM) (see Figure 2.2) shows the nanostructured nature of films sintered at different temperatures. Both films are composed of elongated grains (typical size of 60 nm for the film sintered at 1000 ^{o}C and 20 nm for the film sintered at 550 ^{o}C) and open porosity, which characterizes a mesoporous film.

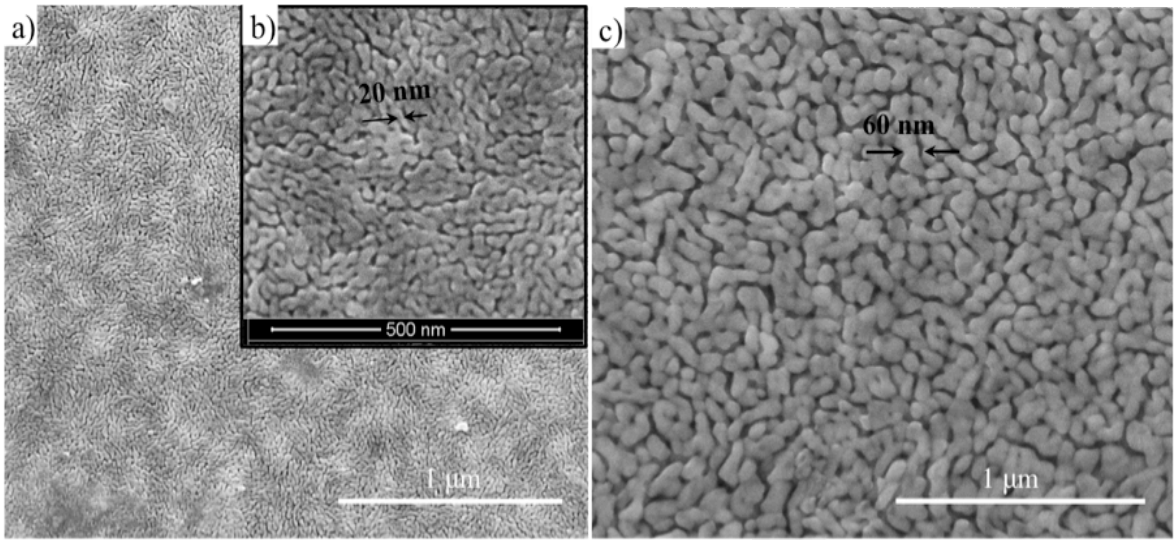

Figure 2.2 The film morphology was characterized by field emission-Scanning electron microscopy (FE-SEM-FEI Inspec F-50). FE-SEM images of hematite thin film. a) b) sintered 550 ^{o}C and c) 1000 ^{o}C

Figure 2.3 is a TEM/HRTEM cross-sectional view of the hematite thin film sintered in 550 ^{o}C. The first information obtained from the low magnification bright field (BF) TEM image (see Figure 2.3a) is the very poor solid-solid contact between the hematite film and the FTO film; only a few contact points are visible. In the high magnification BF-TEM image (see Figure 2.3b), unfilled spaces (gaps) between the FTO and hematite are evident with dimensions ranging from 20 nm to 5 nm. This very poor solid-solid contact is a direct consequence of a heating process that eliminates the solvent and organic compound and produces phase transformations (Fe_3O_4 is transformed to maghemite γ-Fe_2O_3, and γ-Fe_2O_3 is transformed to α-Fe_2O_3 around 450^{o}C). This microstructural observation clearly explains the very low activity measured for water oxidation for the photoanode sintered at 550^{o}C. In addition, the HRTEM image (see Figure 2.3c) of a contact point between the hematite and the FTO shows an incoherent interface (an interface between two phases where there is no lattice matching). This image shows that the hematite is oriented along the [211] zone axis, and the FTO is oriented along [001] zone axis.

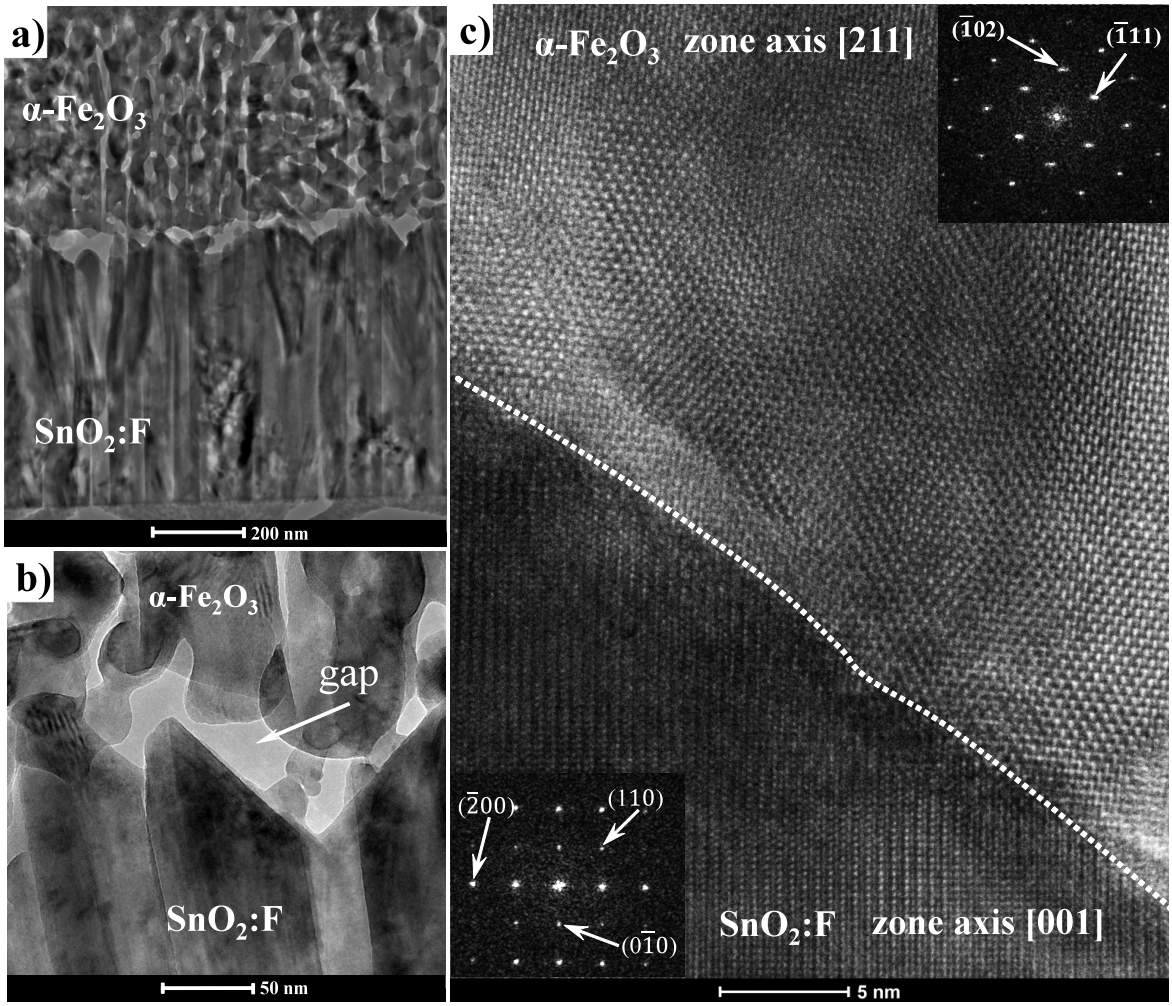

Figure 2.3 Cross-sectional TEM images of the hematite thin film sintered in 550 ^{o}C. a) Low magnification BF-TEM image; b) high magnification BF-TEM image; c) HRTEM image of the FTO/α-Fe_2O_3 interface. A dashed line has been added at interface as a guide to the eyes. Insets: fast Fourier transform (FFT) analysis of the hematite and SnO_2, showing the zone axis of each phases.

The photoanode sintered at 1000 ^{o}C was also characterized by TEM/HRTEM cross-sectional analysis. Figure 2.4a shows a low magnification BF-TEM image of this sample, and the first evident detail is the improvement of the hematite/FTO solid-solid interface and the formation of a mesoporous film with a columnar hematite structure. Figure 2.4b is a high magnification BF-TEM image of the interface highlighting the absence of an unfilled space and a much better solid-solid contact. Several hematite/FTO interfaces were analyzed by HRTEM, and incoherent and semi-coherent interfaces were observed. Figure 2.4c is the HRTEM image of a semi-coherent interface between hematite (α-Fe_2O_3) and FTO. The image analysis shows that α-Fe_2O_3 and SnO_2 phases are oriented along the [110] and [100] zone axis which indicates an epitaxial interface relationship between the $(012)_{\alpha\text{-}Fe2O3}$ and $(110)_{SnO2}$ planes ($(012)_{\alpha\text{-}Fe2O3}$ //$(110)_{SnO2}$). Also Figure 2.4c

shows a peculiar stripe contrast, which is related to the presence of dislocations at the interface. These dislocations are formed at the interface to offset some of the coherency strain required to maintain matching between crystalline planes. Considering that the relative strain (ε) due to the misfit of the lattice is given by $\varepsilon \approx |d_{(012)\alpha\text{-}Fe2O3} - d_{(110)SnO2}|/d_{(012)\alpha\text{-}Fe2O3}$, where $d_{(012)\alpha\text{-}Fe2O3}$ and $d_{(110)SnO2}$ are the (110) and (012) unstressed interplanar distance of SnO_2 and hematite, respectively, we can estimate a $\varepsilon \approx 19\%$ which characterizes a semi-coherent interface. For instance, a coherent interface is possible for the epitaxial interface relationship between the $(110)_{\alpha\text{-}Fe2O3}$ and $(101)_{SnO2}$ planes ($(110)_{\alpha\text{-}Fe2O3}$ //$(101)_{SnO2}$), with $\varepsilon \approx 3.8\%$ and $(110)_{\alpha\text{-}Fe2O3}$ //$(200)_{SnO2}$ with $\varepsilon \approx 4\%$; however, these interfaces were not observed in the present study.

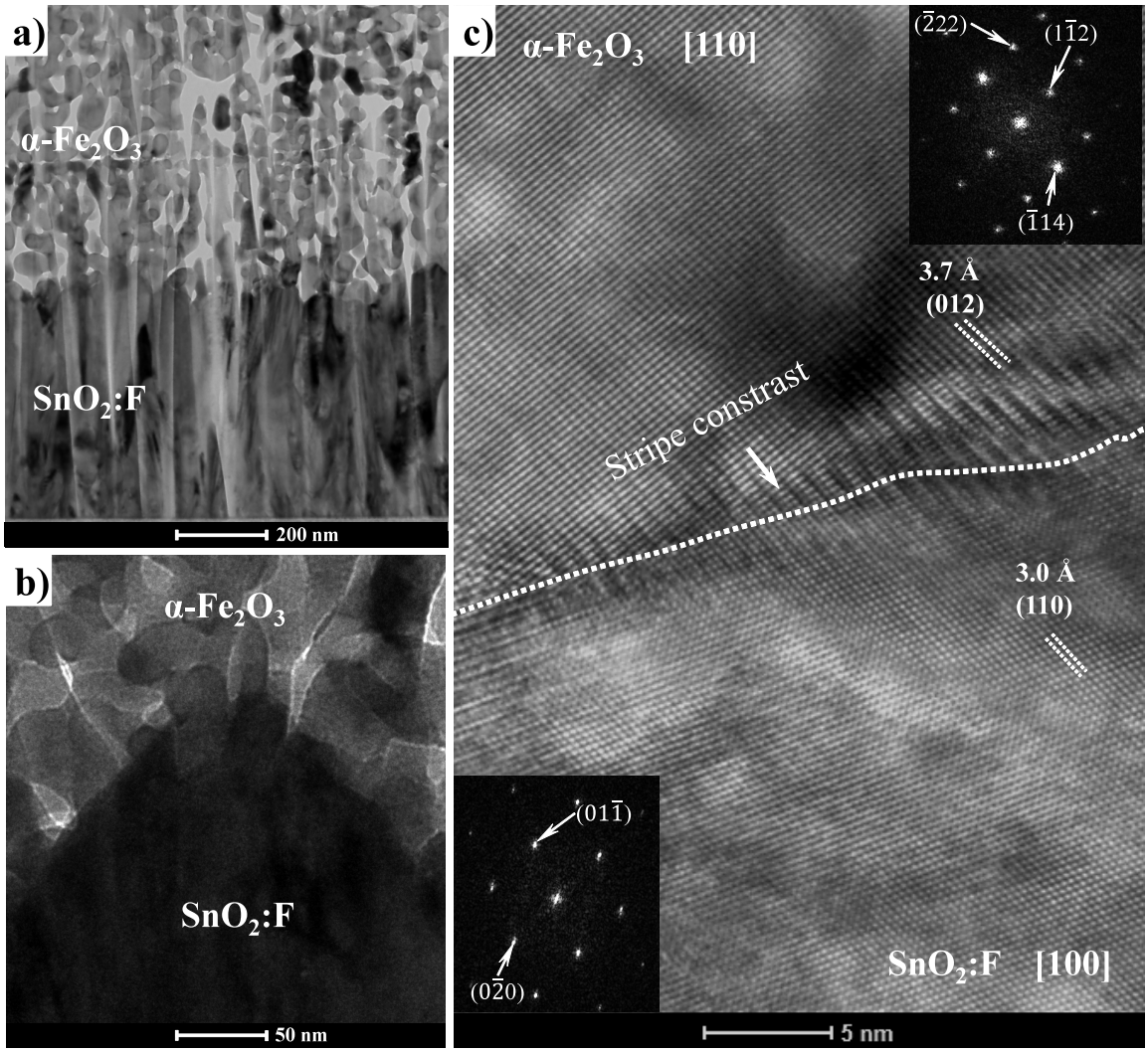

Figure 2.4 Cross-sectional TEM images of the hematite thin film sintered in 1000 ^{o}C. a) Low magnification BF-TEM image; b) high magnification BF-TEM image; c) HRTEM image of the FTO/α-Fe_2O_3 interface. A dashed line has been added at interface as a guide to the eyes. Insets: FFT analysis of the hematite and SnO_2, showing the zone axis of each phases.

XRD and cross-sectional TEM analyses of the TCO used in this study (see Figures 2.5a and 2.5b) indicate morphology and structure, which are schematically illustrated in Figure 2.5c. An analysis of this figure reveals that this morphology and texture are not favorable for the formation of a coherent interface, which suggests that the TCO substrate morphology has a fundamental impact on the type of interfaces in the hematite photoanode. Any improvement in the interface between the hematite and the TCO will necessarily demand the development of a TCO with a different morphology and

preferential orientation.

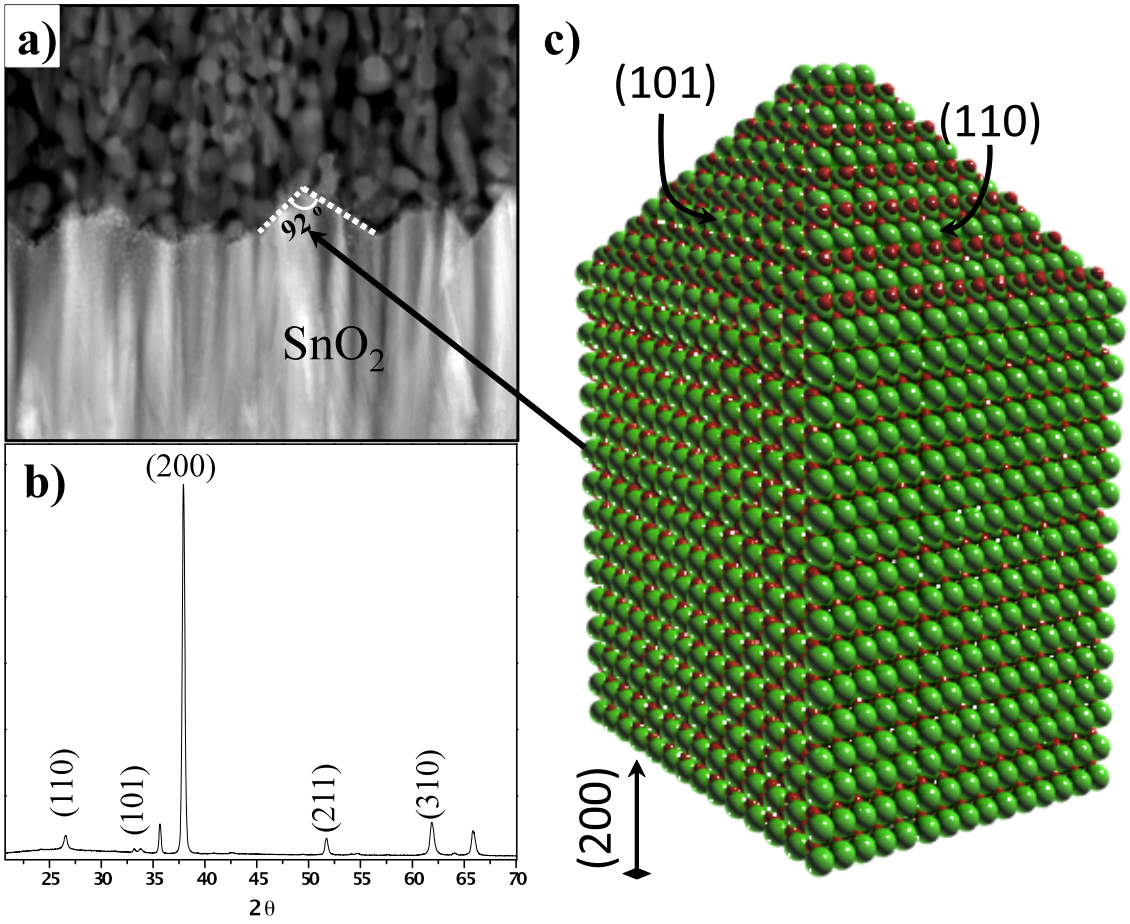

Figure 2.5 a) XRD; b) cross-sectional TEM analysis of the TCO used in this work (sample sintered at 1000°C); c) schematic representation of the FTO morphology based on TEM and XRD analysis.

Figure 2.6 shows an XRD analysis of the hematite films sintered at 550°C and 1000 °C. In both samples a preferential orientation of the hematite film in the [110] axis vertical to the substrate was observed. However, normalizing the peak intensity of the (110) plane by the peak intensity of the (104) plane of hematite, the film sintered at 1000 °C shows a value of normalized intensity four times higher than the hematite thin film sintered on 550 °C which indicates a higher degree of orientation. This result shows that the increase in the sintering temperature has a direct impact on the degree of orientation.

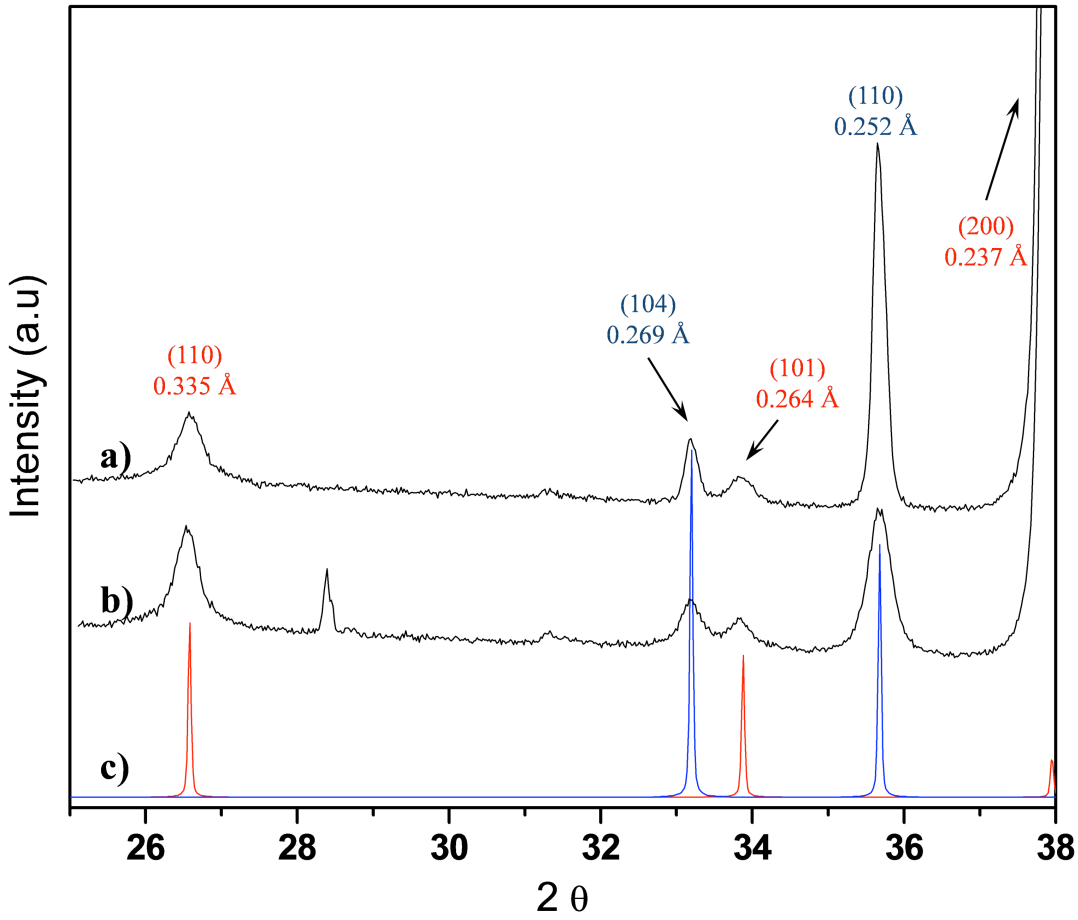

Figure 2.6 XRD pattern of a hematite thin film sintered at two different temperatures: a) 1000 °C; b) 550 °C; c) standard of hematite (blue) (JCPDS-ICDD PDF card No. 33-0664) and standard of cassiterite (JCPDS-ICDD PDF card No. 41-1445) (red).

In our previous research, the unintentional doping by tin (Sn^{4+}) was not detected by X-ray photoelectron spectroscopy and EDS analysis for a hematite film sintered at 820°C.[27] However, in the present study, the sintering temperature was intentionally increased to enhance the inter-diffusion process in the hematite/FTO interface. To characterize this process, an STEM-EDS analysis was performed with a spatial resolution better than 1.5 nm and a high exposure time which assured a good signal-to-noise ratio and reliable results. For this study, EDS elemental mapping images and a concentration line profile analysis was used. The image drift during the acquisition process was correct when the initial high annular dark field (ADF) image was used as a reference. Figure 2.7 illustrates the STEM-EDS analysis of the film sintered at 1000 °C. Figure 2.7a is a low magnification ADF image of the hematite/FTO interface which highlights the region analyzed by EDS (see Figure 2.7b-c). Figure 2.7b shows the X-ray elemental map of the region illustrated in Figure 2.7a. A well-defined interface is evident between the hematite

and the SnO_2 (FTO), which suggests a very low inter-diffusion region. To quantitatively estimate the inter-diffusion region, a line profile analysis was performed in the region shown in Figure 2.7c (as illustrated in Figure 2.7d). The results show a diffusion length of ~40 nm for Sn in hematite and a ~60 nm diffusion length for Fe in FTO. A line profile analysis of other interfaces produced very similar results. An important point is that EDS point analysis far from the interface which was run with a very high exposure time (more than 6 min.) did not detect Sn in the hematite film. These results demonstrate that the diffusion of Sn occurs only in a limited region of the interface (only 40 nm). Thus, it is plausible to assume that the unintentional doping by Sn^{4+} is not significant for hematite photoanode performance for water oxidation because the hematite film has a thickness of 700 nm. Another critical point is that Fe diffusion into the FTO can cause modification in the TCO substrate electronic properties.

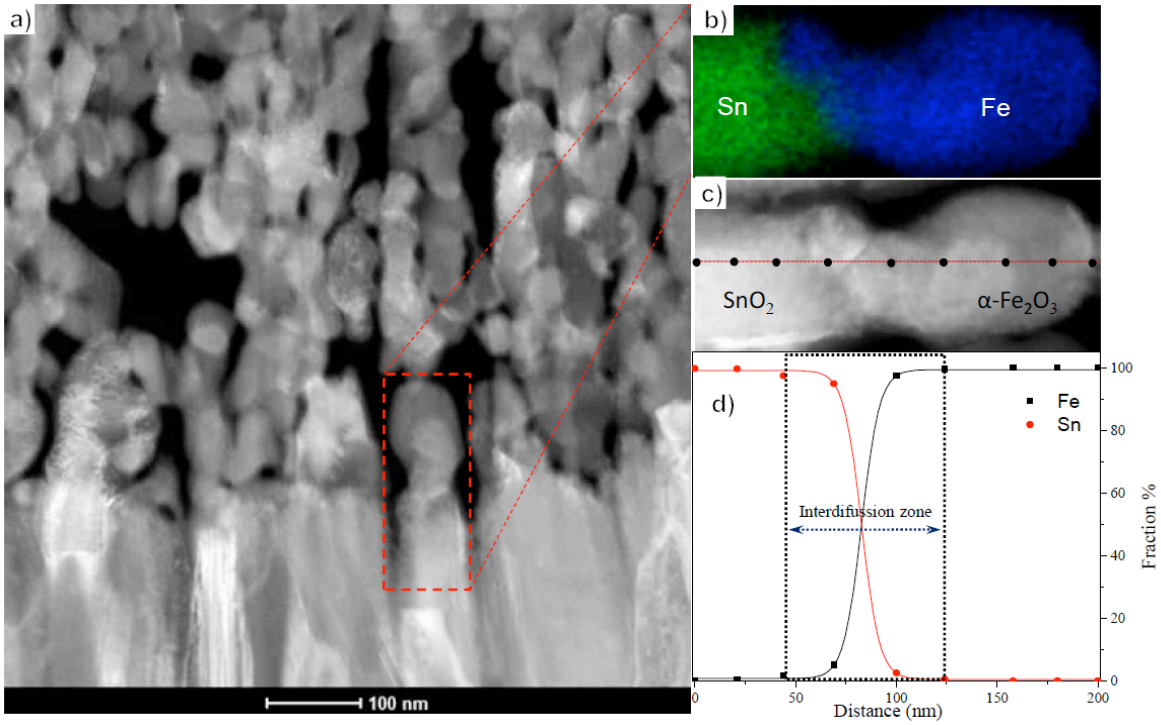

Figure 2.7. STEM-EDS analysis of a film sintered at 1000 ^{o}C; a) low magnification ADF-STEM image b) STEM-EDS elemental X-ray map for Sn (L-line) in green and Fe (L-line) in blue; c) inset of ADF-STEM image where EDS line profile analysis was performed; d) profile of the composition for Fe and Sn at the interface region.

A detailed microstructural characterization of the film sintered at 1000 ^{o}C shows the sintering temperature has a strong influence on the growth of a mesoporous hematite thin film with a columnar grain structure textured in the [110] zone axis. The grain and pore size analysis after the sintering process reveals an intense grain growth process, and the

STEM-EDS analysis indicates the formation of an inter-diffusion layer at the hematite/FTO interface which is initiated by unintentional doping of ~100 nm. The mechanism that promoted the textured thin film with a columnar morphology is unknown; however, it may be related to a grain growth process based on rearrangement between particles followed by coalescence. This rearrangement also promotes the formation of an interface free of unfilled space which improves the solid-solid contact. The photoelectrochemical characterization also revealed that this photoanode has very good activity for water oxidation with a photocurrent of 1.84 $mA.cm^{-2}$ at 1.23 V_{RHE}.

The excellent performance of the photoanode sintered at 1000 ^{o}C must be related to the preferential growth of the hematite film along the [110] axis as the influence of the unintentional doping of hematite with Sn^{4+} is limited to a thinner layer in the FTO interface. Actually, for the first time, the preferential growth direction with the water-splitting activity can be correlated without the interference of intentional or unintentional doping. Two beneficial effects of the preferential growth along the [110] axis of the hematite film in the performance of the photoanode can be identified. First, hematite has an anisotropic conductivity; i.e., the electronic conductivity along the (001) plane is four orders of magnitude higher than in any perpendicular plane.[21] This high charge (electron) mobility must contribute to more efficient charge separation in the water oxidation process. Second, elongated textured hematite grains along the [110] axis have a high fraction of the (001) surface. It is generally accepted that, in relation to other hematite surfaces, the (001) surface is relatively inert (in water) to the protonation and deprotonation reactions required for charge accumulation.[21] As proposed in our previous paper[27], this behavior can favorably decrease the hematite surface trapping state in a water-based electrolyte which contributes to water photo-oxidation.

2.4 Conclusions

In this study, HRTEM and STEM-EDS with high spatial resolution analyses were combined to obtain an in-depth nanostructural characterization of a textured hematite photoanode with columnar grains obtained by the colloidal deposition of magnetite nanocrystals. Our study is the first attempt to describe in detail the structure and chemistry of the α-Fe_2O_3/FTO interface, which identifies semi-coherent and incoherent interfaces as well as a localized an inter-diffusion layer of Sn and Fe at the interface (~100 nm in length). Actually, the nanostructural characterization clearly shows that interface quality is an important issue that must be taken into account in future studies of hematite photoanodes. The correlation of the nanoscale morphology with photoelectrochemical characterization facilitates the identification of the beneficial effect of the preferential growth direction of the hematite film along the [110] axis in water-splitting efficiency. We anticipate that the results described in this study will also be relevant to the development of a hematite photoanode with higher efficiency and will foster the exploration and development of better (coherent) hematite/TCO interfaces as well as improve nanocrystal deposition to achieve columnar hematite completely oriented in the (110) direction.

2.5 References

1. Dare-Edwards, M.P.; Goodenough, J.B.; Hamnett, A.; Trevellick, P.R. Electrochemistry and photoelectrochemistry of iron(III) oxide. *J. Chem. Soc., Faraday Trans.* **,** 79, 2027-2041, **1983.**

2. Itoh, K.; Bockris, J.O. Stacked thin-film photoelectrode using Thin-film photoelectrochemistry – iron-oxide. *J. Electrochem. Soc*. 131, 1266, **1984**.

3. Bjorkstbn, U.; Moser, J.; Gratzel, M. Photoelectrochemical studies on nanocrystalline hematite films. *Chem. Mater*. 6, 858-863, **1994**.

4. Murphy, A. B.; Barnes, P. R. F.; Randeniya, L. K.; Plumb, I. C.; Grey, I. E.; Horne, M. D.; Glasscock, Efficiency of solar water splitting using semiconductor electrodes. J. A. *Int. J.Hydrogen Energy 31*, 1999–2017, **2006**.

5. Kennedy, J.; Frese, K. J. Photooxidation of Water at α-Fe_2O_3 Electrodes. *Electrochem. Soc*. 125, 709, **1978**.

6. Morin, F. J. Electrical properties of alpha-Fe_2O_3 and alpha Fe_2O_3 containing titanium

Phys. Rev. 83, 1005, **1951**.

7. Walter, M. G.; Warren, E.L.; McKone, J. R.; Boettcher, S. W.; Mi, Q.; Santori, E. A.; Lewis, N. S. Solar Water Splitting Cells. *Chem. Rev. 110,* 6446–6473, **2010.**

8. Sivula, K.; Le Formal, F.; Grätzel, M. Solar Water Splitting: Progress Using Hematite (α-Fe_2O_3) Photoelectrodes. *ChemSusChem*, 4, 432-449, **2011**.

9. Tilley, S. D.; Cornuz, M.; Sivula, K.; Gratzel, M. Light-Induced Water Splitting with Hematite: Improved Nanostructure and Iridium Oxide Catalysis. *Angew. Chem. Int. Ed.* 49, 1-5, **2010**.

10. Lin, Y.; Zhou, S.; Sheehan, S. W.; Wang, D. Nanonet-based hematite heteronanostructures for efficient solar water splitting. *J. Am. Chem. Soc.*, *133* (8), 2398–2401, **2011**.

11. Le Formal, F.; Gratzel, M.; Sivula, K. Controlling Photoactivity in Ultrathin Hematite Films for Solar Water-Splitting. *Adv. Funct. Mater.* 20, 1099–1107, **2010**.

12. Klahr, B. M.; Martinson, A. B. F., Hamann, T. W. Photoelectrochemical investigation of ultrathin film iron oxide solar cells prepared by atomic layer deposition. *Langmuir,* 27(1), 461–468, **2011**.

13. Lukowski, M. A.; Jin S. Improved Synthesis and Electrical Properties of Si-Doped α-Fe_2O_3 Nanowires. *J. Phys. Chem. C* 115, 12388–12395, **2011**.

14. Jang, J. S.; Lee, J.; Ye, H.; Fan, F. R. F.; Bard, A. J. Rapid Screening of Effective Dopants for Fe_2O_3 Photocatalysts with Scanning Electrochemical Microscopy and Investigation of Their Photoelectrochemical Properties *J. Phys. Chem. C* 113 (16), 6719–6724, **2009**.

15. Satsangi, V. R.; Kumari, S.; Singh, A. P.; Shrivastav, R.; Dass, S. Iron doped TiO_2 for photoelectrochemical generation of hydrogen. Int. J. Hydrogen Energy 33 (1), 312–318, **2008**.

16. Ling, Y.; Wang, G.; Wheeler, D.A.; Zhang, J. Z.; Li Y. Sn-doped hematite nanostructures for photoelectrochemical water splitting. *Nano Lett.*, *11* (5), 2119–2125, **2011**.

17. Sivula, K.; Zboril, R.; Formal, F. Le; Robert, R.; Weidenkaff, A.; Tucek, J.; Frydrych, J.; Gratzel, M. Photoelectrochemical Water Splitting with Mesoporous Hematite Prepared by a Solution-Based Colloidal Approach. J. *Am. Chem. Soc.* 132, 7436–7444, **2010**.

18. Iordanova, N.; Dupuis, M.; Rosso, K. M. Charge transport in metal oxides: A theoretical study of hematite alpha-Fe_2O_3. *J. Chem. Phys. 122*, **2005**.

19. Nakau, T. Electrical conductivity of alfa-Fe_2O_3 *J. Phys. Soc. Jpn.* 15, 727, **1960**.

20. Benjelloun, J. P. D.; Bonnet, J. P.; Doumerc, J. C.; Launay, M.; Onillon, P.; Hagenmuller. Anysotropic electronic properties of the Iron Oxide (α-Fe_2O_3) *Mater. Chem. Phys.* 10, 503, **1984**.

21. Yanina, S. V.; Rosso, K. M. Linked Reactivity at Mineral-Water Interfaces Through Bulk Crystal Conduction. *Science*. 320, 218-222, **2008**.

22. Kay, A.; Cesar, I; Gratzel, M. New Benchmark for Water Photooxidation by Nanostructured α-Fe_2O_3 Films. *J. Am. Chem. Soc*. 128, 15714, **2006**.

23. Cesar, I.; Sivula, K.; Kay, A.; Zboril R.; Gratzel M. Influence of Feature Size, Film Thickness and Silicon Doping on the Performance of Nanostructured Hematite Photoanodes for Solar Water Splitting. *J. Phys. Chem. C*, *113* (2), 772–782, **2009**.

24. Campbell, A. S.; Schwertmann, U.; Stanjek, H.; Friedl, J.; Kyek, A.; Campbell, P. A. Si incorporation into hematite by heating Si- ferrihydrite. *Langmuir 18*, 7804-7809, **2002**.

25. Vayssieres, L.; Beermann, N.; Lindquist S. E.; Hagfeldt, A Controlled Aqueous Chemical Growth of Oriented Three-Dimensional Crystalline Nanorod Arrays: Application to Iron (III) Oxides. *Chem. Mater*. 13, 233, **2001**.

26. Hahn, N. T.; Ye, H.; Flaherty, D.W.; Bard A. J.; Mullins C. B. Reactive Ballistic Deposition of α-Fe_2O3 Thin Films for Photoelectrochemical Water Oxidation. *ACS Nano*, *4* (4), 1977–1986, **2010**.

27. Gonçalves, R.H.; Lima B. H. R.; Leite, E. R. Magnetite Colloidal Nanocrystals: A Facile Pathway To Prepare Mesoporous Hematite Thin Films for Photoelectrochemical Water Splitting. *J. Am. Chem. Soc*., *133* (15), 6012–6019, **2011**.

28. Murphy, A. B.; Barnes, P. R. F.; Randeniya, L. K.; Plumb, I. C.; Grey, I. E.; Horne, M. D.; Glasscock, Efficiency of solar water splitting using semiconductor electrodes. J. A. *Int. J. Hydrogen Energy 31*, 1999–2017, **2006**.

Chapter 3. The colloidal nanocrystal deposition process: an advanced method to prepare high performance hematite photoanodes for water splitting

3.1 Introduction

Decades ago, K. L. Hardee and A. J. Bard researched hematite (a-Fe_2O_3) as a potential material for photoelectrochemical devices due to its ability to absorb visible light as well as its chemical stability in an alkaline medium and the abundance of this element.[1] The subsequent quest for the direct solar-to-chemical conversion higher efficiency of hematite photoanodes was aggressively pursued. Hematite has a small optical absorption coefficient and poor electronic properties due to its short minority carrier (holes) diffusion lengths.[2-5] Despite this intrinsic disadvantage, many excellent research projects have demonstrated good photoelectrochemical performance for hematite thin films,[6-11] which can be associated with morphological control at the nanoscale through a suitable thin film deposition process.

Among relevant deposition methods, which were investigated to process hematite photoanodes, the atmospheric pressure chemical vapor deposition (APCVD) method is a benchmark with a photocurrent value of 2.2 $mA.cm^{-2}$ at 1.23 V_{RHE} without co-catalysis under standard air mass 1.5 illumination.[12] Atomic layer deposition (ALD) is also a powerful technique to produce high quality thin films;[13] e.g., nanonet-based hematite hetero-structural growth by ALD achieved 1.6 $mA.cm^{-2}$ at 1.23 V_{RHE}.[14] Another interesting strategy is the growth of a hematite nanorod by hydrothermal and sintering processes that have been widely studied and show excellent photocurrent results.[15]

For the last three years, our research group has been working on a CND process to prepare hematite and other semiconductor oxide photoanodes with excellent activity for water splitting.[16] In this study, we demonstrate significant progress by using CND to prepare hematite thin films by introducing the following modifications in the original process as described in ref. 16: (a) the deposition of maghemite (α-Fe_2O_3) instead of magnetite; (b) the introduction of a magnetic field during the dip coating process; and (c) the introduction of an intentional doping.

Scheme 1 illustrates the magnetic field-assisted dip coating process to produce hematite thin films on the FTO substrate. The maghemite colloidal nanocrystal solution is stored in a Teflon container designed to externally couple two parallel magnets (see Figure 3.1). A similar strategy was used to process the doped hematite photoanode; however, intentional doping was performed by the addition of a specific amount of tin (IV) tert-butoxide as a tin precursor which was chosen due to its solubility in toluene and because it is halogen-free.

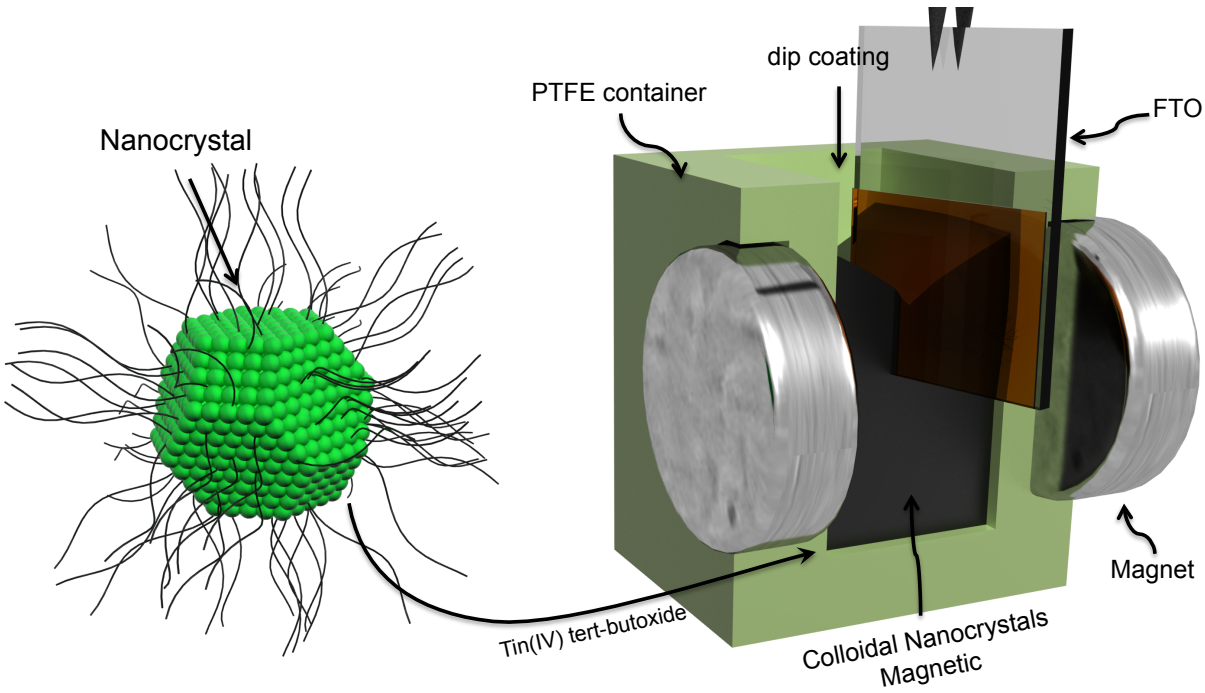

Figure 3.1. Magnetic field-assisted dip coating process to produce hematite thin films on the FTO substrate.

3.2 Experimental Procedure

3.2.1 Materials.

Iron acetylacetonate (III) (99.99%), tin (IV) tert-butoxide, oleyl alcohol and oleic acid were purchased from Aldrich Chemical Co and FTO/aluminum borosilicate was purchased from Solaronix S.A.

3.2.2 Magnetite/maghimite nanocrystals

Magnetite (Fe_3O_4) was synthesized using the method described in reference [16]. In this synthesis, 12 g of iron (III) acetylacetonate were solubilized in 100 ml of oleyl alcohol. This solution was heated to 260 ºC for 1 h under nitrogen atmosphere. After this reaction time, the colloid, which formed, was cooled and separated with the addition of 300 ml of acetone and the assistance of an external magnetic field. The separated nanocrystals were re-dispersed in 20 mL of toluene and centrifuged at 14,000 rpm for 5 min to remove nanocrystal agglomerates. The magnetite nanocrystals were transformed to maghimite (γ-Fe_2O_3) to avoid Fe^{2+}; oxygen gas was bubbled into the magnetite colloid at 120 ºC for 2 h. This transformation can be identified by the brownish color of the colloid. Finally, the nanocrystal concentration was adjusted to 190 $mg.mL^{1}$.

3.2.3 Tin doping precursor

Initially, a tin stock solution was prepared with the addition of 1 mmol of tin (IV) tert-butoxide in 1:1 ml of toluene/oleic acid. The oleic acid was used to stabilize the organometallic precursor in toluene and to protect against hydrolyzation.

3.2.4 Thin film preparation

Prior to the deposition, the FTO substrate (typical size 2 cm x 1 cm) was washed with an HCl/HNO_3 solution for 30 min and rinsed several times with pure water. Then the same substrate was immersed in a sodium hydroxide solution for 30 min and again rinsed with pure water; finally, the substrate was dried at 110 ºC for 2 hours. The colloidal nanocrystal deposition was carried out by a magnetic field-assisted dip coating process. First, a container was fitted with two N50 grade (1.4 T) NdFeB magnets (see figure 3.1 and Figure 3.2 for details regarding this container). For undoped hematite, 2 mL of concentrated stock dispersion (190 $mg.mL^{-1}$) of maghimite colloid was added between these magnets, and the dip coating process was completed with an insertion speed of 60 mm/min and withdrawal speed of 80 mm/min. (see dip coating process detail in the Figure S1c). Under optimized conditions, the nanocrystaline thin film was rapidly inserted into a furnace tube at 850 ºC and quickly removed after 20 min. The doped hematite thin film was produced with colloidal maghemite nanocrystals, which were adjusted in the same concentration (190 $mg.mL^{-1}$), and an 8 wt% tin (IV) tert-butoxide was added. The doped

thin film was inserted into a furnace at 850 ºC and removed directly to room temperature after 3 min of heat treatment.

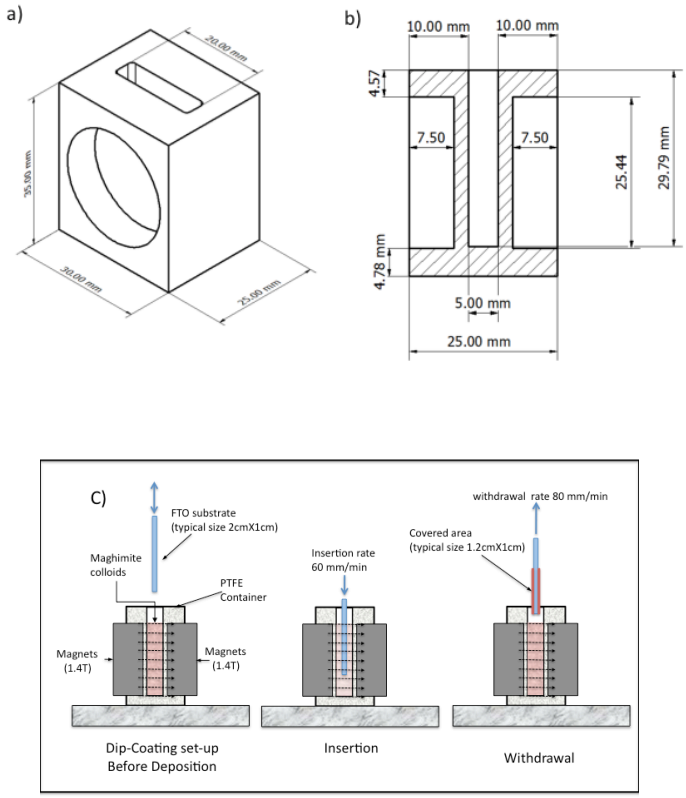

Figure 3.2 Dimensions of the PTFE container used in the dip-coating process with a magnetic field); a) Perspective image; b) cross-sectional image of the container with the dimensions; c) details about the dip-coating process.

3.2.5 Photoelectrochemical characterization

Photoelectrochemistry measurements were conducted in a standard three-electrode cell by using: 1) the hematite film as the working electrode (the working surface area was 0.19 cm^2); 2) Ag/AgCl in a KCl saturated solution as the reference electrode; and 3) the platinum plate as a counter electrode. A 1.0 M NaOH solution (Aldrich, 99.99%) in highly pure water (pH=13.6 at 25 ºC) was used as the electrolyte. A scanning potentiostat (Potentiostat/Galvanostat μAutolab III) was used to measure the dark and illuminated currents at a scan rate of 20 mV/s. Sunlight (100 mW/cm^2) was simulated with a 250 W Xenon lamp (Osram, ozone free) and AM1.5 filter (Newport Corp.). The incident photo-to-current conversion efficiency (IPCE) was measured as a function of the excitation wavelength (λ) using a 300 xenon lamp coupled monochromator (QE/IPCE measurement) (KIT Newport Corp.). The IPCE plot was calculated by considering the following the

equation of reference [16]. The electrochemical impedance spectroscopy (EIS) measurement was taken in a NaOH solution under dark conditions using a Metrohm autolab Model PGSTA T204. The Nyquist plot was constructed from 1.75 V_{RHE} to 0.8 V_{RHE} for both doped and undoped hematite; the Mott- Schottky plot was extracted in the linear region at 1 kHz. For the Mott-Schottky analysis, the geometric area was corrected by multiplying its value by a roughness factor which was estimated by an atomic force microscopy (AFM) measurement. Roughness factors used for undoped and Sn-doped hematite films were 15.6 and 6.2, respectively. For the roughness factor calculation, the film and hematite single crystal roughness measured by AFM (roughness factor = film hematite roughness/hematite single crystal roughness) was considered.

3.3 Results and Discussion

Henceforth, all the results reported in this chapter are related to photoanodes prepared by the CND process with the magnetic field applied during the dip-coating process. First, we optimized the sintering process for the undoped hematite thin film in different ranges of temperatures and times. Figure 3.3 displays the photocurrent density as a function of the sintering time for undoped hematite sintered at 800 ºC and 850 ºC. This temperature range was chosen because below 800 ºC a very low photocurrent is observed. The reproducibility is affected drastically above 850 ºC due to uncontrollable grain growth or substrate damage. For undoped hematite, the best photoresponse was obtained at 850 ºC with a soaking time of 20 min, as can be seen in Figure 3.3b. At these sintering parameters, a photocurrent of 1.4 $mA.cm^{-2}$ at 1.23 V_{RHE} and a plateau of 1.9 $mA.cm^{-2}$ at 1.5 V_{RHE} were achieved under standard AM 1.5 G illumination (see the current–potential curve in Figure 3.4). In our previous study,[16a] we reported a photocurrent value of 1.1 $mA.cm^{-2}$ at 1.23 V_{RHE} for a film formed by six layers of hematite with a thickness higher than 900 nm. Modifications implemented in the CND process (i.e., the magnetic field and the use of maghemite) produced a highly oriented film, which was formed by a single layer of hematite with a 27% improved photocurrent.

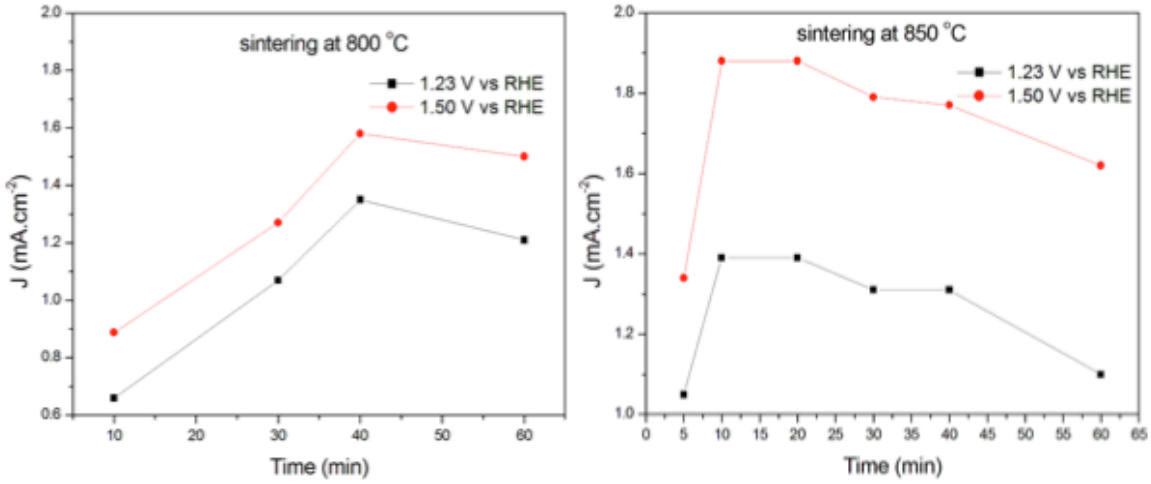

Figure 3.3. Current density (at 1.23 V_{RHE}) vs. sintering time for the undoped hematite thin film: a) Sintered at 800 ºC and b) Sintered at 850 ºC.

As the undoped hematite achieved the best photocurrent value when sintered at 850 ºC, we selected this sintering temperature to study the effect of the addition of Sn on the photoelectrochemical performance of the hematite photoanode prepared by using the CND process. At this stage, we also evaluated the optimum concentration of the Sn precursor in relation to the concentration of maghemite nanocrystals. The best concentration was 8% of precursor in relation to the maghemite weight. As illustrated in Figure 3.4, the photocurrent achieved a value of 2.7 $mA.cm^{-2}$ at 1.23 V_{RHE} and reached a plateau of 3.8 $mA.cm^{-2}$ at 1.5 V_{RHE} for the Sn-doped hematite thin film. The photocurrent at 1.23 V_{RHE} of the Sn-doped sample increased by 93% as compared to the undoped sample.

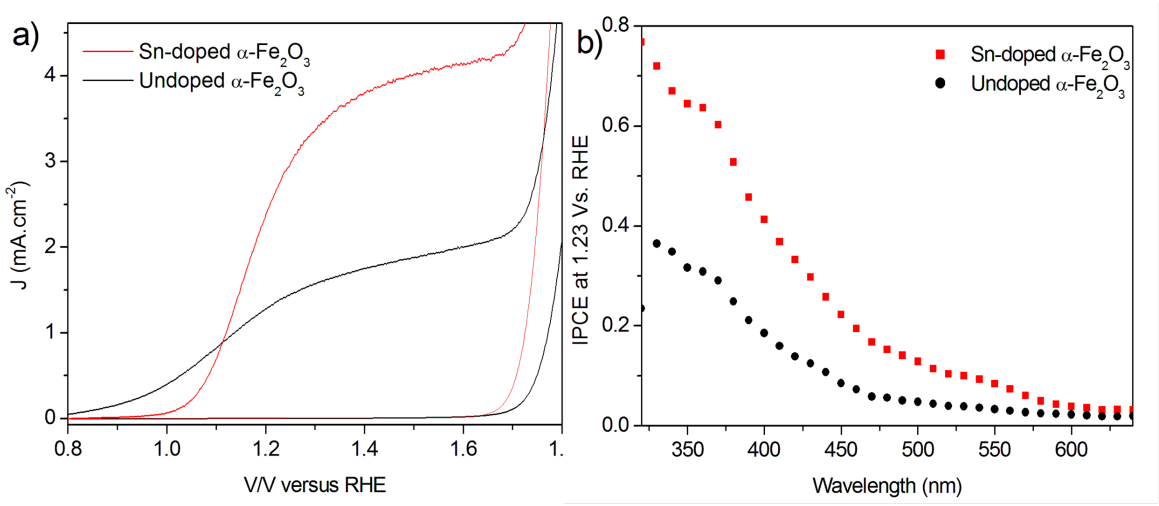

Figure 3.4 Photoelectrochemical analysis of a hematite photoanode prepared by CND. (a) Current density–potential curve of Sn-doped hematite (red line – sintered at 850 ºC per 3 min) and undoped hematite (black line – sintered at 850 ºC per 20 min) under simulated solar light and dark conditions; (b) incident photon-to-current efficiency (IPCE) plots versus wavelength of Sn-doped hematite (diamond markers) and undoped hematite (circle markers); the IPCE was measured at 1.23 V_{RHE}.

IPCEs were realized for both Sn-doped and undoped photoanodes at 1.23 V_{RHE}. An IPCE value of 78% at 320 nm and 40% at 400 nm was observed for Sn-doped hematite thin films (see Figure 3.4b – red squares). IPCEs of 39% at 320 nm and 20% at 400 nm were measured for undoped hematite (black dots), which validates the higher value of IPCE in the wavelength range analyzed for doped hematite as compared to the undoped material. Basically, the shorter wavelength photons have high penetration depth when compared with higher wavelength photons. It means that photons with higher energy can photoexcited electrons from bulk and depletion layer, according to Gartner model. The lower energy photons are limited to photoexcited electron from depletion layer. This hypothesis explains the significant difference in the IPCEs collected at 320 nm and at 500 nm, for both undoped and doped hematite. Integrating the overlap of IPCE data measured at 1.23 V_{RHE} with the solar irradiance spectrum AM1.5/100 mW.cm^{-2} gives calculated photocurrent values of 2.6 mA.cm^{-2} and 1.3 mA.cm^{-2} for Sn-doped hematite and undoped hematite, respectively, which are similar to values measured by the current–potential curve and confirms that the employed light source simulated the AM1.5 solar emission. Note that this value is comparable to or even higher than the best photocurrent values reported for hematite without a catalyst which was prepared by using the APCVD process or the hydrothermal method.[12,15] In addition, the Sn-doped hematite chronoamperometry measurement showed excellent stability (see Figure 3.5) that demonstrates the most important parameter for hematite photoanode studies.

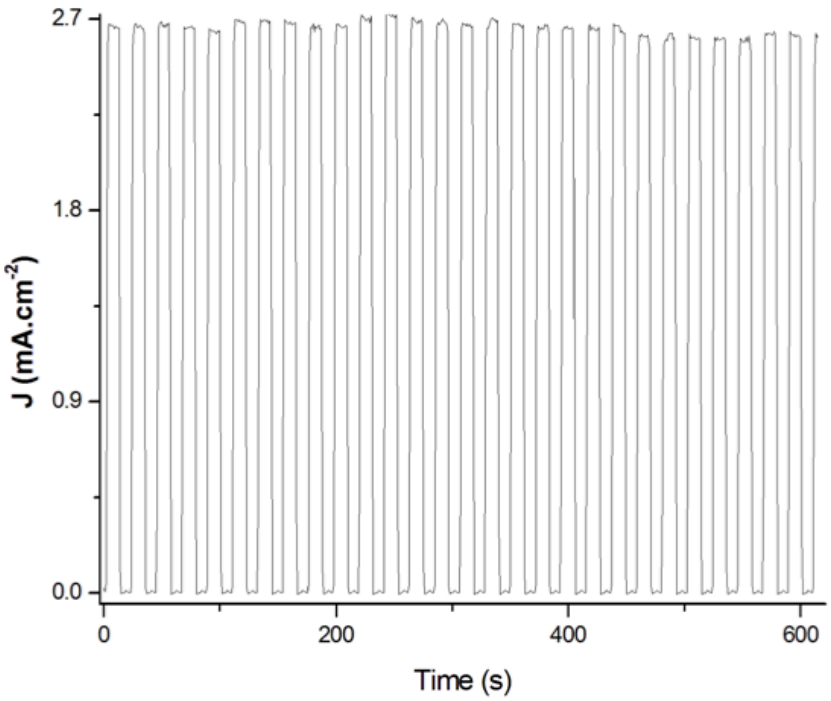

Figure 3.5. Chronoamperometry test, performed at 1.23 V_{RHE}, which shows electrochemical stability for the Sn-doped hematite photoanode.

During the development of doped and undoped hematite photoanodes prepared by the CND process, we evaluated the influence of the magnetic field using a photocurrent density at 1.23 V_{RHE} as a figure of merit. Note that a single deposition layer was used to avoid several rounds of dip coating and sintering steps. MR fluids are materials, which show a reversible transition from a liquid to a nearly solid state in the presence of external magnetic fields. In the absence of a magnetic field, MR fluids behave as Newtonian fluids. Furthermore, when a magnetic field is applied (transverse to the direction of flow) a yielding, shear thinning and viscoelastic behavior is observed.[17] These modifications, which are induced by the magnetic field in the γ-Fe_2O_3 colloidal dispersion, have a direct impact on the dip-coating process and facilitate the preparation of films with thicknesses ranging from 150–250 nm, in a single step (see Figure 3.6). Note that the magnetic field improves the photoelectrochemistry performance during the deposition process. Even with multiple deposition circles (without a magnetic field), photoanodes did not achieve the same performance as photoanodes processed with an external magnetic field. The undoped hematite photoanode was sintered at 850 ºC for 20 minutes, and the Sn-doped hematite photoanode was sintered at 850 ºC for 3 min. The film thickness is indicated in the Figure legend for the films prepared without the magnetic field. The thickness was collect by cross-sectional SEM images.

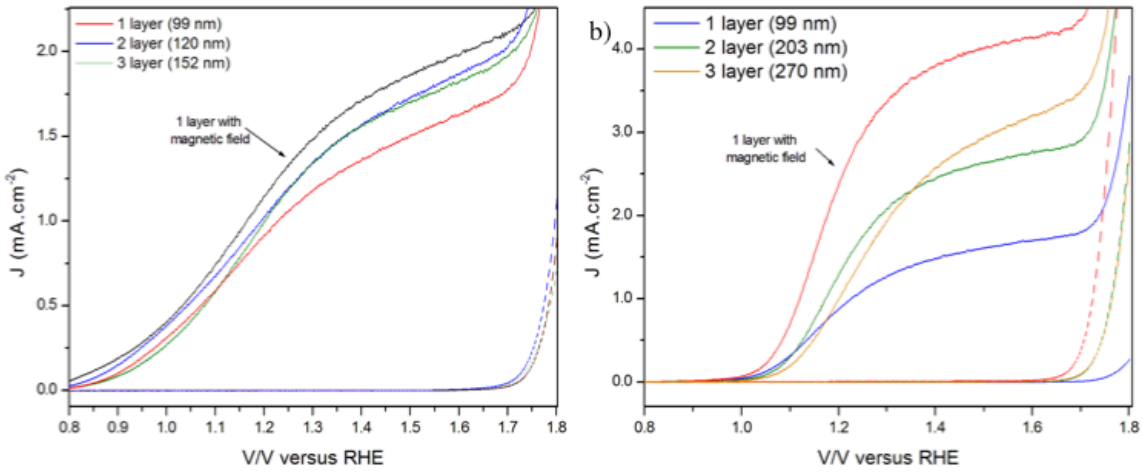

Figure 3.6. Comparison of the photocurrent versus potential curves for hematite produced with and without a magnetic field applied during the dip-coating deposition process: a) Undoped hematite; and b) Sn-doped hematite.

The influence of the magnetic field on the undoped and Sn-doped hematite photoanode performance (assessed by J at 1.23 V_{RHE}) and nanostructure is summarized in Table 3.1. The use of a magnetic field during the dip-coating process produces an increase in the photocurrent and the film thickness. Note that photoanodes processed by multiple deposition steps without the application of a magnetic field did not demonstrate a better photoelectrochemical performance for water splitting (see Figure 3.6).

Table 3.1 Influence of the magnetic field applied during the dip-coating process on the photocurrent density at 1.23 V_{RHE} and thin film thickness of undoped and Sn-doped hematite photoanodes[a]

	With magnetic field		Without magnetic field	
α-Fe_2O_3 photoanode	Undoped	Sn-doped	Undoped	Sn-doped
Thickness[b] (nm)	180	250	91	99
J@1.23 V_{RHE} (mA cm^{-2})	1.4	2.7	1.0	1.1

[a] Samples sintered at 850 °C. [b] Measured by cross-sectional FE-SEM images.

We believe that the influence of the magnetic field on the CND process is associated with the γ-Fe_2O_3 colloidal dispersion magnetorheological (MR) fluid behavior employed in this study (see Figure 3.7).

Figure 3.7. Photography of vials containing maghemite colloidal dispersion without the influence of magnetic field and under the influence of an external magnetic field. We can notice that there is no phase separation between the nanoparticles and the solvent. The entire dispersion is attracted by the magnetic filed. This is a typical behavior of MR fluid.

The X-ray diffraction (XRD) analysis performed on the film after the sintering process shows the formation of a hematite phase with a preferential orientation along the [110] axis vertical to the substrate (see Figure 3.9). Figure 3.8a and c illustrate top view and cross-sectional analyses of the undoped hematite film, which was characterized by field emission scanning electron microscopy (FE-SEM). The top view analysis (see Figure 3.8a) shows the nanostructured nature of the film with elongated grains (with the smallest feature size in the range of 75 nm) and open porosity. The cross-sectional analysis (see Figure 3.8c) shows a film formed by columnar grains with a thickness of 180 nm and note that a single column of hematite grains forms the film.

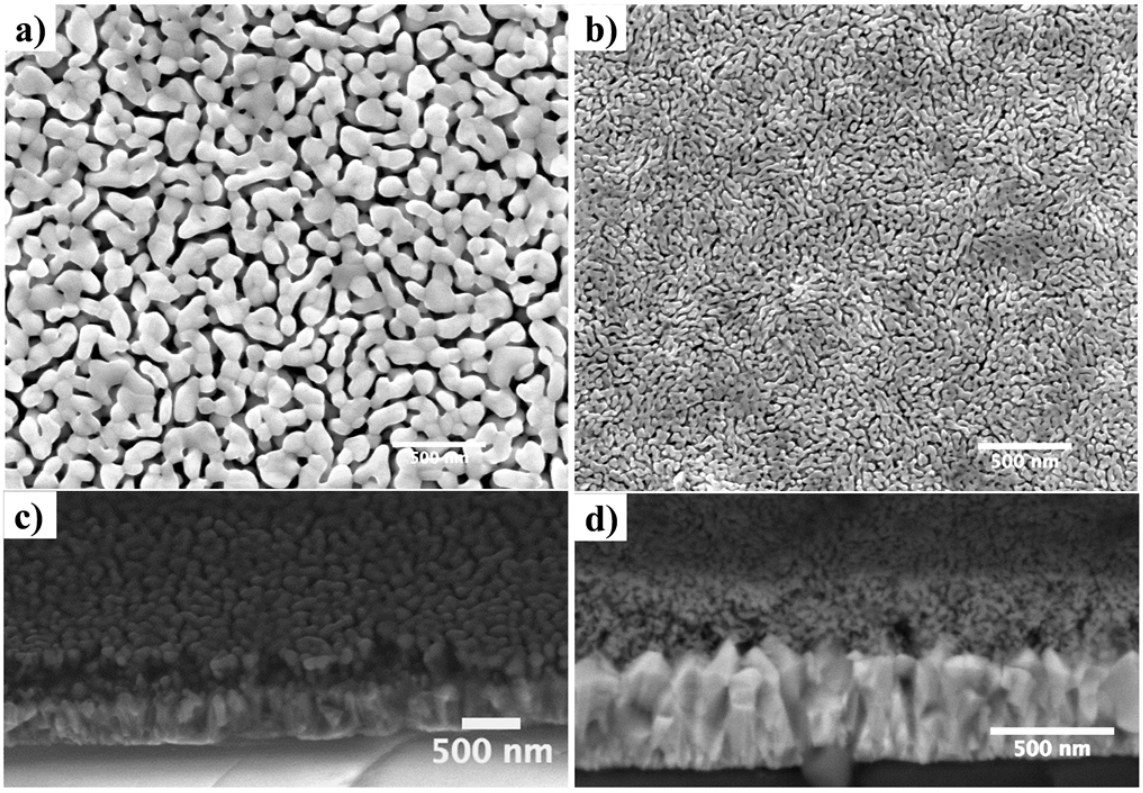

Figure 3.8 FE-SEM images of hematite thin films obtained by CND. (a) Top view image of undoped hematite annealed at 850 ºC for 20 min. (b) Top view image of Sn-doped hematite annealed at 850 ºC for 3 min; (c) and (d) are cross-sectional images of undoped and Sn-doped hematite, respectively. All images are in the same magnification.

The cross-sectional FE-SEM images were also performed in hematite thin film produced without magnetic field and single layer of deposition. The Figure 3.9a and b shows details of top views for undoped and doped, respectively. It is clear, the magnetic field have no influence the grain growth because undoped hematite grain has approximated the same size and the same segregation behavior is noted in doped hematite thin film. However, the main modification is associated with thickness of hematite thin film, as can be seen Figure 3.9. An applausive explanation for this difference is viscosity behavior in the absence of magnetic field. The thickness of both undoped and doped hematite thin film was less than 50 nm.

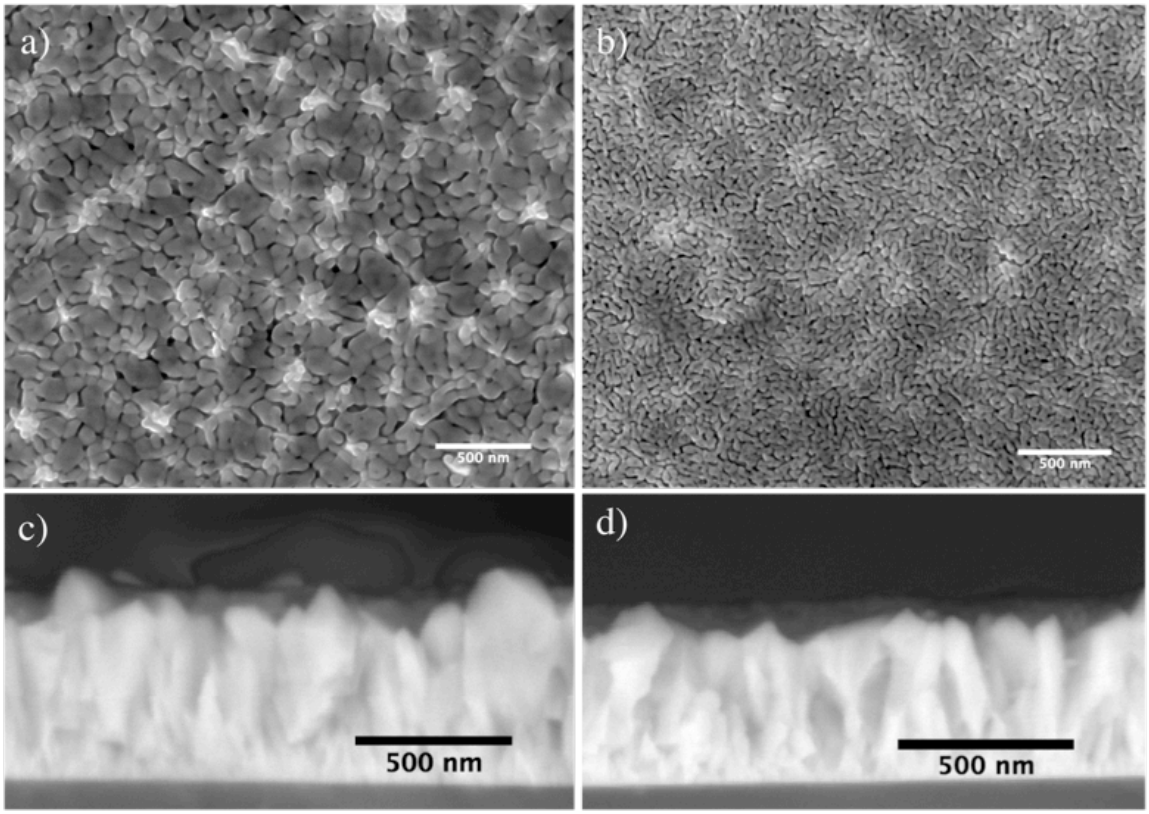

Figure 3.9 Comparison of SEM images of hematite thin films produced by CND without magnetic field: a) undoped hematite; and b) doped hematite.

The cross-sectional analysis by transmission electron microscopy (TEM) and high-resolution transmission electron microscopy (HRTEM) (see Figure 3.10) confirms the formation of columnar grains with a good interface between the hematite and FTO and the coherent grain boundary between hematite grains (see Figure 3.10) FE-SEM and TEM/HRTEM analyses of the undoped film reveal an unexpected nanostructural evolution after the sintering process.

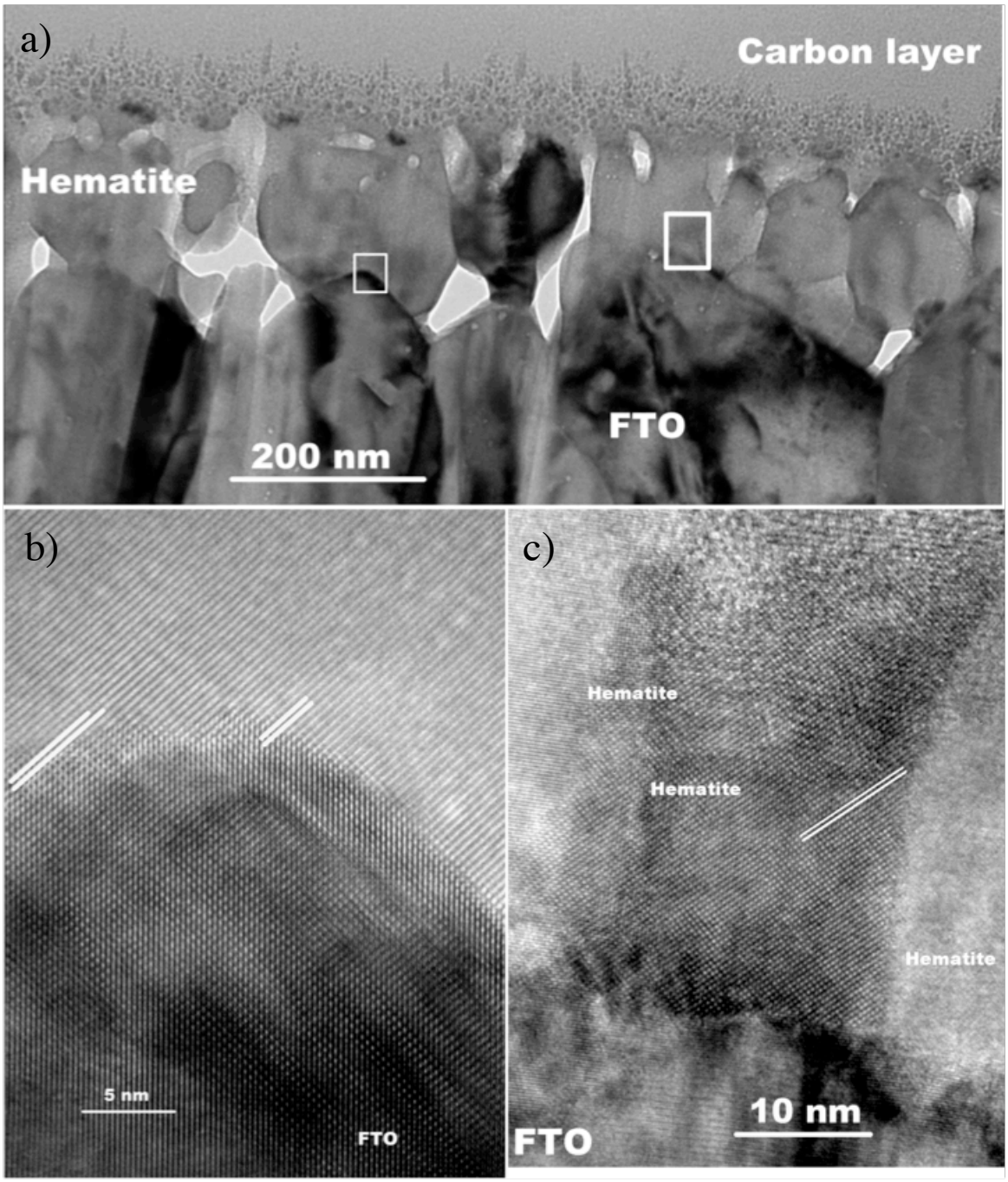

Figure 3.10. TEM and HRTEM cross-sectional analysis of the undoped hematite photoanode: a) Low magnification bright field TEM image showing the columnar structure; b) HRTEM image of the FTO/Hematite interface; and c) HRTEM image showing a coherent hematite grain boundary.

The XRD analysis of the Sn-doped film after the sintering process reveals the formation of a hematite phase with no traces of the undesired phase. As observed in the undoped film, this sample also showed a preferential orientation along the [110] axis vertical to the substrate (see Figure 3.11). Crystallite sizes, which were calculated by the Scherrer equation, for undoped and doped hematite were 78 nm and 41 nm, respectively. The FE-SEM analysis (see Figure 3.8c and d) supports the XRD analysis and shows an

impressive decrease in the grain size with the addition of Sn. These results strongly suggest that during the sintering process, Sn^{4+} segregation occurs along solid–solid and solid–gas surfaces which hinders the grain growth process.[15,18] The cation segregation can promote either a decrease in the grain boundary mobility or a surface energy reduction. Both phenomena will contribute to a decrease in the grain growth rate.[18–21]

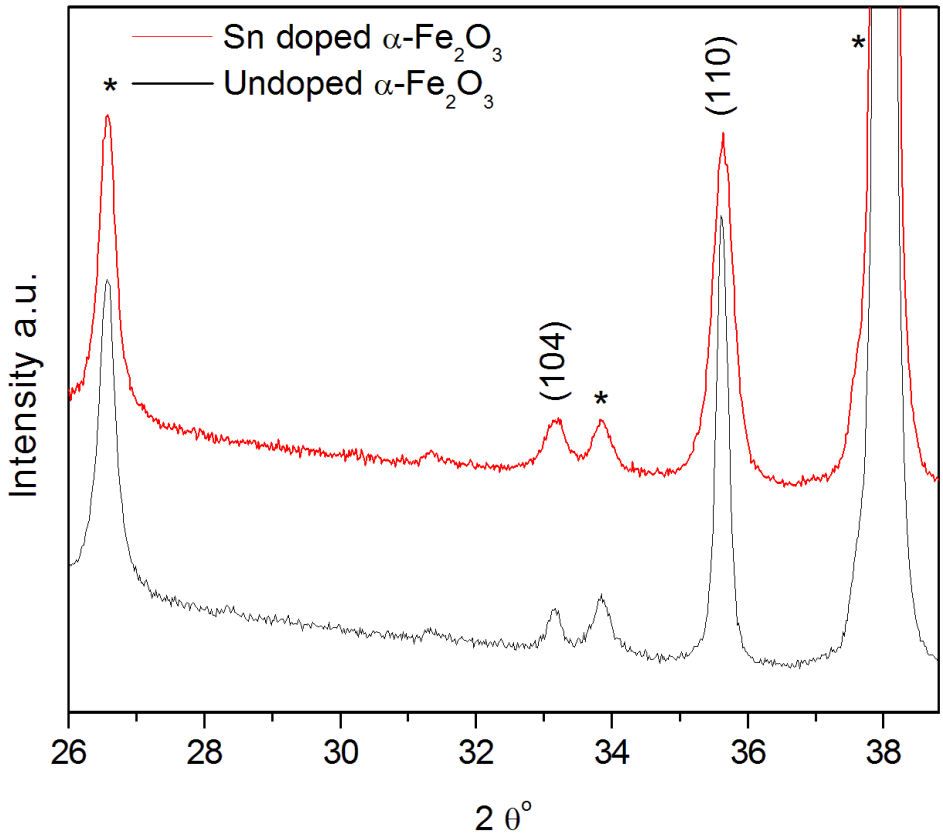

Figure 3.11. XRD pattern for both Sn-doped (red line) and undoped (black line) hematite thin films. * Indicates SnO_2 peak from the TCO substrate.

The segregation phenomenon was investigated by scanning transmission electron microscopy (STEM) with X-ray energy dispersive analysis (EDS) in the film cross-section. As illustrated in Figure 3.12, the line profile EDS analysis along the hematite grain showed an Sn enrichment in the grain surface which confirms the segregation process. Note that the undoped sample did not show any sign of impurities (see the STEM-EDS analysis in Figure 3.12). The cross-sectional analysis performed by STEM and FE-SEM (see Figure 3.8d) shows a mesoporous film formed by elongated grains with a thickness of 250 nm. Note that after the Sn addition, the columnar structure disappears.

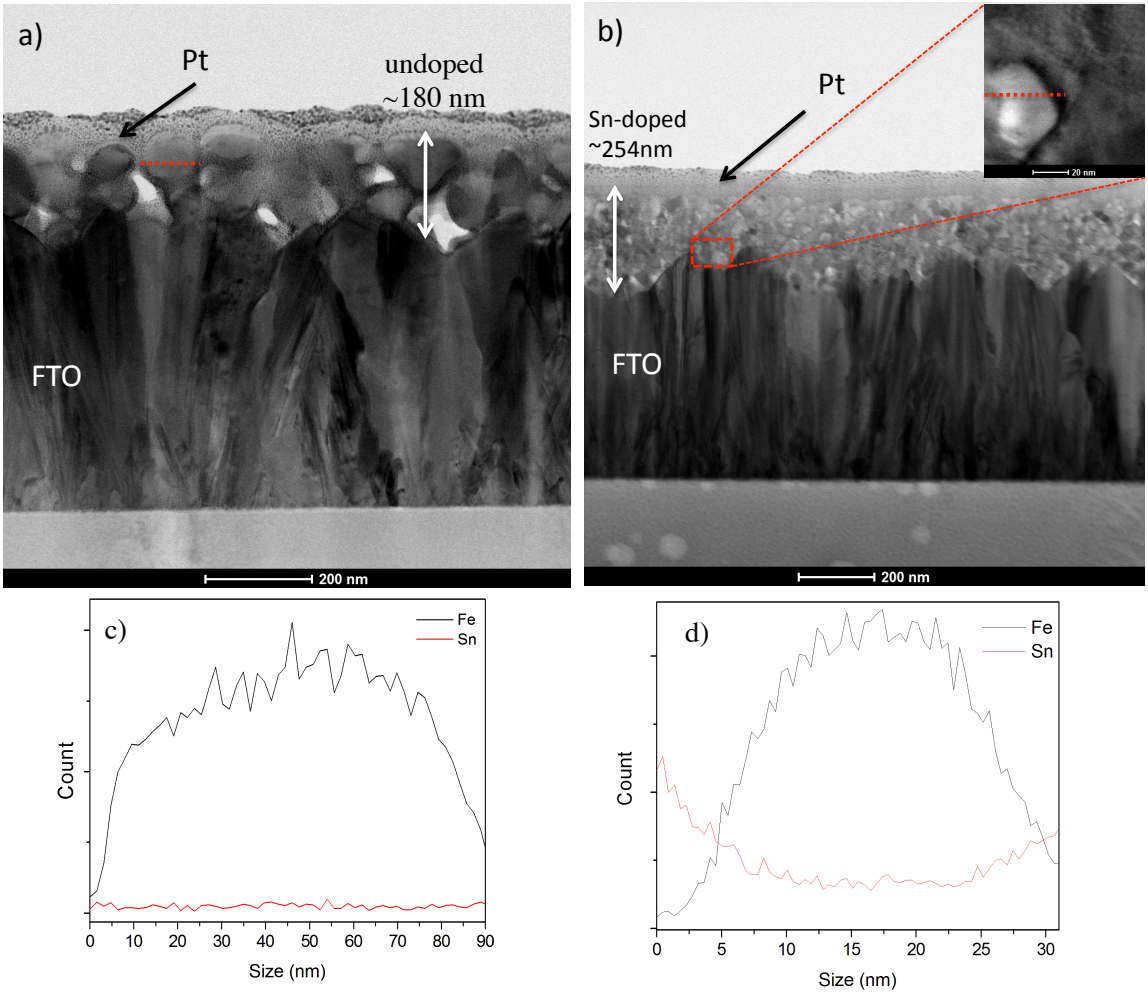

Figure 3.12 STEM cross-sectional image of a) Undoped hematite with a thickness of ~180 nm, b) STEM image of Sn-doped hematite with a thickness of ~254 nm, c) plot corresponding to the line scan (EDX) for undoped hematite (the red line in the figure (a) shows the analyzed region and d) the EDX line scan for Sn-doped hematite (the red line in the inset shows the analyzed region).

To obtain a better understanding of the effect of the Sn addition on the photoelectrochemistry of the doped hematite photoanode, electrochemical impedance spectroscopy (see details in Figure 3.13 and Table 3.3) and a Mott–Schottky analysis were performed to estimate the donor density (ND) and the flat band potential (V_{fb}). Figure 13a displays the Mott–Schottky plot for doped and undoped hematite thin films recorded in the absence of light. A good linear fit (with $R^2 > 0.99$ for both samples) was obtained in the bias range from 0.9 to 1.4 V_{RHE} with a positive slope, which is typical of an n-type semi-conductor. ND and V_{fb} values measured for both films are listed in Table 3.2.

Table 3.2 Fitted parameters obtained from the equivalent circuit diagram used to simulate and to fit the Nyquist plot of hematite photoanodes (Figure 3.13)

Hematite Photoanode	N_D (cm^{-3})	V_{fb} (V_{RHE})
Undoped	$1.3x10^{18}$	0.40
Sn-doped	$1.7x10^{18}$	0.94

The ND value analysis was unchanged and corresponds to $1.3x10^{18}$ cm^3 and $1.7x10^{18}$ cm^3 for undoped and Sn-doped photoanodes, respectively. This result suggests that Sn does not act as an electronic dopant. In contrast, clearly the addition of Sn promotes a significant anodic shift of the V_{fb} in relation to the undoped film. The increase in the V_{fb} must be associated with Sn enrichment in the hematite grain surface. The increase of the V_{fb} promotes an increase in band bending, which can contribute to the charge separation process.[22]

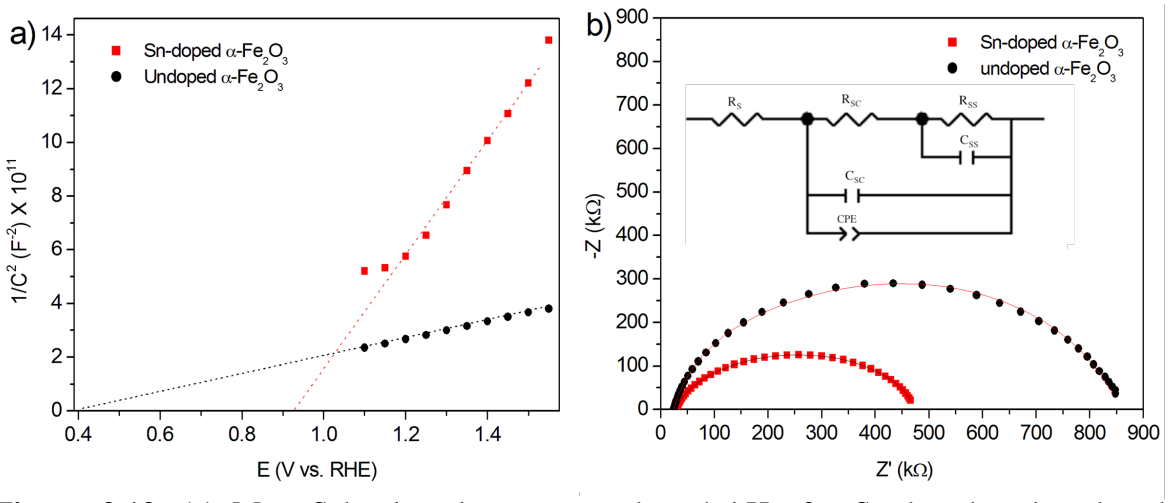

Figure 3.13. (a) Mott–Schottky plots measured at 1 kHz for Sn-doped and undoped hematite photoanodes. The flat-band potential is determined on the linear fit slope intercept for both curves; (b) Nyquist plot of the electrochemical impedance spectroscopy analysis for Sn-doped and undoped hematite thin films measured at 1.75 V_{RHE}.

In addition, defining the pseudo-overpotential for water oxidation (η_{Ox}) as the difference between the onset voltage for a photocurrent (V_{on}) under standard illumination conditions and the V_{fb} i.e., $\eta_{Ox} = (V_{on} - V_{fb})$,[23] there is a small value of η_{Ox} (0.1 V) for the doped photoanode as compared to the undoped film (0.4 V). We therefore performed a simple qualitative electrochemical impedance spectroscopy analysis to determine the effect of the addition of Sn on the η_{Ox}. The Sn-doped anode Nyquist plot showed a semicircle with a smaller diameter when compared to an undoped hematite anode, which indicates a

smaller charge transfer resistance. These results suggest that the Sn segregation layer in the hematite surface facilitates the charge transfer at the semiconductor–liquid junction. The exact effect of Sn segregation on the charge transfer is unknown. However, clearly the association of a smaller charge transfer resistance with a higher surface area contributes to a superior photoelectrochemical performance for water splitting of the doped photoanode.

Table 3.3 N_D and V_{fb} values extracted of Mott-Schottky plot for both thin films.

	Rs (Ω)	Rsc (Ω)	Rss (Ω)	Css (F)	Csc (F)	CPE1-T(s^p/Ω)	CPE1-P (0.8-1)	q^2
Undoped	24.84	57.35	798.7	1.0776E-6	2.239E-7	2.0447E-5	0.63806	3.303E-5
Sn-Doped	28.88	24.55	448	2.4987E-7	7.3382E-7	7.2885E-5	0.56131	1.78E-4

3.3 Conclusions

In conclusion, we improved the CND process by using the deposition of maghemite (γ-Fe_2O_3) nanocrystals and by introducing the magnetic field during the dip coating process to improve the thin film deposition method, which is mainly due to the MR fluid behavior of this colloid. These modifications produced a highly oriented and transparent thin film formed by a single layer of hematite (thickness ~180 nm) with a photocurrent of 1.4 $mA.cm^{-2}$ at 1.23 V_{RHE}. We also introduced an intentional doping and added a Sn precursor during the deposition process. The photocurrent achieved for the doped photoanode was 2.7 $mA.cm^{-2}$ at 1.23 V_{RHE}. The improvement in the photocurrent is attributed to an increase in band-bending and to a smaller charge transfer resistance associated with a higher surface area; this behavior is facilitated by the addition of Sn.

3.4 References

1. Hardee, K. L.; Bard, A. J. Semiconductor Electrodes V. The Application of Chemically Vapor Deposited Iron Oxide Films to Photosensitized Electrolysis *J. Electrochem. Soc*., 123, 1024–1026, **1976**.

2. Itoh, K.; Bockris, J. O. Thin Film Photoelectrochemistry: Iron Oxide *J. Electrochem. Soc*., 131, 1266, **1984.**

3. Morin, F. Photooxidation of Water at α – Fe_2O_3 Electrodes *J. Electrochem. Soc*., 125, 709, **1978**.

4. Dare-Edwards, M. P.; J. B. Goodenough, A. Hamnett and P. R. Trevellick, Electrochemistry and photoelectrochemistry of iron(III) oxide *J. Chem. Soc., Faraday Trans*., 79, 2027–2041, **1983**.

5. Gleitzer, C.; Nowotny, J.; Rekas, M. Surface and bulk electrical properties of the hematite phase Fe_2O_3 *Appl. Phys. A: Solids Surf.,* 53(4), 310–316, **1991.**

6. Tilley, D. S.; Cornuz, M.; Sivula, K.; Gratzel, M. Light-Induced Water Splitting with Hematite: Improved Nanostructure and Iridium Oxide Catalysis, *Angew. Chem., Int. Ed*., 49, 1–5, **2010.**

7. Sivula, K.; Zboril, R.; Formal, F. L.; Robert, R.; Weidenkaff, A.; Tucek, J.; Frydrych J. ; Gratzel, M. Photoelectrochemical Water Splitting with Mesoporous Hematite Prepared by a Solution-Based Colloidal Approach. *J. Am. Chem. Soc*., 132, 7436–7444, **2010**.

8. Klahr, B. M.; Martinson, A. B. F.; Hamann, T. W. Photoelectrochemical Investigation of Ultrathin Film Iron Oxide Solar Cells Prepared by Atomic Layer Deposition, *Langmuir*, 27, 461–468, **2011**.

9. Formal, F. Le; Graetzel, M.; Sivula, K. Controlling Photoactivity in Ultrathin Hematite Films for Solar Water-Splitting *Adv. Funct. Mater*., 20, 1099–1107, **2010**.

10. Li, L.; Yu, Y.; Meng, F.; Tan, Y.; Hamers, R. J.; Jin, S.; Facile Solution Synthesis of α-$FeF_3 \cdot 3H_2O$ Nanowires and Their Conversion to α-Fe_2O_3 Nanowires for Photoelectrochemical Application. *Nano Lett*., 12, 724–731, **2012**.

11. S. C. Warren, K. Voitchovsky, H. Dotan, C. M. Leroy, M. Cornuz, F. Stellacci, C. Hebert, A. Rothschild and M. Gratzel, Identifying champion nanostructures for solarwater-splitting *Nat. Mater*., 12, 842–849, **2013**.

12. A. Kay, I. Cesar and M. Gratzel, New Benchmark for Water Photooxidation by Nanostructured α-Fe2O3 Films. *J. Am. Chem. Soc*., 128(49), 15714–15721, **2006**.

13. (a) N. T. Hahn, H. Ye, D. W. Flaherty, A. J. Bard and C. B. Mullins, Reactive Ballistic Deposition of α-Fe2O3 Thin Films for Photoelectrochemical Water Oxidation *ACS Nano*, 4, 1977, **2010**.; (b) O. Zandi, B. M. Klahr and T. W. Hamann, Highly photoactive Ti-doped α-Fe2O3 thin film electrodes: resurrection of the dead layer *Energy Environ. Sci*., 6, 634–642, **2013**.

14. Y. Lin, S. Zhou, W. S. Sheehan and D. Wang, Nanonet-Based Hematite Heteronanostructures for Efficient Solar Water Splittin, *J. Am. Chem. Soc.,* 133(8), 2398–2401, **2011**.

15. L. Xi, S. Y. Chiam, W. F. Mak, P. D. Tran, J. Barber, S. C. Joachim Loo and L. H. Wong, A novel strategy for surface treatment on hematite photoanode for efficient water oxidation. *Chem. Sci*., 4, 164–169, **2013**.

16. (a) R. H. Goncalves, B. H. R. Lima and E. R. Leite, J. Am. Chem. Soc., 133(15), 6012–6019, **2011**.; (b) R. H. Gonçalves, L. D. T. Leite and E. R. Leite, *ChemSusChem*, 5(12), 2341–2347, **2012**.; (c) A. N. Pinheiro, E. G. S. Firmiano, A. C. Rabelo, C. J. Dalmaschio and E. R. Leite, *RSC Adv*., 4, 2029, **2014**.

17. J. Vicente, D. J. Klingenberg and R. Hidalgo-Alvarez, Magnetorheological fluids: a review *Soft Matter*, 7, 3701–3710, **2011**.

18. Carbajal-Franco, G.; Avila-Garcia, A.; Tiburcio-Silver, A.; Gouvea, D.; Castro, R. H. R. *J. Nanosci. Nanotechnol.*, 10, 1338–1342, **2010**.

19. Cesar, I.; Sivula, K.; Kay, A.; Zboril, R.; Graetzel, M. Influence of Feature Size, Film Thickness and Silicon Doping on the Performance of Nanostructured Hematite Photoanodes for Solar Water Splitting, *J. Phys. Chem. C*, 113, 772–782, **2009**.

20. Leite, E. R.; Maciel, A. P.; Weber, I. T.; Lisboa-Filho, P. N.; Longo, E.; Paiva-Santos, C.O.; Andrade, A. V. C.; Paskocimas, C. A.; Maniette, Y. ; Schreiner, W. H. Development of Metal Oxide Nanoparticles with High Stability Against Particle Growth Using a Metastable Solid Solution, *Adv. Mater.* , 14, 905, **2002**.

21. Chiang, Y.-M.; Dimie III, D.; Kingery W. D. Physical Ceramics Principle for Ceramic Science and Engineering, John Wiley, New York, **1997**.

22. Barroso, M.; Mesa, C. A.; Pendlebury, S. R.; Cowan, A. J.; Hisatomi, T.; Sivula, K.; Gratzel, M.; Klug, D. R.; Durrant, J. R. Dynamics of photogenerated holes in surface modified α-Fe2O3 photoanodes for solar water splitting, *Proc. Natl. Acad. Sci.* U. S. A., 109(39), 15640–15645, **2012**.

23. Sivula, K.; Metal Oxide Photoelectrodes for Solar Fuel Production, Surface Traps, and Catalysis, *J. Phys. Chem. Lett.*, 4(10), 1624–1633, **2013**.

Chapter 4. Understanding the influence of Colloidal concentration on the thickness of hematite thin film

4.1 Introduction

The short hole diffusion length of α-Fe_2O_3 (2–4 nm) and also a low absorption coefficient of hematite thin film has been the limiting parameter to increase the photocurrent.[1] These two parameters have a direct relationship with the thickness of thin films.[2] The thicker film has higher recombination rate, due to the short diffusion length, and thinner films has lower absorbance. Thus, the thickness control has been essential to understand the mechanistic factors and to achieve the maximum photocurrent of semiconductor oxide. The CND process assisted by magnetic field has demonstrated an impressive versatility for production of homogeneous thin film with good photoresponse.[3] However, the CND process has experimental parameters that affect drastically the photoelectrochemical performance, such as colloidal concentration and sintering condition. For example, the thickness can be controlled by multistep layer deposition or by change of the colloidal concentration.[4] Previously, the layer-by-layer process was the first strategy to increase the thickness of hematite thin film.[4] However, this first approach was limited to process thin film in a small area of FTO. As described in chapter 3, the CND process assisted by magnetic field has the advantage to produce homogeneous thin film with large area, in a single step of deposition. Therefore, the thickness control was not optimized, yet. Thereby, the only way to obtain an optimized thickness by in single step is controlling the colloidal concentration during the deposition process.

In order to understand the influence of thickness on the photoelectrochemical performance, it is important to have a low roughness on the conductor substrate. The FTO substrate has a roughness of 51.4 to 73.3 nm that limits measuring accurately the thickness of hematite thin film.[5,6] Unfortunately, there is a small class of transparent conductor substrate with stability against corrosive electrolyte and heat treatment. Antimony doped tin oxide (ATO) has conductivity and chemical stability very similar to the FTO substrate.[7,8] However, the ATO substrate is not commercially available. In this context, it was deposited ATO thin film on borosilicate substrate. The Pulsed Electron Deposition (PED) is an excellent technique for growth epitaxial thin film with low roughness. Thus, the ATO was deposited on ABS by PED, as detailed in the experimental section.

4.2 Experimental Section

4.2.1 Materials

Iron (III) acetylacetonate (99.99%), oleyl alcohol, Antimony (III) oxide, Tin (IV) oxide were purchased from Aldrich Chemical Co and FTO/aluminum borosilicate was purchased from Solaronix S.A.

4.2.2 ATO Thin film by Pulsed Electron Deposition

The ATO target was used as the source of Sb and Sn to grow thin film by PED process. This target was prepared by solid-state process. The tin oxide was mixed with 12 wt% of antimony oxide, using a pestle and mortar. After this process, the powder was pressed with 2 tons, as disc format with 2 inches of diameter. The pallet was sintered at 1100 ºC under ambient atmosphere for 12 hours. The ABS substrate was cleaned with hot acetone and ultrasonic bath. The chamber pressure of PED was set up to $2.0x10^{-3}$ Torr and oxygen flux of 20 ccs. The temperature on the substrate was adjusted at 800 ºC. The electron gun was operated at 16 kV at 10 Hz with 10.000 pulses.

4.2.3 Maghemite nanocrystals and Thin film preparation

The maghemite nanocrystals were synthesized as described in chapter 3. The colloidal concentration was adjusted to 400, 300, 250, 200, 150, 100, 50 and 25 $mg.ml^{-1}$. The thermogravimetric analysis was carried out to determine the organic molecules bound on the nanocrystals. These concentrations were considered as 20-wt% of the organic compound chemically bound on nanocrystals surface. The deposition and thermal treatment were also carried out as described previously in chapter 3.

4.2.4 Photoelectrochemical characterization and UV-vis spectroscopy

The photoelectrochemical characterization was performed as cited in chapter 3. However, in this chapter both back and front side of the hematite photoanode were illumined to collect the photoresponse. UV−vis absorption spectra were obtained using a Shimadzu 3100 UV−vis spectrophotometer.

4.3 Results and discussion

Firstly, the maghemite nanocrystals were concentrated at 400 $mg.ml^{-1}$ in toluene. This stock solution was used to prepare the diluted colloidal dispersion. These nanocrystals were deposited on the FTO, ATO and ABS substrate, as described in experimental section. Figure 4.1a shows a XRD pattern of maghemite nanocrystals deposited on the aluminum borosilicate substrate and Figure 4.1b reveals the hematite XRD pattern after annealing at 850 ^{o}C, in oxygen atmosphere. The XRD peak intensity ratio between (110) and (104) was 0.7 that correspond to the isotropic hematite structure. This XRD pattern shows that the ABS substrate has no effect to texture hematite thin film. Figure 4.1c show the hematite crystallographic phase with textured peak on the direction (110). As mentioned in chapter 2, this peak is perpendicular to the (001) basal plane that has a charge transport four order of magnitude higher than others direction. In the same Figure is noted the FTO peak (200) at 38.4^{o}. It is important to highlight that the intensity of peak (110) was higher for thin film produced with 400 $mg.ml^{-1}$ and almost absent with 25 $mg.ml^{-1}$. The same behavior was observed in the thin film produced with ATO substrate. However, the textured peak for ATO substrate corresponds to the $(101)^{*}$, as can be seen in Figure 4.2. In consideration of no textured hematite powder, the peak (104) has higher intensity than peak (110).

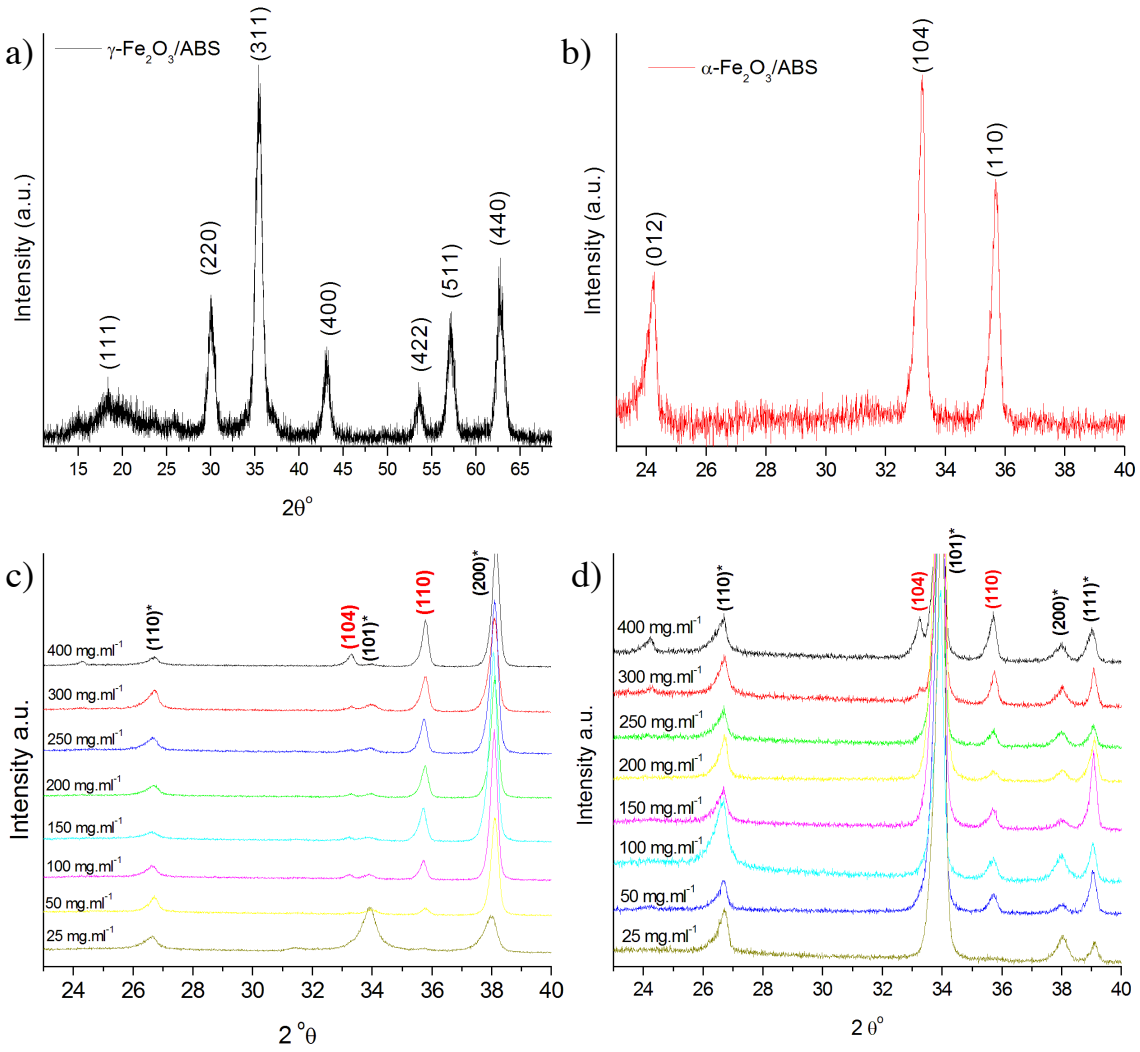

Figure 4.1. XRD patterns for hematite thin film on different substrates. a) γ-Fe_2O_3/ABS without thermal treatment b) α-Fe_2O_3/ABS, c) α-Fe_2O_3/FTO, d) α-Fe_2O_3/ATO treated at 850 ºC.

Figure 4.2 shows the peak (110)/(104) ratio in function of the colloidal concentration with typical linear rise of intensity for the deposition on FTO. In comparison with the (110)/(104) ratio for the thin film deposited on ATO, it can be noted a distinct difference between both curves. In fact, this difference shows that ATO with direction $(101)^*$ has unfavorable crystallographic plane to texture the peak (110) of hematite. In the case of FTO substrate, the textured direction is (200). However, the FTO roughness shows that the plane (200) is not exposed to the hematite contact. In chapter 2, the cross-sectional TEM images showed that (110) plane of FTO has been frequently exposed to the solid-solid contact and which it explains the high (110)/(104) ratio for the hematite deposited on FTO substrate. The textured peaks apparently disappear in thin films produced with concentration higher than 400 $mg.ml^{-1}$.

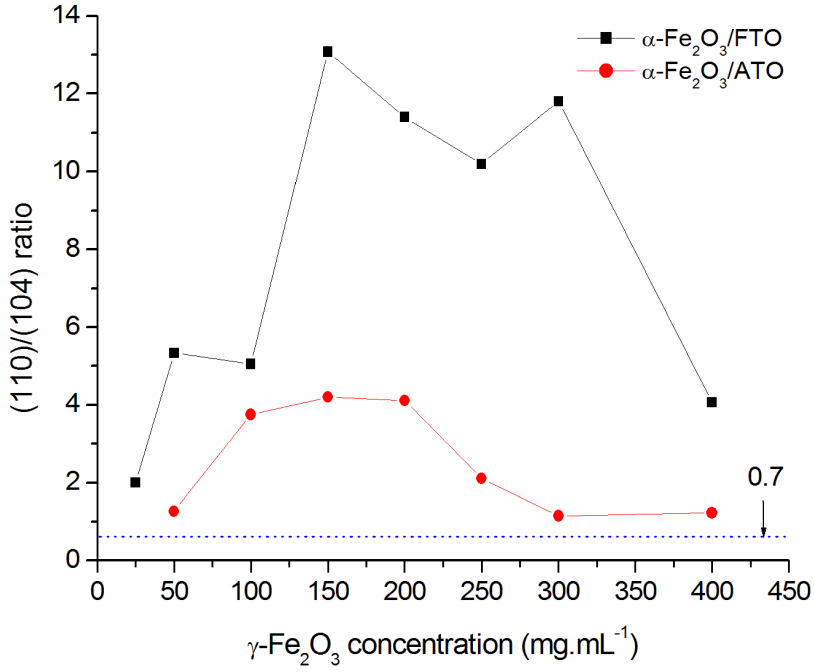

Figure 4.2. (110)/(104) intensity ratio *vs*. colloidal concentration used to produce hematite thin film. The black and red lines represent the ratio for α-Fe_2O_3/FTO and α-Fe_2O_3/ATO, respectively. The blue line is the (110)/(104) ratio for α- Fe_2O_3/ABS.

The SEM images were collected for thin films produced with different colloidal concentration deposited on the FTO substrate. Figure 4.3 shows the top view and respective cross-sectional SEM images for all thin films and revealed that the mesoporous structure has a similar behavior independent of the colloidal concentration. The average of grain size was 50 to 90 nm and porous of approximately 80 nm. The lowest thickness of 40 nm was measured for thin film produced with 25 $mg.ml^{-1}$ and the highest thickness achieved approximately 742 nm from concentration of 400 $mg.ml^{-1}$.

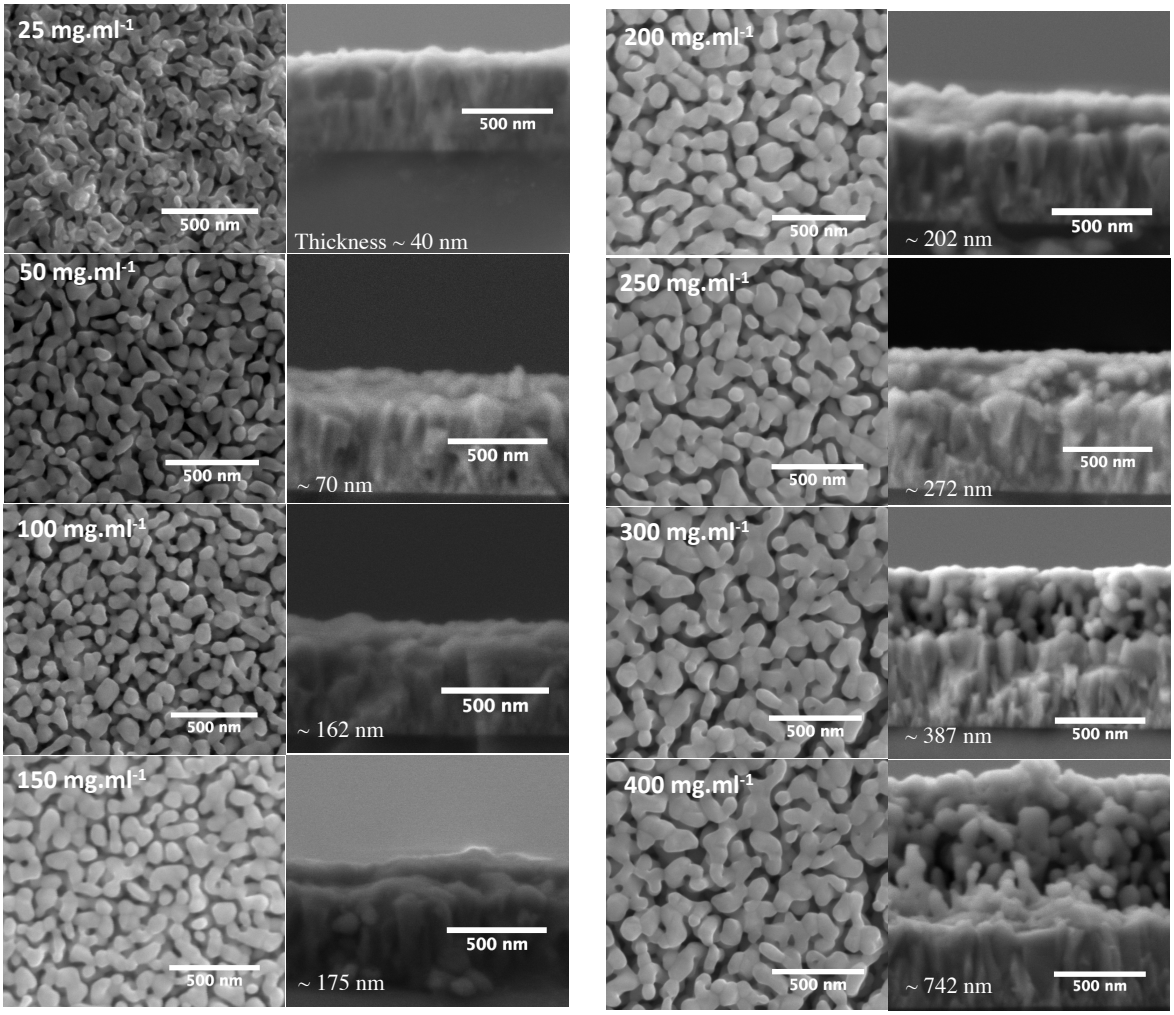

Figure 4.3. The top and cross-sectional view of SEM images for hematite thin films deposited on FTO. The sequences of SEM images correspond to the thin film deposited with colloidal concentration from 25 to 400 mg.ml^{-1}.

The SEM images also were collected for hematite thin film on ATO substrate. A similar morphology was observed in these thin films. Figure 4.6 shows the flat interface between hematite and ATO substrate. The lowest thickness of 20 nm was measured for thin film produced with 25 mg.ml^{-1} and highest thickness achieved approximately 530 nm from concentration of 400 mg.ml^{-1}. It is interesting to analyze that in the top-view SEM image the hematite thin film produced with 25 mg.ml^{-1} has no brightness spot as can be observed for hematite on FTO substrate with the same concentration. It clearly indicates that thin film has low roughness compared with hematite on FTO.

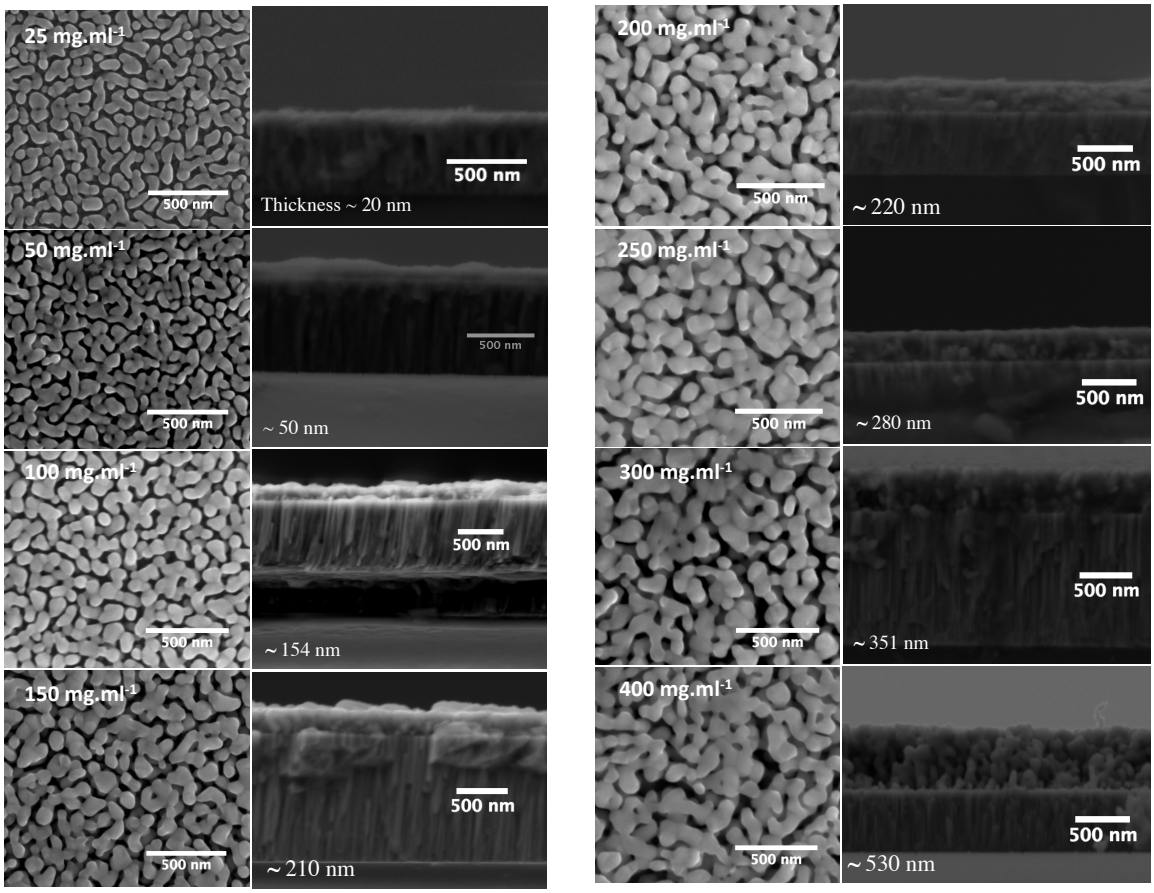

Figure 4.4. The top and cross-sectional view SEM images for hematite thin films deposited on ATO. The sequences of SEM images correspond to the thin film deposited with colloidal concentration from 25 to 400 mg.ml^{-1}.

The cross-sectional SEM images in Figures 4.3 and 4.4 were essential to measure the thickness, porosity, and the grain size and to understand the effect of colloidal concentration. Figure 4.7 shows the thickness versus the concentration with similar behavior between the FTO and ATO substrate obtained from the SEM images. It is important to mention that the thickness of hematite thin film on FTO was measured considering the roughness of the FTO substrate.

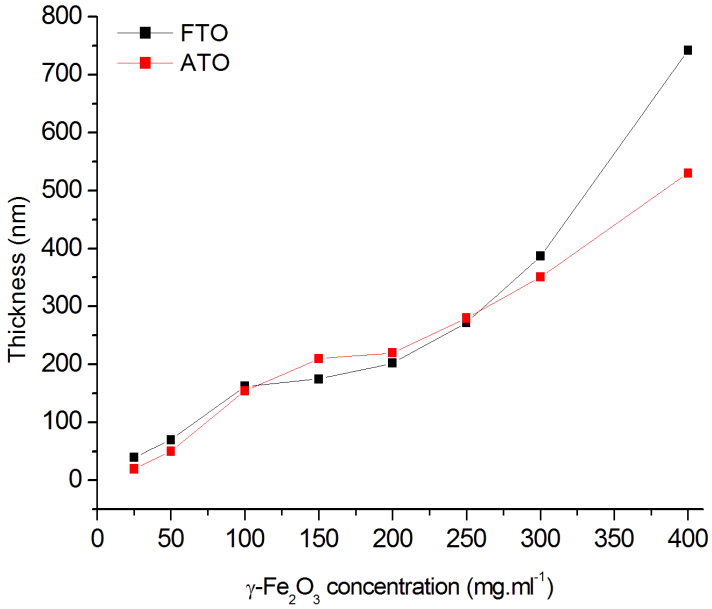

Figure 4.5 Thickness of hematite thin film *vs*. nanocrystals concentration as precursor.

The photoelectrochemical measurement also was performed for all hematite thin films. It is possible to observe that the thickness of hematite thin film has slight effect in the overpotential shift. As expected, the photocurrent density is directly affected with the change of thickness. Figure 4.6 shows the J *vs* V_{RHE} curves collected for hematite photoanodes with different maghemite concentrations. The backside-illuminated photoanode has lower photocurrent density than the front-side illumination. The explanation for this difference is based on the exponential decreasing of light intensity in function of the penetration path, according with Lambert-Beer law. In the backside illumination the interface FTO/hematite receives an intense radiation that is decreases until the electrolyte/hematite surface. On the contrary, the front-side illumination electrolyte/hematite interface receives the intense radiation. The decreasing of recombination rate on the liquid/solid surface is favored by the hole acceleration on the depletion layer.

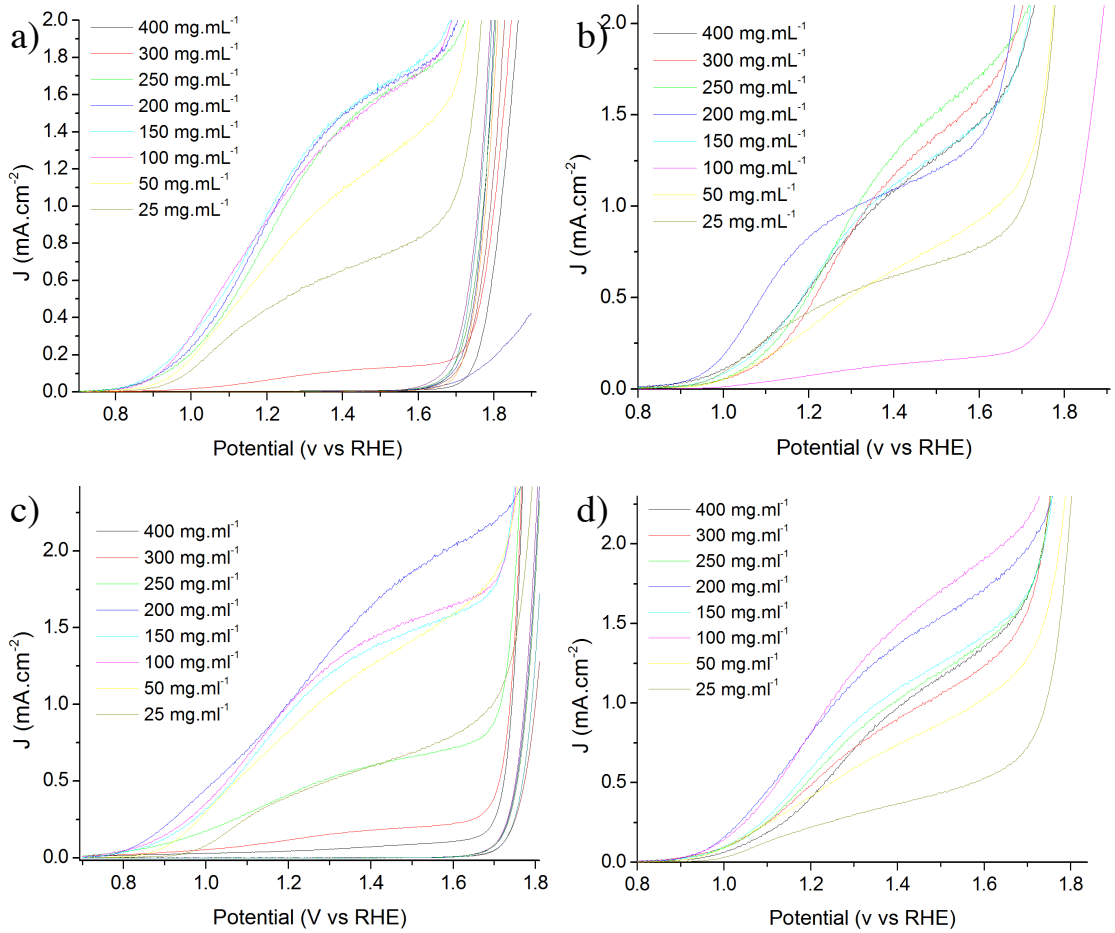

Figure 4.6. Photocurrent density *vs*. V_{RHE} collected for hematite thin films. a) frontside and b) backside illumination for α-Fe_2O_3/FTO, c) frontside and d) backside illumination for α-Fe_2O_3/ATO.

To become clear this discussion, the photocurrent density was plotted against colloidal concentration and the thickness measured by cross-sectional SEM images for thin film on ATO and FTO. Figure 4.9a and b shows the J *vs*. concentration and J *vs*. thickness, respectively for hematite thin film on FTO. The photocurrent density collected from the illuminated frontside of the photoanode is represented by the black line curve

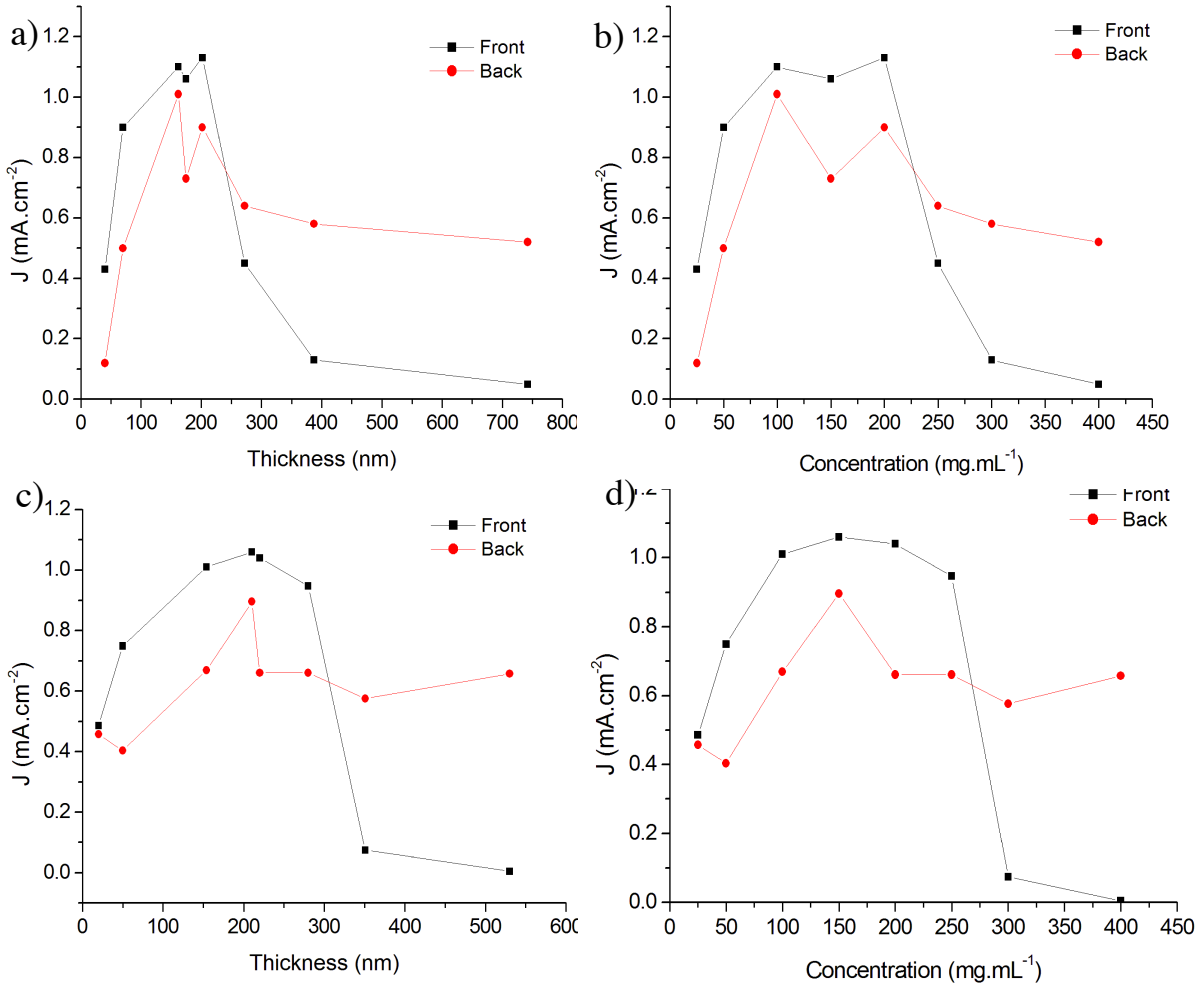

Figure 4.7. Photocurrent density for hematite thin films. a) J at 1.23 V_{RHE} *vs*. nanocrystals concentration, b) J at 1.23 V_{RHE} *vs*. thickness for front and backside illumination of α-Fe_2O_3/FTO, c) and d) for α- Fe_2O_3/ATO.

The Uv-vis spectra were collected for hematite thin film on FTO and ATO substrates. In both substrates, the saturation of Uv-vis light absorption was observed in the thin film produced with 400 $mg.ml^{-1}$ or more precisely thin films with thickness higher than 400 nm. The absorption spectra range from 300 to 600 nm was observed in all thin films produced, according with the narrow band gap (1.9 - 2.2 eV).

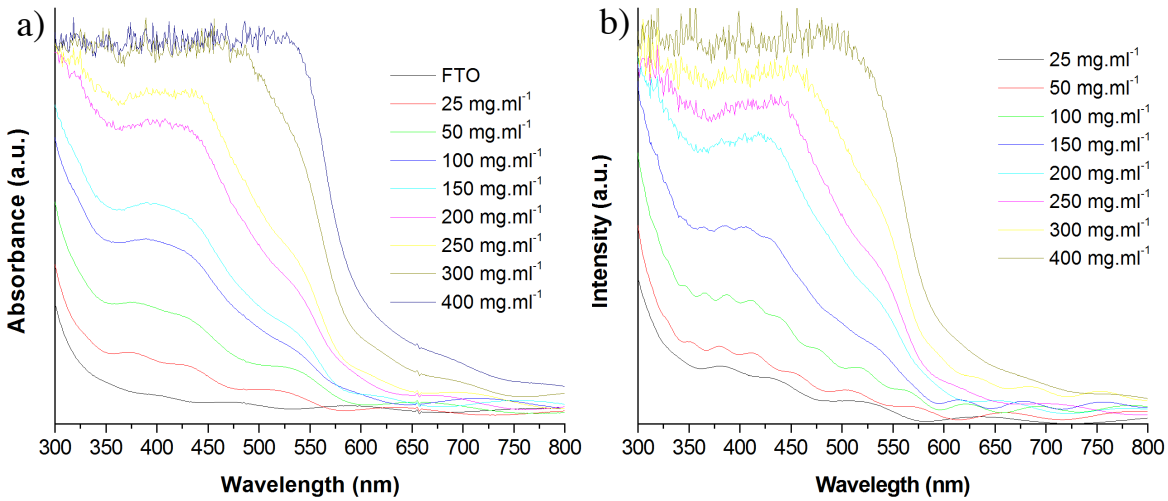

Figire 4.8. Uv-vis spectra of hematite thin films deposited on a) FTO and b) ATO substrates with nanocrystals concentration from 25 to 400 $mg.ml^{-1}$.

As mentioned in chapter 1, the maximum theoretical efficiency can be measured in function of the band gap and the amount of photons absorbed. The charge separation rate depends on the absorbance that is correlated with the thickness and the absorption coefficient.

Uv-vis spectra in Figure 4.8 represents the amount of photons absorbed and it can be used to calculate the theoretical efficiency, considering only the contribution referent in J_{ab}. The equation 1.12, in chapter 1 was used to calculate this efficiency. Therefore, to consider only the absorbed fraction, it was included the term $\eta = 1 - 10^{-\varepsilon.l}$, where ε is the absorption coefficient of hematite and l is the thickness of thin film.

The integration was performed in function of the solar irradiance AM 1.5 and the UV-vis spectra. Figure 4.9 shows this theoretical current density versus the concentration of maghemite. The theoretical current density for hematite thin films produced with 400 $mg.ml^{-1}$ was 10 $mA.cm^{-2}$ and 14 $mA.cm^{-2}$ for FTO and ATO substrates, respectively. Therefore, the experimental value was 0.6 $mA.cm^{-2}$ at 1.23 V_{RHE}.

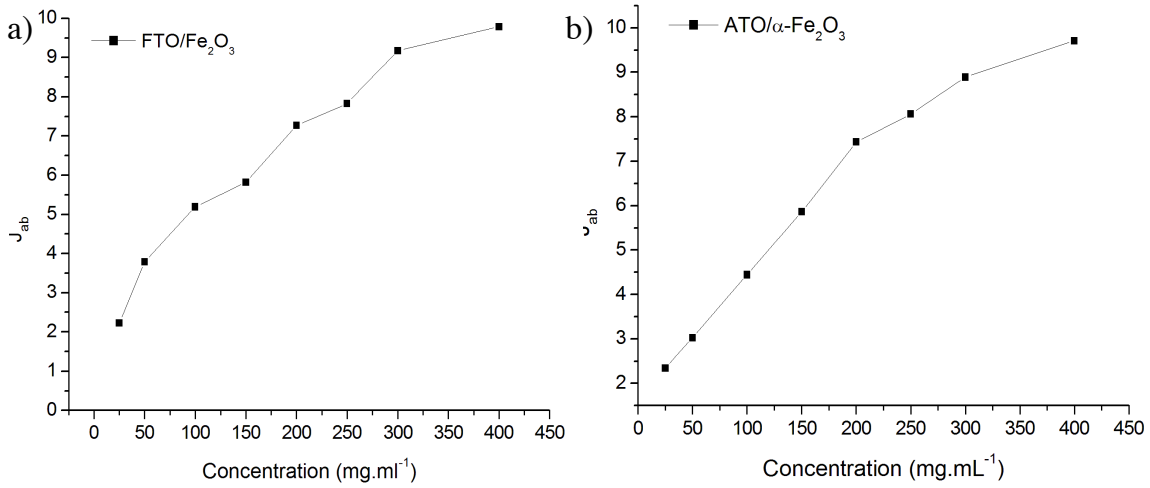

Figure 4.9. J_{ab} estimated through Uv-vis spectra and solar irradiance spectrum. a) α-Fe_2O_3/FTO and b) α- Fe_2O_3/ATO

Figure 4.10 shows a photograph of hematite thin film deposited on FTO and ATO substrate in function of colloidal concentration. The thin film produced with 400 $mg.ml^{-1}$ is noted a strong red color in both substrate.

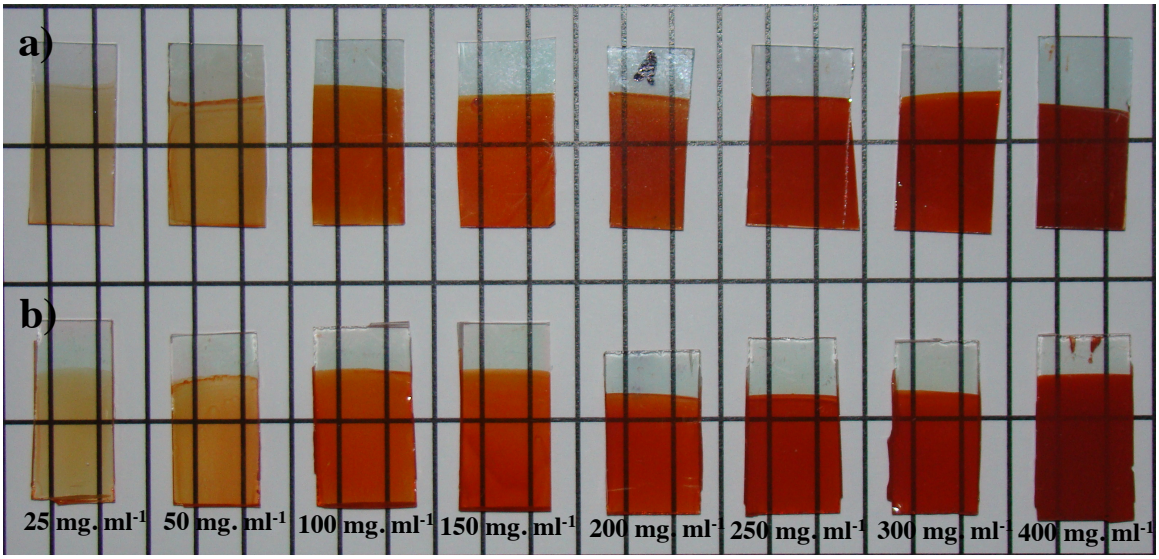

Figure 4.10. Photograph of hematite thin film deposited on a) ATO and b) FTO.

In order to obtain more information about the photoresponse behavior in function of atmospheric condiction used during the thermal treatment, the undoped hematite thin film deposited on the FTO was treated at 850 ºC in air, oxygen and nitrogen gas flux, for 20 minutes. Figure 4.11 is evident that thin film treated in oxygen gas had onset of 0.8 V_{RHE} and photocurrent of 1.4 $mA.cm^{-2}$, the thin film treated in air had a photocurrent of 1.1 $mA.cm^{-2}$ with a onset of 0.85 V_{RHE}. However, the thin film treated in nitrogen flux had a

worse perfomonce that can be explained by Fe^{2+} formed in inert atmosphere. The Fe^{2+} can trap the charge photogenarated that results in low photocorrent.

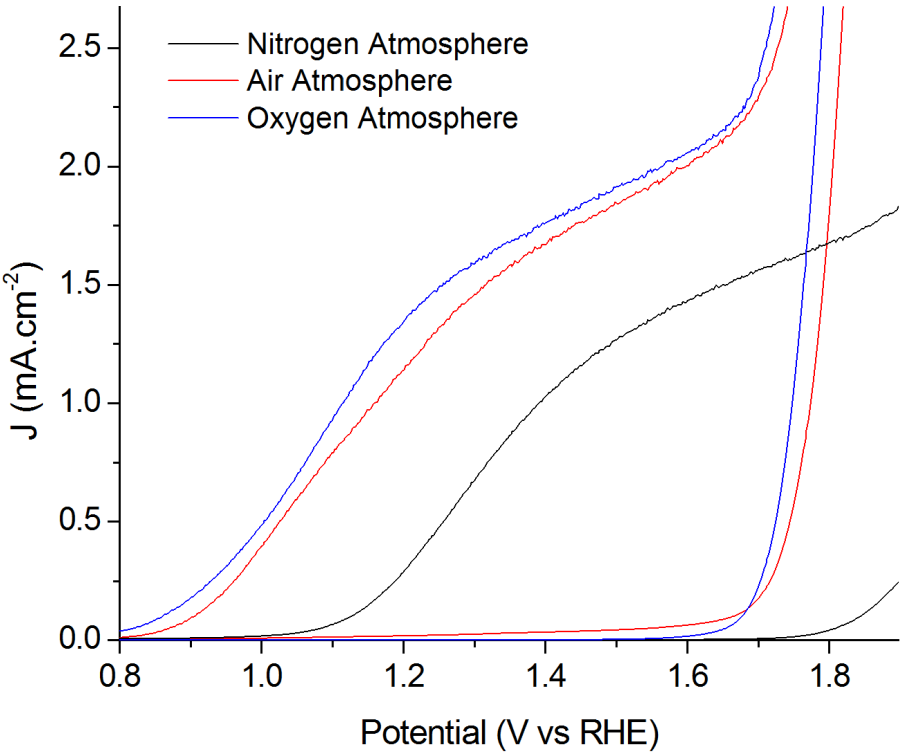

Figure 4.11. Effect of atmospheric condition on hematite photoanode.

4.4 Conclusions

In conclusion, the optimization of colloidal deposition process for undoped hematite showed significant effect of nanocrystals concentration on the thickness and photoelectrochemical performance. The XRD pattern reveled that the conductor substrate, such as FTO and ATO, has strong influence to texture hematite grain. The ATO substrate also showed less favorable on the orientation of peak (110) when compared with FTO substrate. The degree of texture had a direct effect on the photoresponse. The UV-vis spectra and the estimative of maximum photocurrent also gave an important contribution to understand absorbance of thin film produced on FTO and ATO substrate. It has showed that these photoanodes have great perspective to achieve the maximum theoretical efficiency of 14% considering only absorbance of thin film produced with a colloidal concentration of 400 $mg.ml^{-1}$.

4.5 References

1. Kennedy, J. H.; Frese, K. W. Photooxidation of water at alpha-Fe_2O_3 electrodes. *J. Electrochem. Soc.*, *124*, C130, **1977**

2. Bosman, A.; Vandaal, H. Small-polaron versus band conduction in some transition-metal oxides. *Adv Phys*, *19*, 1, **1970**

3. Formal, F. Le; Gratzel, M.; Sivula, K. Controlling Photoactivity in Ultrathin Hematite Films for Solar Water-Splitting. *Adv. Funct. Mater.*, *20*, 1099, **2010.**

4. Klahr, B. M.; Martinson, A. B. F;Hamann, T. W. Photoelectrochemical Investigation of Ultrathin Film Iron Oxide Solar Cells Prepared by Atomic Layer Deposition. *Langmuir*, *27*, 461, **2011.**

5. Rioult, M.; Magnan, H.; Stanescu, D.; Barbier, A. Single Crystalline Hematite Films for Solar Water Splitting: Ti-Doping andThickness Effects *J. Phys. Chem. C*, *118*, 3007, **2014.**

6. Gonçalves, R. H.; Leite. E. R. The colloidal nanocrystal deposition process: an advanced method to prepare high performance hematite photoanodes for water splitting. *Energy & Enveromental science*, 7, 2250-2254, **2014.**

Chapter 5. In-situ Electron microscopy to understand Iron Oxide growth in Nanoscale

5.1 Introduction

Semiconductor oxides have been considered the key material to be applied in photoelectrochemistry. Hematite has been a semiconductor oxide that plays an important rule as photoanode for water oxidation.[1] Therefore, there are many fundamental parameters that need to be overcome to achieve the maximum performance of this semiconductor. It is well known that single crystal of hematite has low efficiency due to the short hole diffusion length and there is not an element doping to change this configuration.[2] On the other hand, polycristaline hematite photoanode has a significant performance when compared with single hematite.[3] Apparently, the increase of grain boundary has a positive effect on the electronic conductivity of hematite.[4] For long time, electroceramic field has been dedicated to understand the electrical behavior of this transition metal oxide in function of sintering, densification and doping. Grain boundary and diffusion transport have been the heart of ceramic processing.[5]

Understanding of mechanism of grain growth in nanoscale has been a huge challenge due to the fast kinetic and abnormal grain growth.[6] In the conventional sintering process, the empirical Hall-Petch equation can predict the yield stress in function of grain size, ($\sigma = \sigma_0 + f.d^{-1/2}$) where σ is the yield stress, σ_0 is the lattice friction stress required to move individual dislocations, f is a constant of material and d is the grain size.[7-9] However, in nanocrystals the constant f has a negative value and the yield stress decreases drastically with the decreasing of the nanocrystals size and this phenomenon is know as inverse Hall-Petch effect.[10,11] For example, a nanocrystal with 10 nm of diameter has 20% of atom located on the grain boundaries and a high-energy surface. In these conditions, the atom dislocation becomes favorable on the surface.[12] Thus, in high temperature the yield stress can decrease considerably and generate a condition of superplastic flow in crystalline structure where the particle has very large tensile deformations.[13.14] This empirical model has been studied for long time, specially applied in metallic structure.[15] However, there is no experimental visualization that this superplastic flow phenomenon can happen in transition metal oxide.

It has been extremely hard to measure the dynamics of diffusion-induced grain-boundary migration in nanocrystalline system due to the complexity to observe

nanocrystals under heating influence.[16] However, the *in situ* hot stage TEM has been a powerful tool to understand this effect in nanoscale. This chapter describes an *in situ* hot stage TEM experiment of maghimite nanocrystals to mimic grain growth kinetic of this nanocrystals during the sintering state of hematite thin film. The main strategy is to understand how the Sn doping controls the hematite grain size on the thin film and compare with undoped process.

5.2 Experimental Section

5.2.1 Material

Maghemite nanocrystals was produced as described in chapter 3. Silicon nitride membrane grid with 5 nm thickness and square membrane windows centered on 200μm thickness silicon frames from Norcada Inc. The *in situ* hot stage holder from Gatan and Tecnai F20 from FEI Company.

5.2.2 *In situ Hot Stage sample holder and sample preparation*

The *in situ* heating experiments were performed in a Gatan 628 single-tilt heating holder (with an tantalum based furnace). The first step of this experiment was to deposit the nanocrystals on the grid. The nanocrystals dispersion was diluted and added tin butoxide. The nanocrystals dispersion was dropped on the grid and dried. After that, the next step was to eliminate the organic compound on the nanocrystals surface. For it, the grid was treated at 400 ºC in an infrared furnace for 30 seconds. In the *in situ* heating experiment, the sample was slowly heated until 400 ^{0}C and after that video was recorded during the heating until 550 ºC, 650 ºC and 750 ºC. The transmission electron microscopy was a Tecnai F20 at 200 kV .

5.3 Results and Discussion

Figure 5.1a shows a photograph of a single tilt sample holder used to performance the *in situ* heating experiments. The sample holder has a tantalum furnace that achieves high temperature in vacuum. However, *in situ* heating experiments has some disadvantages, such as the thermal drift. To minimize this effect, the heating rate was

raised slowly. Figure 5.1b shows a photograph of silicon nitride grid where the nanocrystals were deposited.

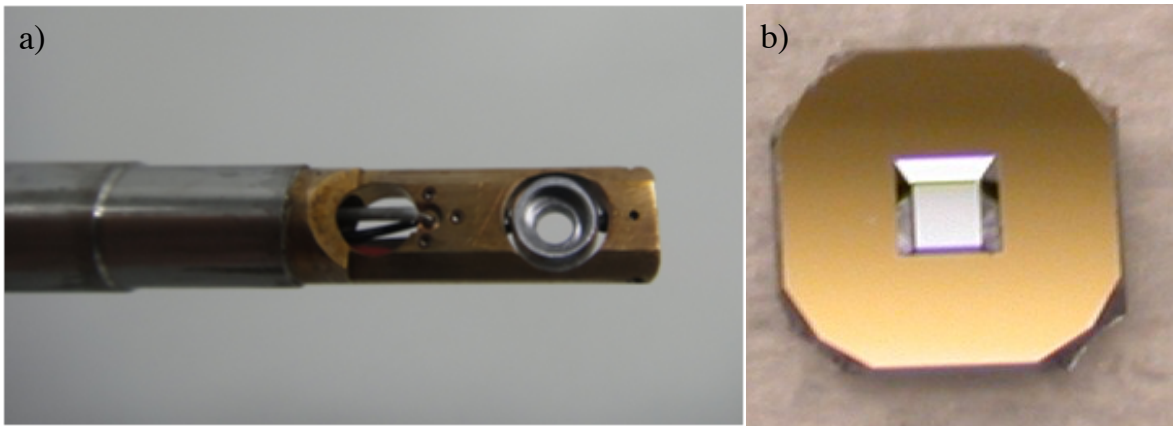

Figure 5.1. Details of TEM holder. a) Gatan 628 Single Tilt Heating Holder b) Silicon nitride grid.

In the first *in situ* heating experiments, the maghemite nanocrystals was observed in low magnification. Figure 5.2a provide a TEM image of this nanocrystals with a size control and reasonable dispersion on the Si3N4 grid. Figure 5.2b shows a TEM image for iron oxide after the heating treatment at 750 ºC. It is evident that a monodisperse system transform into polydisperse structures with large grain size. The HRTEM image in Figure 5.2c shows the nanocrystals in oriented zone axis and Figure 5.3c shows the HRTEM image of grain boundary of two nanocrystals after sintering process. The insets below of Figure 5.2 show the electron diffraction before and after *in situ* heating experiments. In video recorded of this process permit observe that there is superplastic behavior in this process. In other words, superplastic flow phenomenon determines the grain kinetic growth of γ-Fe_2O_3 nanocrystals. It is important to mention that the growth process is trigged at 500 ºC.

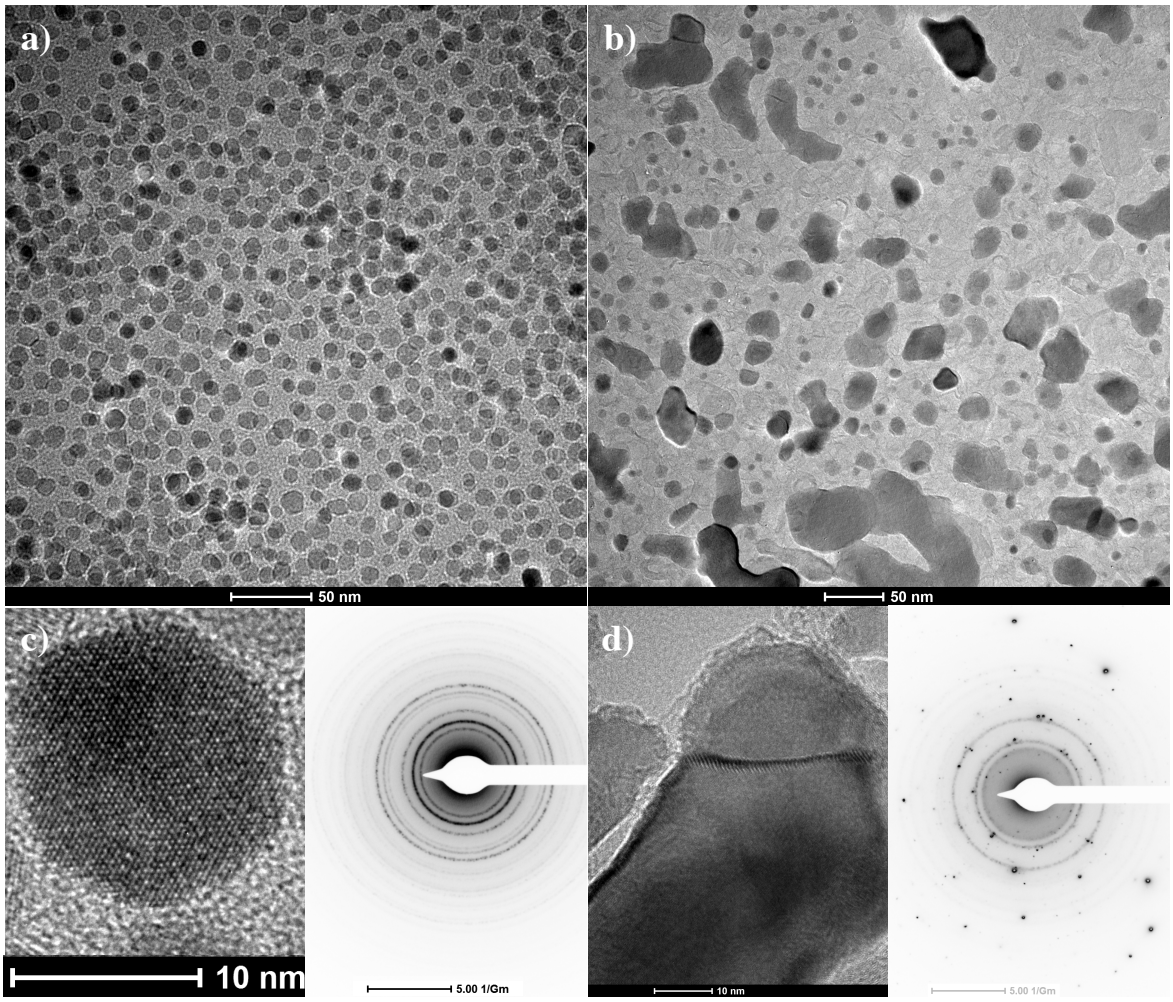

Figure 5.2 General views of *in situ* TEM images. a) Pure γ-Fe_2O_3 deposited on Si_3N_4 before and b) after heating experiment c) HRTEM image of γ-Fe_2O_3 before and d) after heating experiment.

To mimic the CND process, the tin butoxide was added on the colloidal dispersion, using the same concentration. Again, the TEM images were collect before, as can be seen in Figure 5.3a. After the *in situ* heating experiment, the TEM images in Figure 5.3b reveals that nanocrystals have evolved for large spherical particles and a portion of nanocrystals of 10 nm remained constant. HRTEM image in Figure 5.3c and d shows that nanocrystals size were affected drastically when compared with undoped heating experiments.

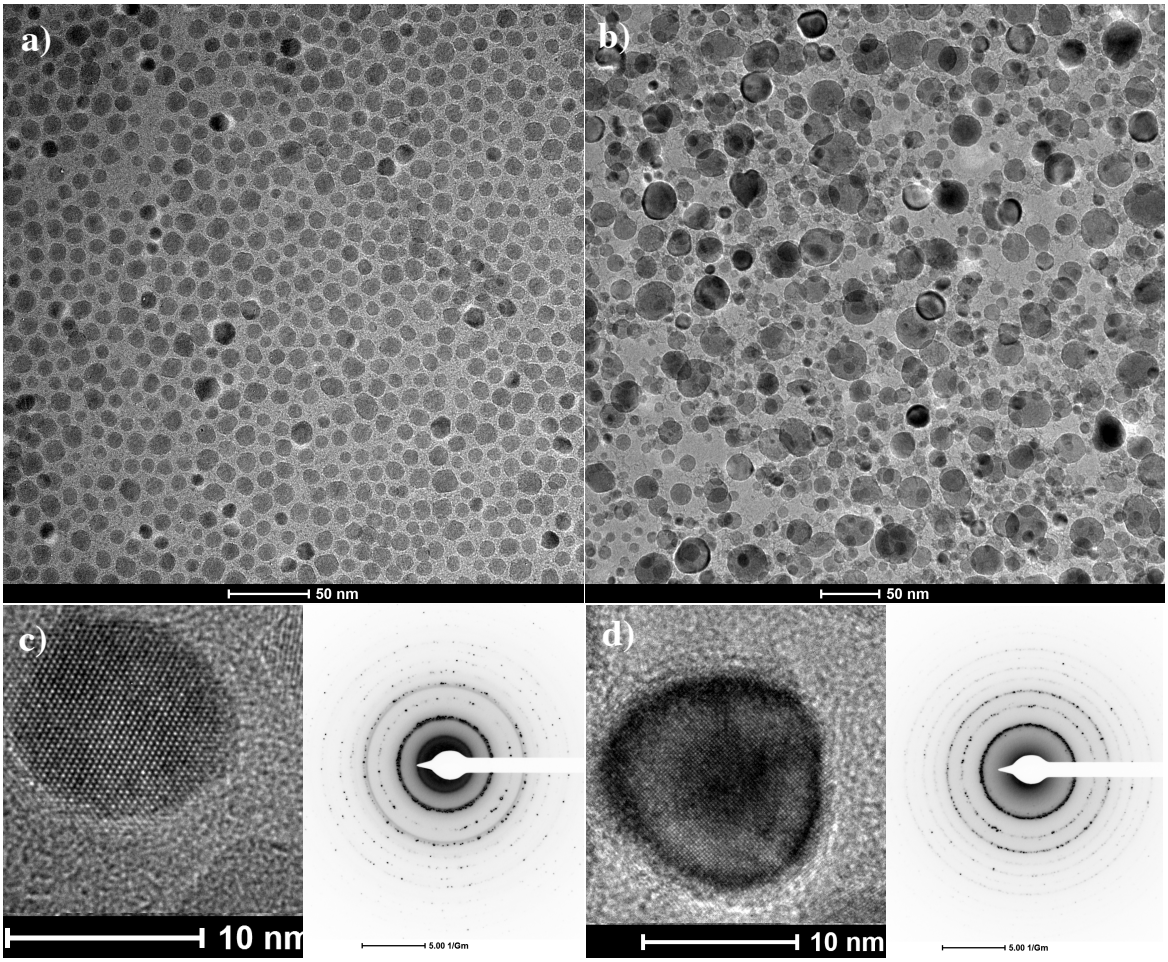

Figure 5.3 General views of *in situ* TEM images. a) Sn doped γ-Fe_2O_3 deposited on Si_3N_4 before and b) after heating experiment c) HRTEM image of Sn doped γ-Fe_2O_3 before and d) after heating experiment.

The EDS analysis, after *in situ* experiment, in Figure 5.4 shows that atom percentage for Fe was 96.67% and for Sn 3.33%. This percentage had the same value before the sintering process. The EDS analysis showed also a silicon peak from grid and also a tantalum peak from the furnace.

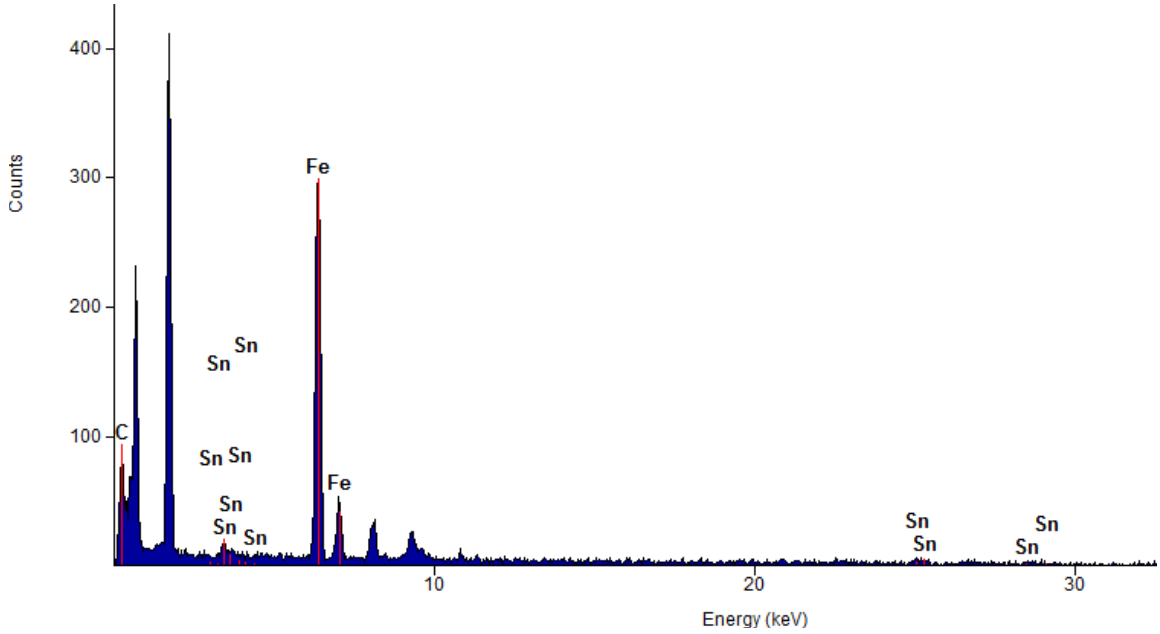

Figure 5.4 EDS analysis after in situ experiment for Sn doped γ-Fe_2O_3.

The size distribution was also measured by counting 600 particles. Figure 5.4a reveals the mean diameter of 12 nm, before the heating process. After the experiment for Sn doped γ-Fe_2O_3, the size distribution was affected as shown in Figure 5.4b and crystalline particles were observed from 8 to 40 nm. Figure 5.4c shows the size distribution for undoped γ-Fe_2O_3 with a range of 8 to 100 nm. Furthermore, the population of nanocrystals with 12 nm of diameter considerably decreased. It is indication that Sn added on the nanocrystals dispersion tends to segregate on the surface of nanocrystals to reduce the grain boundary free energy to zero and stabilize the grain sizes.

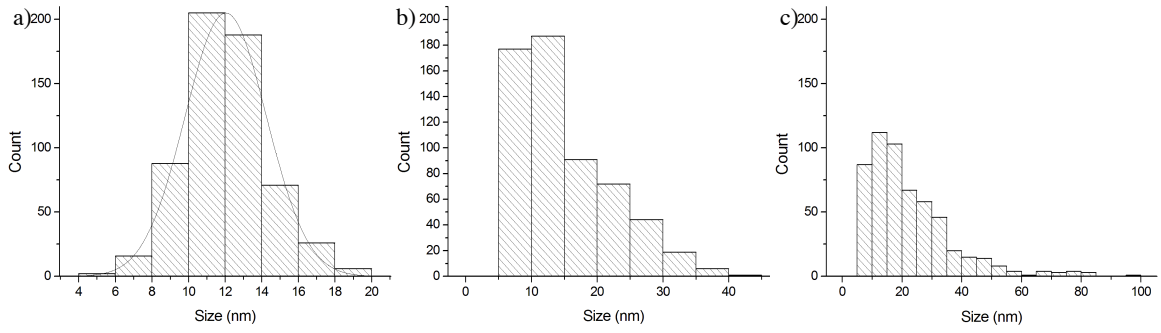

Figure 5.5 Size distributions of particles. a) γ-Fe_2O_3 before b) Sn doped γ-Fe_2O_3 after c) γ-Fe_2O_3 undoped after the heating experiments.

The sequence of TEM images in Figure 5.6 shows a detailed growth process. The arrow in the first image shows nanocrystals at an initial stage where is possible to observe the grain boundary of these nanocrystals. The last stage, the arrow highlight a particle formed with 20 nm of diameter, during *in situ* heating experiments. An important

phenomena observed in this experiments was the nanoparticles motion on the Si_3N_4. The high rate of atom dislocation on the grain boundary gives a superplastic behavior for this nanoparticles during the heating stage. It can be correlated with the inverse Hall-Petch effect where the yield stress is reduced in nanoscale. However, the nanoparticle achieves sizes around 100 nm and the growth is motionless, it means when particle size is large atom diffusion rate decrease due to reduction of surface energy. The grain boundary on the solid-solid interface creates a barrier for atom dislocation propagation.

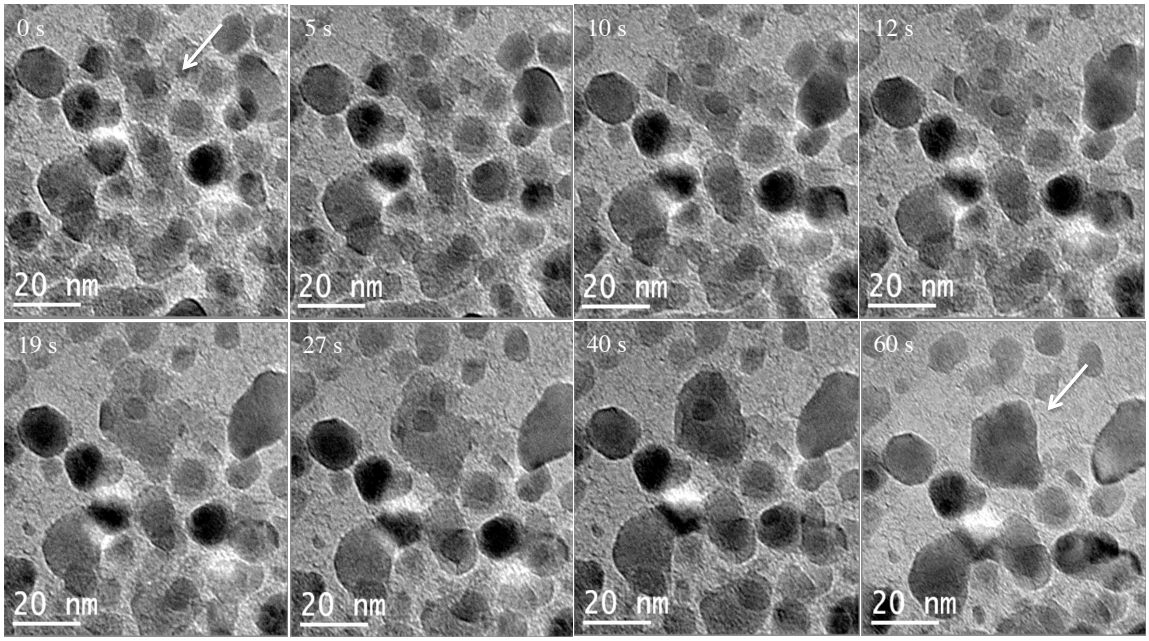

Figure 5.6 Sequence of TEM images for undoped γ-Fe_2O_3 treated at 650 ºC.

The *in situ* heating experiments for Sn doped γ-Fe_2O_3 are detailed in sequence of TEM images in Figure 5.7. It is possible to see a slow growth rate when compared with undoped system. Apparently, the Sn^{4+} added on the nanocrystals surface reduces the grain boundary sliding and consequently decreases the growth rate. Sintering SnO_2 has not been a simple task, it is well know that this oxide has low diffusion rate and can be decomposed under high temperature. This low diffusion rate is the key to control the iron oxide growth.

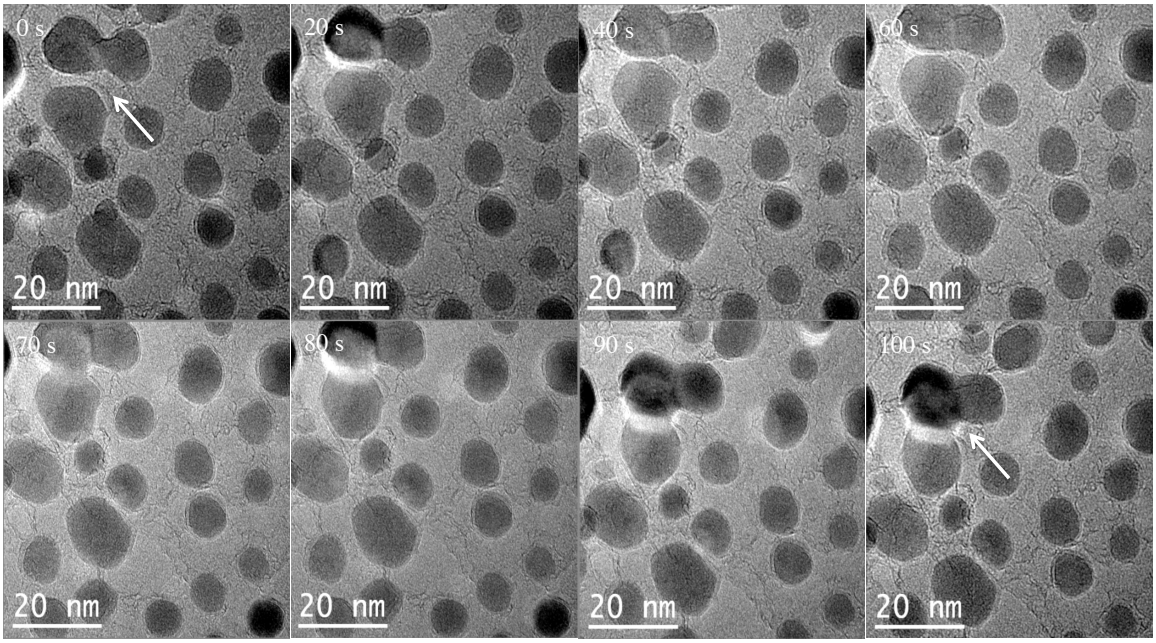

Figure 5.7 Sequence of TEM images for Sn doped γ-Fe_2O_3 treated at 750 ºC.

5.4 Conclusions

In situ heating TEM images have demonstrated that a superplastic phenomenon has controlled the nanocrystals growth for undoped γ-Fe_2O_3. The critical temperature for this phenomenon was around 550 ºC. The abnormal growth process was observed at 750 ºC where the superplastic effect was more accentuated. The size distribution of nanoparticles for undoepd has a lognormal behavior, after the heating process. The Sn added on the system creates a barrier for growth process due to the low diffusion rate. *In situ* heating experiments showed that Sn atom on the γ-Fe_2O_3 has limited growth and particle achieve only 40 nm of diameter.

5.5 References

1. Sivula, K.; Formal, F. Le; Gratzel, M. Solar Water Splitting: Progress Using Hematite (a-Fe_2O_3) Photoelectrodes. *ChemSusChem*, 4, 432 – 449, **2011.**

2. Turner, J.E., Hendewerk, M., Parmeter, J., Neiman, D., Somorjai, G.A.: The characterization of doped iron-oxide electrodes for the photodissociation of water – stability, optical, and electronic-properties. *J. Electrochem. Soc*. 131, 1777, **1982**.

3. Launay, J.C., Horowitz, G.: Crystal-growth and photo-electrochemical study of Zr-doped alpha-Fe_2O_3 single-crystal. *J. Cryst. Growth*, 57, 118, **1982**.

4. Greutert, F.; Blatter, G. Electrical properties of grain boundaries in polycrystalline compound semiconductors. *Semicond. Sci. Technol.* 5, 111-137, **1990**.

5. Brener, E.A; Temkin, D.E. Theory of diffusion induced grain boundary migration: is mass transport along free surfaces important?. *Acta Materialia, 50,7, 1707–1716,* **2002**.

6. Lawrencea, A.; Rickmana, J.M.; Harmera, M.P.; Rollettb, A.D. Parsing abnormal grain growth. *Acta Materialia*, 681–687, **2016**.

7. Armstrong, R. W. 60 Years of Hall-Petch: Past to Present Nano-Scale Connections. *Materials Transactions*, 55, 1, 2- 12, **2014**.

8. Fan, G.J.; Choo, H.; Liaw, P.K.; Lavernia, E.J. A model for the inverse Hall–Petch relation of nanocrystalline materials. *Materials Science and Engineering A,* 409, 243–248, **2005**.

9. Chokshi, A.H.; Rosent, A.; Karch, J.; Gleiter, H. On the Validity of Hall-Petch relationship in Nanocrystalline Materials. *Scripta Metallurgica*. 23, 1679-1684, **1989**.

10. Takeuchi, S. The mechanism of the inverse Hall-Petch relation of nanocrystals. S*cripta Materialia,* 44, 1483-1487, **2001**.

11. E. O. Hall: Proc. Phys. Soc. Lond. B 64, 47-753, **1951**; N. J. Petch: *J. Iron Steel Inst*. 174, 25-28, **1953**.

12. Schiotz, J., Di Tolla, F. D. & Jacobsen, K. W. Softening of nanocrystalline metals at very small grain sizes. *Nature,* 391, 561–563, **1938**.

13. Schneibel, J.H.; Heilmaier, M. Hall-Petch Breakdown at Elevated Temperatures, *Materials Transactions*. 55, 1, 44 -51, **2014**.

14. Ashby, M. F.; Verrall, R. A. Diffusion-Accommodated Flow and Superplasticity. *Acta. Metall*., 21, 2, 149–63, **1973**.

15. Sherby, O. D. ; Wadsworth, J. Superplasticity—Recent advances and future directions. *Progress in Materials Science*, 33, 3, **1989**.

16. Swygenhove, H. V. Grain Boundaries and Dislocations**.** *Science***,** 5, 296**, 2002.**

Chapter 6. Electrodeposition of Metal Hexacyanoferrates as Efficient Catalysts for the Oxygen Evolution Reaction

"This chapter shows a collaborative research made at The Pennsylvania State University"

6.1. Introduction

Oxygen evolution reaction (OER) for long time has been considered the critical parameter of water electrolysis.[1-4] It is already known that the anode is presence of corrosive electrolyte has self-oxidation trends due to the anodic potential applied to splitting water. Unfortunately, there is a lack of electrocatalyst that presents minimum requisite for OER. In general, RuO_2 and IrO_2 are the most efficient electrocatalysts for OER due to the metallic conductivity, high catalytic activity, and resistance against the corrosive electrolyte.[5-8] Indeed, catalytic support also is another variable that affects directly the overpotential. Frequently, these supports are alloys or pure metal with high surface area that can suffer corrosion under electrochemical conditions.[9] For OER, alkaline electrolytes have been consolidated as excellent media for this purpose.[10-14] Therefore, the support catalytic must be resistant to the electrolyte and avoid the isolating oxide growth on the interface.

The eminent perspective for large-scale production of hydrogen gas via conventional electrolysis demands more researches to investigate new electrocatalysts with low cost, durability and especially with low overpotential for the hydrogen evolution reaction (HER) and OER. Corrigan discovered that iron impurities in a nickel electrode had significant influence on the OER overpotential. His work opened new perspectives to develop catalysts based on Ni/Fe compounds. Nickel iron (oxy)hydroxide catalysts ($Ni_{1-x}Fe_xOOH$) have received more attention due to the excellent electron transfer and bond strength of M-O.[15,16] The main hypothesis for the iron contamination on the nickel electrode has been the increase of conductivity. Despite the outstanding electrochemical performance, there are few routes to deposit this electrocatalyst. The most common route is the electrodeposition of iron-nickel from a solution under cathodic potential and high current.[17] The hydrothermal growth of (oxy)hydroxide has also led to good performance.[18,19]

This chapter describes an approach to produce a ($Ni_{1-x}Fe_xOOH$) thin film via electrodepositing process on a sustainable conductor support to produce a dimensionally stable anode, such as Pyrolytic Graphite Sheet (PGS). For this purpose, a Prussian Blue

(PB) analogue, such as $Ni_{1-x}Fe_xHCF$ (hexacyanoferrate) was used as a precursor to produce the electrocatalyst. This approach has the advantage to use low potential and current values during the deposition. The precipitation mechanism of PB is based on the reduction of ferricyanide $[Fe^{III}(CN)_6]^{3-}$ to ferrocyanide $[Fe^{II}(CN)_6]^{4-}$ in a solution of Fe^{3+} that produce a insoluble compound on the substrate.[20] This reduction can be made via electrochemical or electroless process. The PB analogues use Ni^{2+}/Fe^{3+} as cations, instead of uniquely Fe^{3+}. This metal hexacyanoferrate is converted into $Ni_{1-x}Fe_xOOH$ when in contact with the alkaline solution.

6.2 Experimental Section

6.2.1 Material

The FTO quartz substrate was purchased from Solaronix S.A. The pyrolytic graphite sheet (PGS) was purchased from Panasonic. Palladium foil, iron (III) nitrate 99.9%, and potassium ferricyanide were purchased from Aldrich. PGS was purchased from Panasonic Company.

6.2.2 Electrochemical thin film deposition of metal ferricyanide

In this process, a 50 ml three-neck round-bottom flask was used as an electrodeposition cell. First, distinct stock solutions of Ni (II), Fe (III) and $[Fe^{III}(CN)_6]^{3-}$ (0.1 M) were prepared. 20 mL of KCl (1 M) and 1 mL of $K_3[Fe(CN)_6]$ was added in the round-bottom flask under stirring. After that, 0.5 mL of Ni(II) and 0.5 mL of Fe (III) were also added to the cell. The FTO substrate was positioned in the middle of cell and platinum mesh as counter electrode and the reference saturated $Ag/AgCl_s$ were positioned in the lateral. Chronoamperometry measurements were performed at 0.1 V *vs*. Ag/AgCl during 50, 100 and 150s. After the deposition of metal hexacyanoferrates (HCF), the substrate was slightly rinsed with deionized water (18.2 MΩ·cm). The optimized conditions were used to deposit the catalyst on a palladium foil and PGS.

6.2.3 Electrochemical Measurement

Before starting the OER measurement, the electrochemical cell with three electrode modes was cleaned with Aqua Regia (3:1 $HCl:HNO_3$) and rinsed with deionized water

(18.2 MΩ·cm). 1 M of KOH was used as electrolyte was prepared. The thin film of $Ni_{1-x}Fe_x[Fe(CN)_6]_y$ deposited on the substrate was used as the working electrode (WE). A platinum gauze (0.1mm diameter, 2 cm^2 of geometric area) was used as a counter-electrode. A Haber-Luggin capillary $Ag/AgCl_{st}$ was used as a reference electrode. The distance from the reference tip to the WE was 3 mm. Before collect a slow linear sweep voltammetry (LSV), the WE was cycled 10 times at 25 $mV.s^{-1}$ in a range from 0.8 to 1.8 V *vs*. RHE. After that, the LSV was registered at 5 $mV.s^{-1}$. The chronopotentiometric experiment was carried out at 10 $mA.cm^{-2}$ in a 1 cm^2 geometric area. Magnetic stirring was used to enhance bubble elimination from the WE.

6.2.4 Thin film characterization

Micro-Raman spectrum was obtained in a Synapse Horiba Jobin Yvon with a Nd:YAG (wavelenght of 532 nm). A FEI field- emission SEM NanoSEM 630 was used to register images and a EDS to detect the electrocatalyst on the substrate.

6.3 Results and Discussion

The first step of this strategy was to optimize the deposition of the metal hexaferricyanide on the FTO substrate. As shown in to the table 1, four experimental conditions were selected. The concentration of $[Fe(CN)_6]^{3-}$ and KCl were kept constant and the ratio Ni^{2+}/Fe^{3+} was changed. Magnetic stirring was used to decrease the mass-transport effect during the deposition. During the deposition at room temperature, a bluish thin film formed on the substrate is noted.

Table 1. Experimental parameters of the metal-cyanide thin film electrodepositions

solutions	Ni^{2+} (mM)	Fe^{3+} (mM)	$[Fe(CN)_6]^{3-}$ (mM)	KCl M
NiFeHCF	0.8	0.8	1.6	1
FeHCF	-	1.6	1.6	1
NiHCF	1.6	-	1.6	1
NiFeOx	0.8	2.4	-	1

Figure 6.1 shows the CV collected for the Prussian blue analogue deposited on FTO substrate. The onset potential for PB was 1.6 V_{RHE} and the overpotential of 0.72 V_{RHE} at 10 $mA.cm^{-2}$. The NiHCF had an onset of 1.5 V_{RHE} and overpotential of 0.57 V_{RHE}, as can

be seen in Figure 6.1b. In this same Figure, there is an oxidation peak attributed to Ni^{2+}/ Ni^{3+} at 1.4 V_{RHE}. The NiFeHCF presented better results with potential onset of 1.45 V_{RHE} and overpotential of 0.48 V_{RHE} at 10 $mA.cm^{-2}$. As can be seen in Figure 6.1c the oxidation peak had an anodic shift compared to the Figure 6.2b. This shift has been attributed to the oxidation of Fe^{3+} to Fe^{4+}.[21] The Ni^{2+}/Fe^{3+} without $[Fe(CN)_6]^{3-}$ was also deposited on the FTO using the same electrochemical condition. However, the anode did not have a significant decrease of the OER overpotential compared to bare FTO.

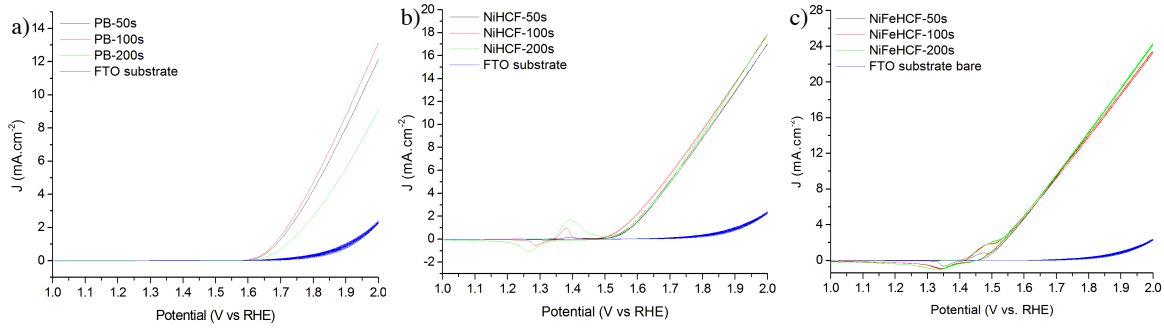

Figure 6.1 Linear sweep voltammograms of electrocatalyst deposited on FTO substrate. a) PB deposited, b) NiHCF and c) $Ni_{1-x}Fe_xHCF$.

A comparison of these CVs can be seen in Figure 6.2a. It is evident that the electrocatalyst ($Ni_{1-x}Fe_xHCF$) favor the OER by 500 mV compared with bare FTO. The overpotentials at 10 $mA.cm^{-2}$ for FeHCF and NiHCF were 0.72 and 0.59 V_{RHE}, respectively. The NiFeHCF had overpotential of 0.48 V_{RHE} at 10 $mA.cm^{-2}$.

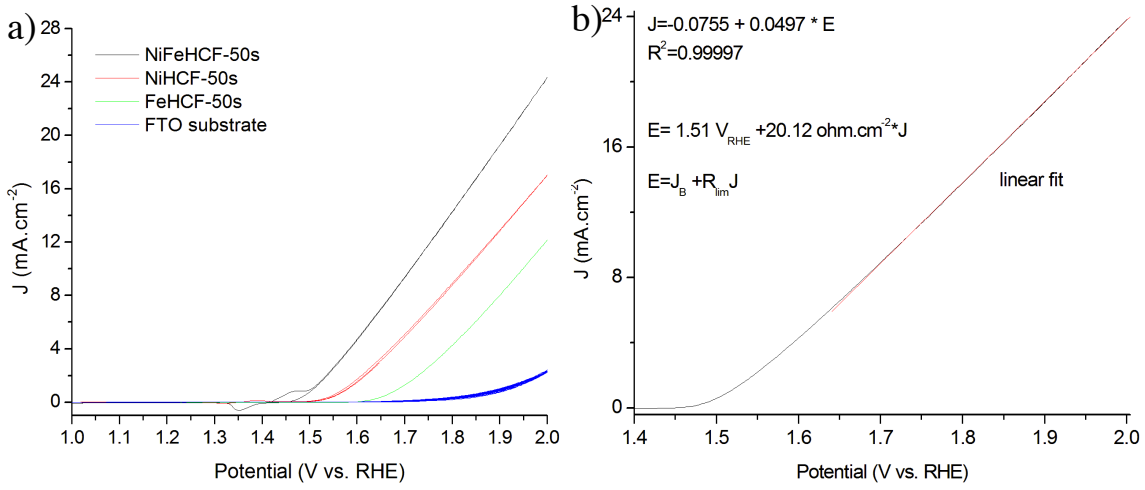

Figure 6.2 Comparative voltammograms of catalyst deposited on the FTO. a) Optimized J vs. V_{RHE} for $Ni_{1-x}Fe_xHCF$, NiHCF and FeHCF. b) Resistive behavior of the electrocatalyst on the FTO substrate.

Despite the good stability of this electrocatalyst deposited on the FTO substrate, a linear current is observed in the Figure 6.2b. This linear current has resistive behavior and does not obey the Butler-Volmer model. This kind of resistive kinetics is commonly observed in electrode with high current that is limited by electrolyte or electrode resistance, R_{Ω}. In this case, this linear behavior is due to the sheet resistance of the FTO substrate (15 Ω/□). A linear regression from linear sweep can give two kinetic parameters to describe the OER. The inset of Figure 6.2b shows an equation where E and J represent the potential and the current density respectively. The R_{lim} and J_b are the resistive kinetic parameters. The R_{lim} had a value of 20 $\Omega.cm^2$ that represent the FTO sheet resistance and J_b had 1.51 V_{RHE}.

SEM images in Figure 6.3 show the NiFeHCF deposited on the FTO substrate. Figure 6.3a shows a crack that highlights the FTO from the electrocatalyst. It is more evident in Figure 6.3b where a pellicle of the NiFeHCF can be seen. Figure 6.3c shows only the FTO substrate.

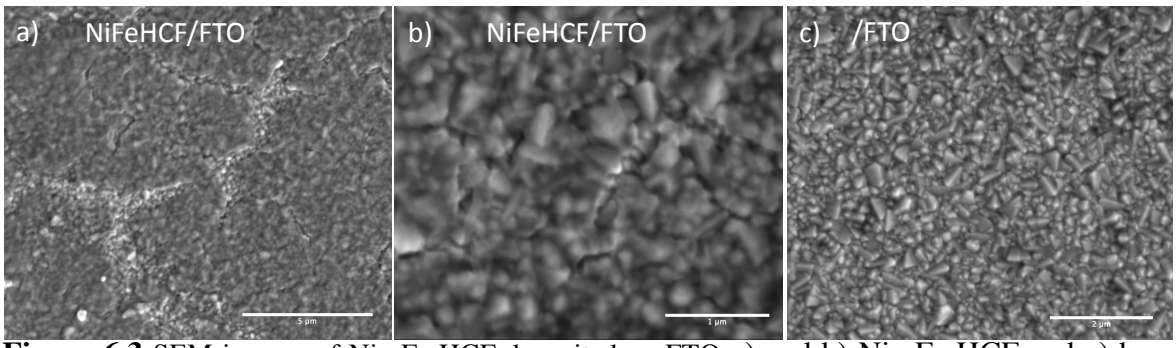

Figure 6.3 SEM images of $Ni_{1-x}Fe_xHCF$ deposited on FTO a) and b) $Ni_{1-x}Fe_xHCF$ and c) bare FTO.

To better take advantage of this electrocatalyst, another substrate was selected to deposit the NiFeHCF under optimized condition. For this deposition, a palladium foil was selected as substrate due to the high OER overpotential of this substrate. The overpotential of the NiFeHCF deposited on the palladium foil was 0.28 V_{RHE} at 10 $mA.cm^{-2}$. Obviously, palladium is more conductive than FTO and in this case the OER follows the Butler-Volmer kinetics, as can be observed in the exponential growth of current shown in Figure 6.4. Figure 6.4c highlights the oxidation peak of Ni^{2+} to Ni^{3+} around 1.45 V_{RHE}.

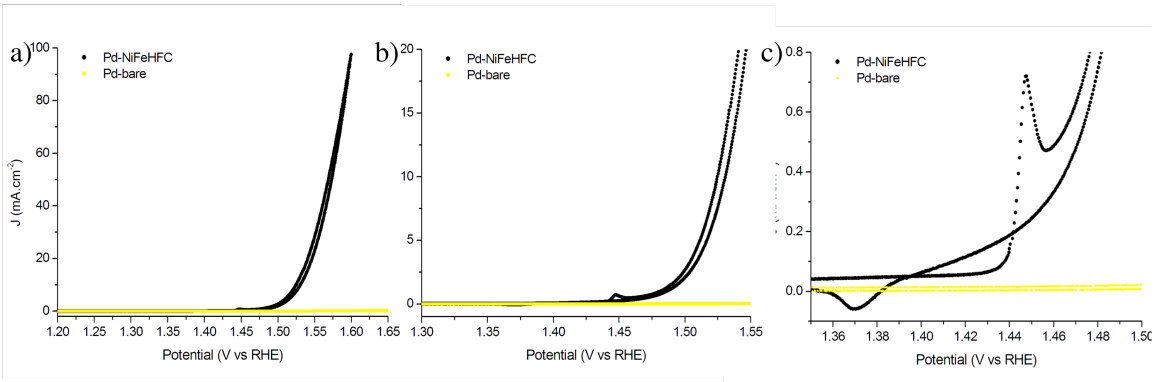

Figure 6.4 $Ni_{1-x}Fe_xHCF$ deposited on a palladium substrate. a) CV from 1.2 to 1.65 V_{RHE} b) CV from 1.3 to 1.55 V_{RHE}, c) oxidation peak enhanced.

SEM images in Figure 6.5 show the NiFeHCF deposited on the palladium foil. The low magnification SEM image in Figure 6.5a shows that this catalyst was homogeneously deposited on the foil. The same pellicle observed on the FTO substrate was detected on the palladium foil, as can be seen in Figure 6.5b.

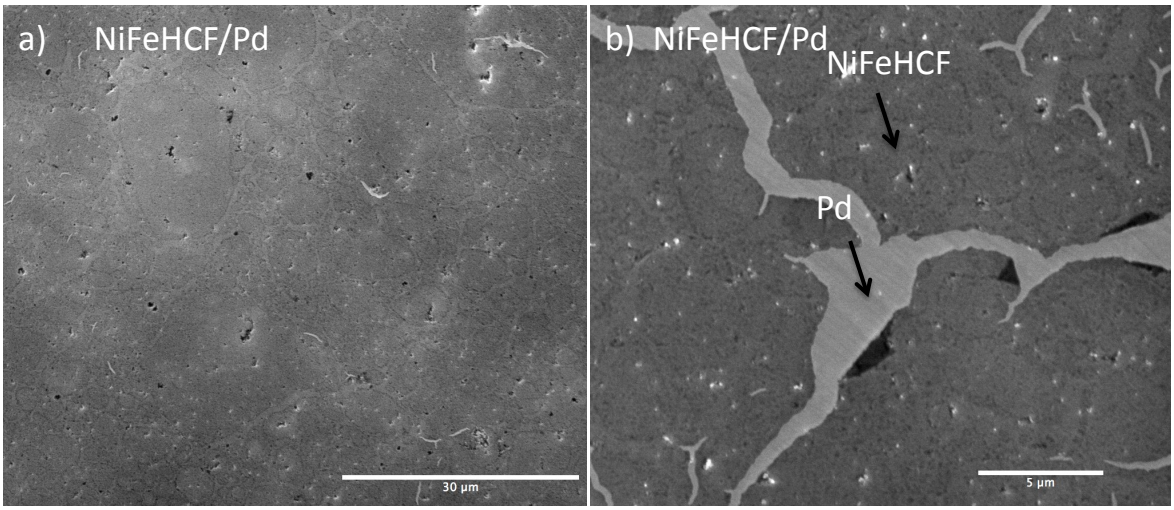

Figure 6.5 SEM images of $Ni_{1-x}Fe_xHCF$ deposited on palladium substrate. a) Homogenous thin film of $Ni_{1-x}Fe_xHCF$ b) crack on the thin film.

Figure 6.6 shows a chronopotentiometric measurement with excellent stability over 2 hours for this electrocatalyst on the palladium foil. This result indicates that the catalyst has also excellent adhesion to the substrate, with the fast elimination of oxygen bubbles from the surface. The palladium foil has good performance as substrate. Therefore, it is important to mention that the palladium foil was used as substrate only to study the performance of this electrocatalyst.

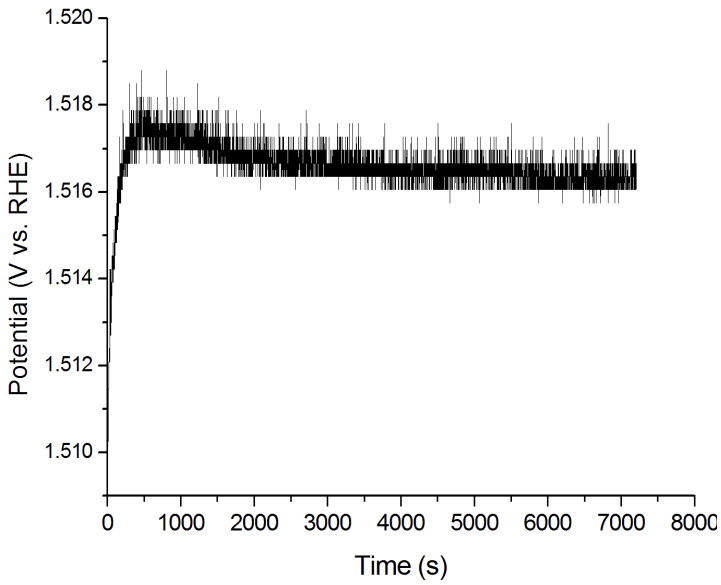

Figure 6.6 Chronopotentiometry of $Ni_{1-x}Fe_xOOH$/palladium foil at 10 $mA.cm^{-2}$.

The Raman spectra of the anode before OER showed the peak of cyanide group from 2050 to 2200 cm^{-1}. However, after OER this same peak showed an expressive decrease of intensity. A possible reasonable explanation for this decrease is the exchange of cyanide to hydroxyl group.

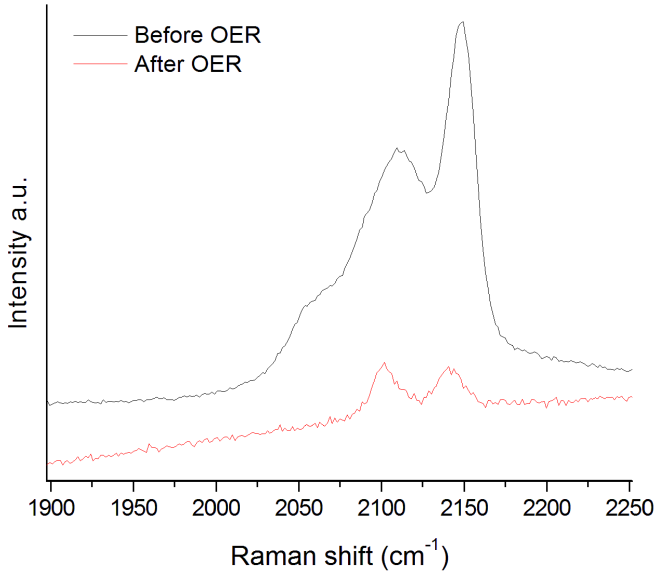

Figure 6.7 Raman spectroscopy analysis of electrocatalyst before and after OER.

Unfortunately, most conductive supports are metals, such as nickel, iron, titanium and alloys. These metallic anodes can also be oxidized to form an isolating layer that considerably increases the overpotential. Pyrolitic graphite substrates can be an excellent

alternative as conductive substrate for anode. The PGS patented by Panasonic has conductivity around 20 $kS.cm^{-1}$. PGS also is flexible and resistant to corrosion and mainly has low cost. Here, the main strategy was to use PGS as substrate to deposit the $Ni_{1-x}Fe_xOOH$, instead using palladium or other metal as substrate.

Figure 6.7a shows cyclic voltammetry for $Ni_{1-x}Fe_xOOH$ on PGS substrate. Apparently, the curves show noises due to the oxygen bubble generation. In the first experiment, the PGS substrate did not show good results as observed to the palladium foil. The hypothesis for this low performance was the hydrophobic surface of PGS. Thus, the first strategy to make PGS hydrophilic was the electrochemical oxidation of the PGS surface. In sulfuric acid and anodic potential, the PGS surface is oxidized to C^+SO_4. During the electrochemical oxidation the surface of PGS becomes blue which is characteristic of graphite-bisulfate. The surface becomes more hydrophilic due to the change of sulfate to hydroxyl group. After this electrochemical oxidation, the $Ni_{1-x}Fe_xHCF$ was deposited on the PGS-bisulfate and a new experiment of OER was carried out. Figure 6.7b shows voltametry curves and it is evident that the hydrophilic surface has improved the performance of the electrocatalyst on the PGS. The overpotential at 10 $mA.cm^{-2}$ was 0.33 V_{RHE} for the hydrophobic PGS and 0.29 V_{RHE}.

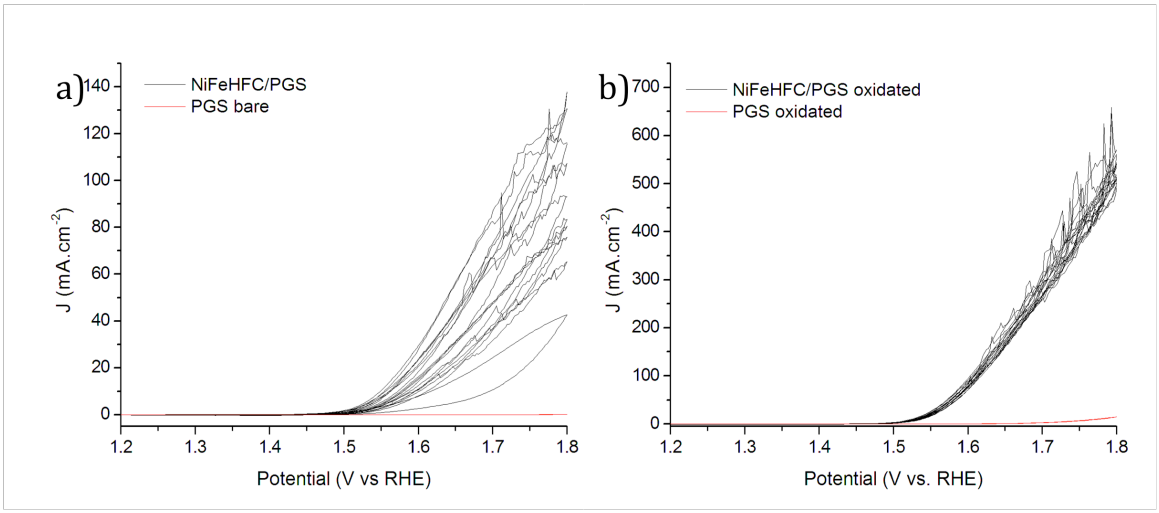

Figure 6.8 $Ni_{1-x}Fe_xHCF$ deposited on PGS. a) Unoxidazed PGS b) PGS-bisulfate.

Figure 6.9 shows top-view SEM images of the electrocatalyst deposited on the PGS. The pellicle of $Ni_{1-x}Fe_xHCF$ is evident in Figure 6.9c and apparently shows a homogeneous distribution on the surface of this support. Figure 6.9a shows only the bare PGS. The elemental analysis was also performed to determinate the presence of nickel and iron. EDS maps is showed in Figure 6.9. Nickel and iron were detected as well as the

oxygen. It is important to mention that these elements were homogeneously mapped on the surface.

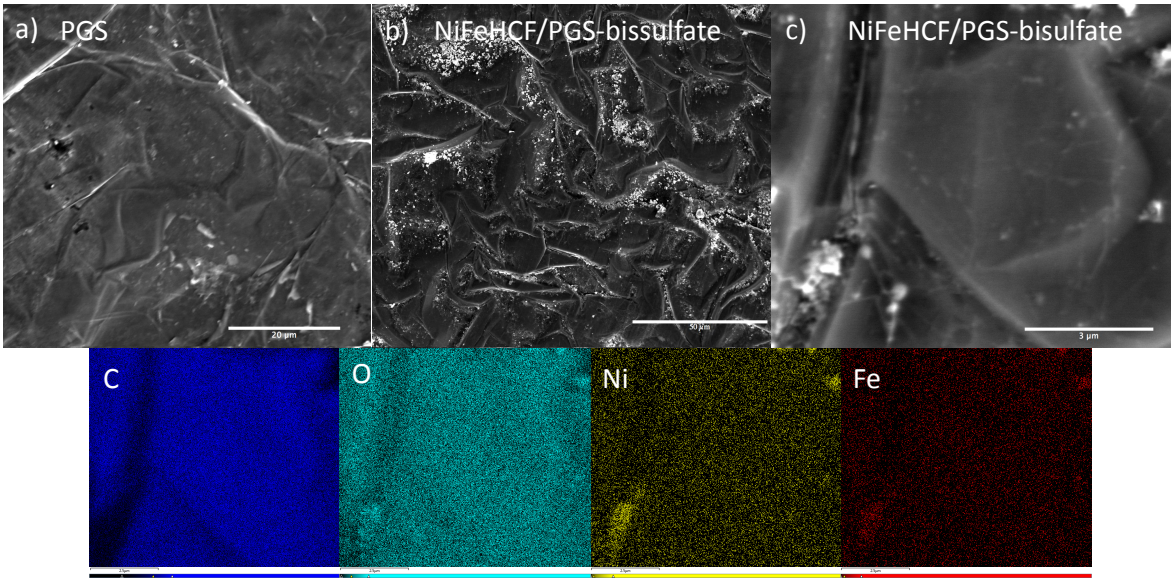

Figure 6.9 SEM images of $Ni_{1-x}Fe_xHCF$ deposited on PGS-bisulfate. a) bare PGS, b) and c) $Ni_{1-x}Fe_xHCF$ /PGS-bisulfate. EDS map image corresponds to the SEM image c).

This electrocatalyst was also deposited on a hematite thin film. Firstly, a thin layer of 20 nm of hematite was deposited on the PGS-SO_4. This layer was produced via the CND process described in chapter 4. After that, the $Ni_{1-x}Fe_xHCF$ was deposited on Fe_2O_3/PGS following the optimized conditions for the FTO substrate. The voltammetric curve in Figure 6.10a shows a significant change of the OER overpotential oand an exponential behavior of the current density. The overpotential shift was 200 mV compar to the Fe_2O_3/PGS without the electrocatalyst. Figure 6.10c shows photographies of PGS and PGS-SO_4.

A thin layer of hematite was also deposited on FTO substrate, under the same condition. Figure 6.10b shows a change for the better on onset of the electrocatalyst deposited on the hematite thin film. The overpotential at 1 $mA.cm^{-2}$ had a shift of 200 mV compared to hematite deposited on the FTO.

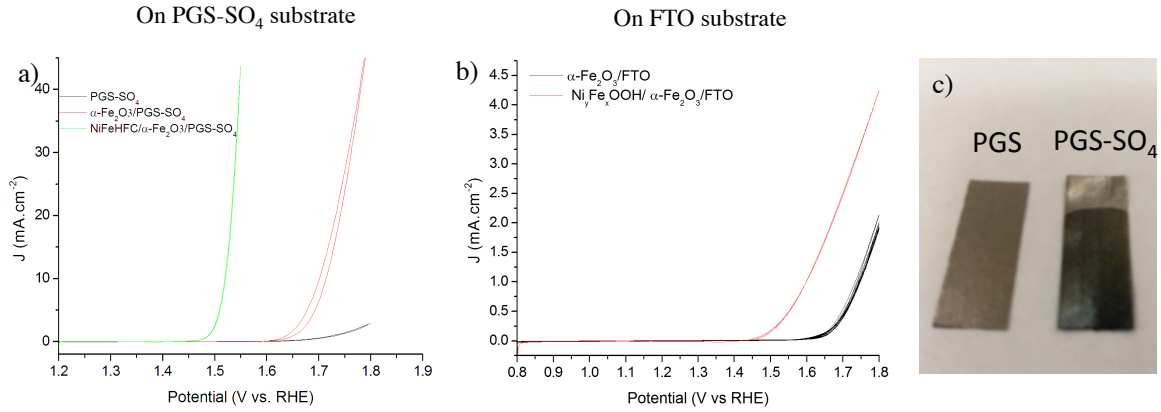

Figure 6.10 Voltametric curves of $Ni_{1-x}Fe_xHCF$ deposited on a) PGS-bisulfate and b) FTO substrate, c) photograph of PGS-bisulfate.

The chronopotentiometric analysis for the electrocatalyst deposited on the α-Fe_2O_3/PGS in Figure 6.11 has showed excellent performance and can be compared to the electrocatalyst deposited on the palladium foil.

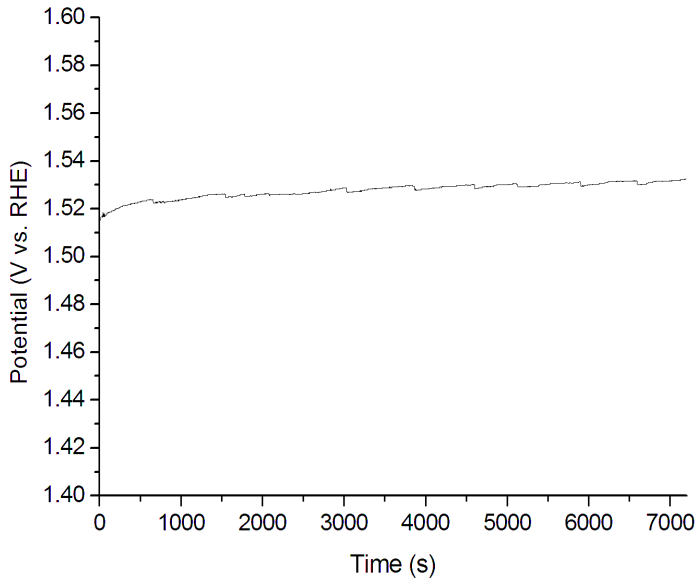

Figure 6.11 Chronopotentiometry of $Ni_{1-x}Fe_xOOH$/PGS-bisulfate at 10 $mA.cm^{-2}$.

6.4 Conclusions

The $Ni_{1-x}Fe_xOOH$ obtained via electrochemical deposition of Prussian Blue analogue had an overpotential at 10 $mA.cm^{-2}$ lower than to electrocatalyst frequently reported. According with the deep revision, this electrochemical strategy to deposit this electrocatalyst has not been published yet. The first approach to deposit the electrocatalyst on the FTO did not show good results in terms of high current due to the electrical resistance of this substrate. In the other hand, the palladium foil has demonstrated as an excellent substrate due to the low overpotential and electrochemical stability. The PGS with the surface oxidized also demonstrated a good performance in term of overpotential and stability.

6.5 References

1. Walter, M. G.; Warren, E. L.; McKone, J. R.; Boettcher, S. W.; Mi, Q.; Santori, E. A.; Lewis, N. S. Solar Water Splitting Cells. *Chem. Rev*. 110, 6446–6473, **2010**.

2. Rossmeisl, J.; Qu, Z. W.; Zhu, H.; Kroes, G. J.; Norskov, J. K. Electrolysis of Water on Oxide Surfaces. *J. Electroanal. Chem*. 607, 83– 89, **2007**.

3. Hall, D. E. Impregnated Anodes for Alkaline Water Electrolysis. *J. Electrochem. Soc*. 130, 317– 321, **1983**.

4. Li, X. H.; Walsh, F. C.; Pletcher, D. Nickel based electrocatalysts for oxygen evolution in high current density, alkaline water electrolyzers. *Phys. Chem. Chem. Phys*. 13, 1162–1167, **2011**.

5. Matsumoto, Y.; Sato, E. Electrocatalytic Properties of Transition Metal Oxides for Oxygen Evolution Reaction. *Mater. Chem. Phys*. 14, 397, **1986**.

6. Trasatti, S. Electrocatalysis by Oxides - Attempt at a Unifying Approach. *J. Electroanal. Chem.,* 111, 125– 131, **1980**.

7. Yagi, M.; Tomita, E.; Kuwabara, T. Remarkably High Activity of Electrodeposited IrO_2 Film for Electrocatalytic Water Oxidation. *J. Electroanal. Chem*. 579, 83– 88, **2005**.

8. Trotochaud, L.; Young, S. L.; Ranney, J. K.; Boettcher, S.W. Nickel–Iron Oxyhydroxide Oxygen-Evolution Electrocatalysts: The Role of Intentional and Incidental Iron Incorporation. *J. Am. Chem. Soc*., 136, 6744–6753, **2014**.

9. A. Harriman, I.J. Pickering, J.M. Thomas, P.A. Christensen. Metal oxides as heterogeneous catalysts for oxygen evolution under photochemical conditions. *J. Chem. Soc. Faraday Trans.*, 184 2795, **1988**.

10. Trotochaud, L.; Ranney, J. K.; Williams, K. N.; Boettcher, S. W. Solution-Cast Metal Oxide Thin Film Electrocatalysts for Oxygen Evolution. *J. Am. Chem. Soc.* 134, 17253– 17261, **2012**.

11. Gong, M.; Li, Y. G.; Wang, H. L.; Liang, Y. Y.; Wu, J. Z.; Zhou, J. G.; Wang, J.; Regier, T.; Wei, F.; Dai, H. J. An Advanced Ni-Fe Layered Double Hydroxide Electrocatalyst for Water Oxidation. *J. Am. Chem. Soc.* 135, 8452– 8455, **2013**.

12. Wendt, H.; Plzak, V. Electrocatalytic and thermal activation of anodic oxygen- and cathodic hydrogen-evolution in alkaline water electrolysis. *Electrochim. Acta* 28, 27– 34, **1983**.

13. Dinca, M.; Surendranath, Y.; Nocera, D. G.Nickel-Borate Oxygen-Evolving Catalyst that Functions under Benign Conditions. *Proc. Natl. Acad. Sci. U.S.A.* 107, 10337– 10341, **2010**.

14. Miller, E. L.; Rocheleau, R. E. Electrochemical behavior of reactively sputtered iron-doped nickel oxide. *J. Electrochem. Soc.* 144, 3072, **1997**.

15. Corrigan, D. A. The catalysis of the oxygen evolution reaction by iron impurities in thin film nickel oxide electrodes. *J. Electrochem. Soc.*, 134, 377, **1987.**

16. Corrigan, D. A.; Bendert, R. M. Effect of Coprecipitated Metal Ions on the Electrochemistry of Nickel Hydroxide Thin Films: Cyclic Voltammetry in 1M KOH. *J. Electrochem. Soc.*, 136, 723, **1989.**

17. Singh, R.; Pandey, J.; Anitha, K. Preparation of Electrodeposited Thin Films of Nickel-Iron Alloys on Mild Steel for Alkaline Water Electrolysis. Part I: Studies on Oxygen Evolution. *Int. J. Hydrogen Energy* 18, 467– 473, **1993**.

18. Louie, M. W.; Bell, A. T.An Investigation of Thin-Film Ni-Fe Oxide Catalysts for the Electrochemical Evolution of Oxygen. *J. Am. Chem. Soc.* 135, 12329– 12337, **2013**.

19. Oliva, P.; Leonardi, J.; Laurent, J. F.; Delmas, C.; Braconnier, J. J.; Figlarz, M.; Fievet, F.; de Guibert, A.Review of the Structure and the Electrochemistry of Nickel Hydroxides and Oxy-Hydroxides. *J. Power Sources* 8, 229– 255, **1982.**

20. de Tacconi, N. R.; Rajeshwar, K.; Lezna, R. O. Metal Hexacyanoferrates: Electrosynthesis, i*n Situ* Characterization, and Applications. *Chem. Mater.* 15, 3046– 3062, **2003**.

21. Chen, J. Y. C.; Dang, L.; Liang, H.; Bi, W.; Gerken, J. B.; Jin, S.; Alp, E. E.; Stahl, S. S. Operando Analysis of NiFe and Fe Oxyhydroxide Electrocatalysts for Water Oxidation: Detection of Fe^{4+} by Mössbauer Spectroscopy. *J. Am. Chem. Soc.*, 137, 48, **2015**.

Chapter 7. Conclusions and Outlook

7.1 General Conclusions

CND process is a promising route to produce thin film dedicated to photoelectrochemistry. The number of publication and citation in this field and specially related with hematite photoanode is considerably increasing. It has showed that this field has an emergent impact on the technology. It is important to mention that there are few researches group in the world that has highlighted with outstanding results and innovative strategy to obtain hematite photoanode. Our group has short experience periods in this field. However, we are working insistently to optimize the experimental parameter of CND process to become also a reference in this field. We reported a different approach to doping or grain growth control of hematite adding tin butoxide on the colloidal nanocrystals. This strategy also had an impact on the performance of photoanode. In addition, the ferrofluid behavior of this colloid has also relevant properties that permit to deposit thin film in large area and control the thickness, using the external magnetic field.

Study of new electrocatalyst for OER has been an important contribution in this field. The most efficient electrocatalyst are produced with noble metals, such as iridium, ruthenium and platinum. In practice, this electrocatalyst should be produced with abundant elements in the earth and low cost of manufacturing. The combination of photoanode and electrocatalyst can increase the solar-to-hydrogen conversion efficiency.

The advance of the characterization techniques also is doing relevant contribution to design and understand the chemical properties of these materials. Chemical analysis and *in situ* electron microscopy can provide time-resolved experiments to give detailed information.

7.2 Future directions

The photocurrent of hematite photoanode and electrocatalyst reported in the thesis can be compared with the best results of literature. However, it important to highlight that this results is far way of ideal photoresponse expected for this semiconductor oxide. There are many fundamental questions that need to be solved and to become this photoanode commercially attractive to produce hydrogen gas. The first parameter that needs an intense study is the onset of the photocurrent, according the flat band potential for hematite it should be around 0.4 V_{RHE}. However, there is overpotential in this photoanode. The main

strategy to overcome this limitation has been to develop an electrocatalyst. The nickel-iron oxyhydroxide developed in chapter 6 has great perspective to be deposited on the hematite photoanode. It is possible due to the low potential and current applied to deposited Prussian blue analogue. This low potential is necessary to avoid any damage on the hematite thin film. Increase the photocurrent is the second point; an interesting strategy should have control of the grain size during the sintering process. For it, it is necessary to optimize carefully the amount of doping and sintering time.

Finally, the *in situ TEM* technique has showed efficient to understand the fundamental parameters that govern the nanocrystals growth. A systematic studied using this technique should bring important contribution for the electrochemistry field. It is necessary to understand the size effect on the grain kinetic growth. γ-Fe_2O_3 should be synthesized with different size and evaluate the growth process using *in situ* heating experiment. Other different element doping also should be studied, such as Sb and Ti.

Appendix A. Design of the PEC with Large Window

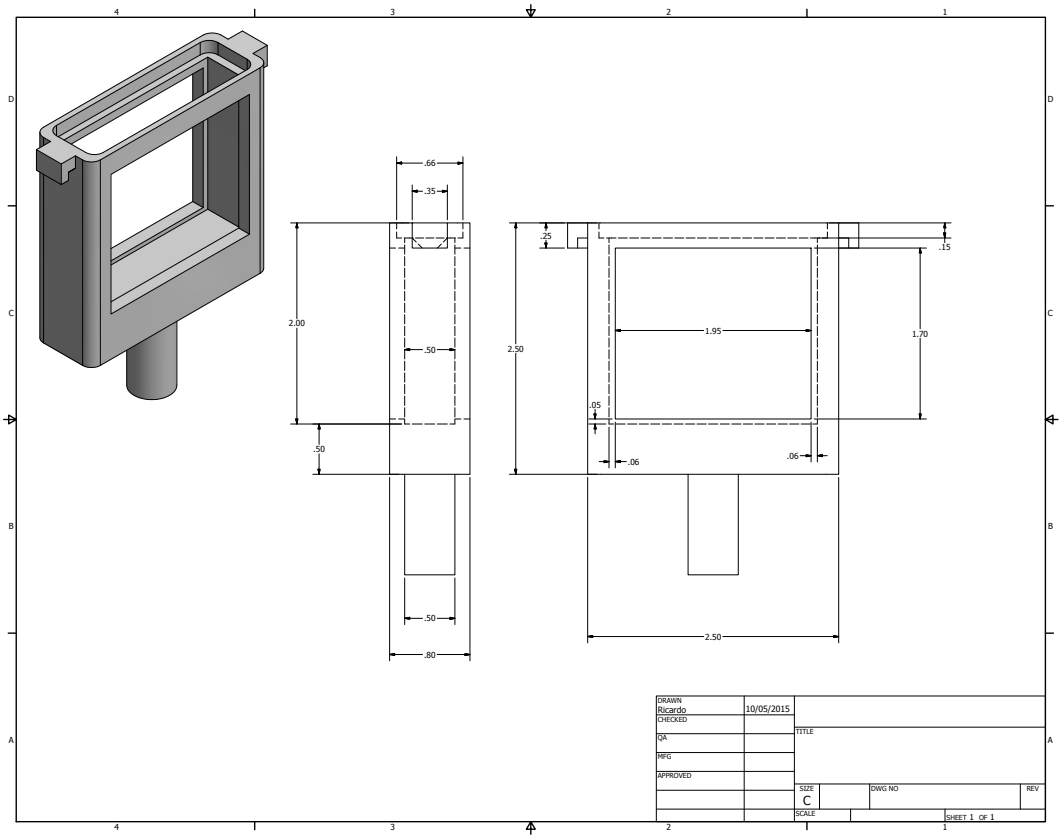

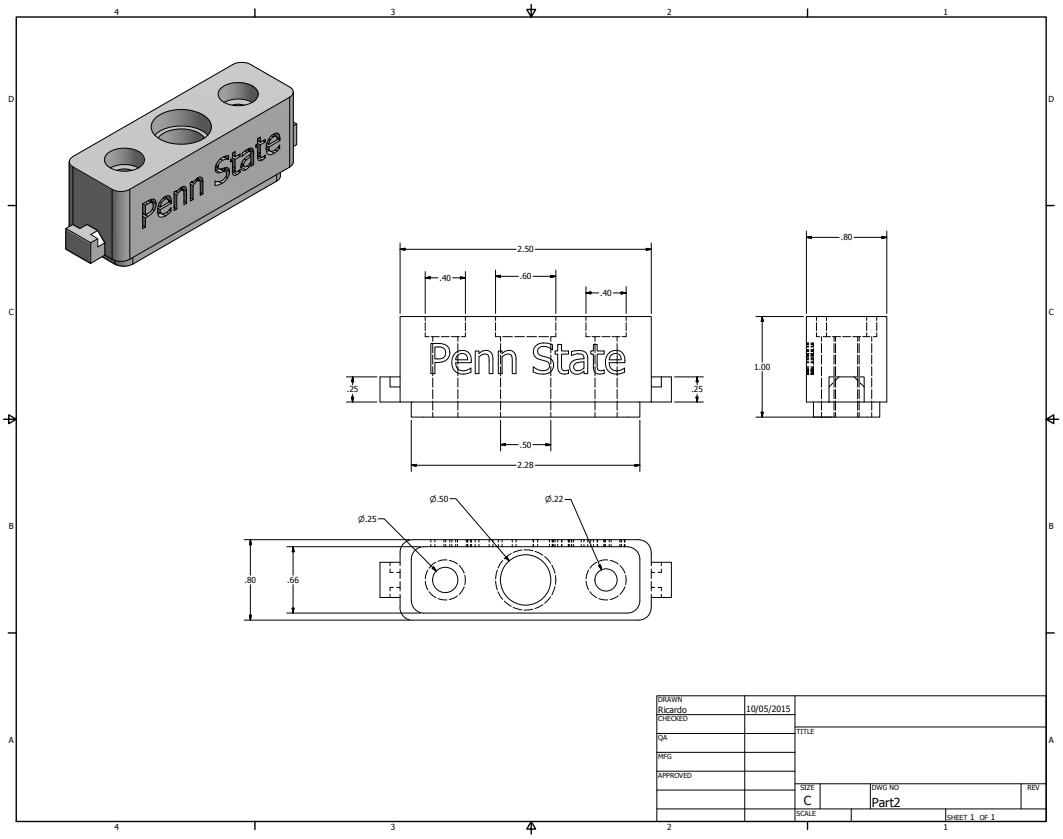

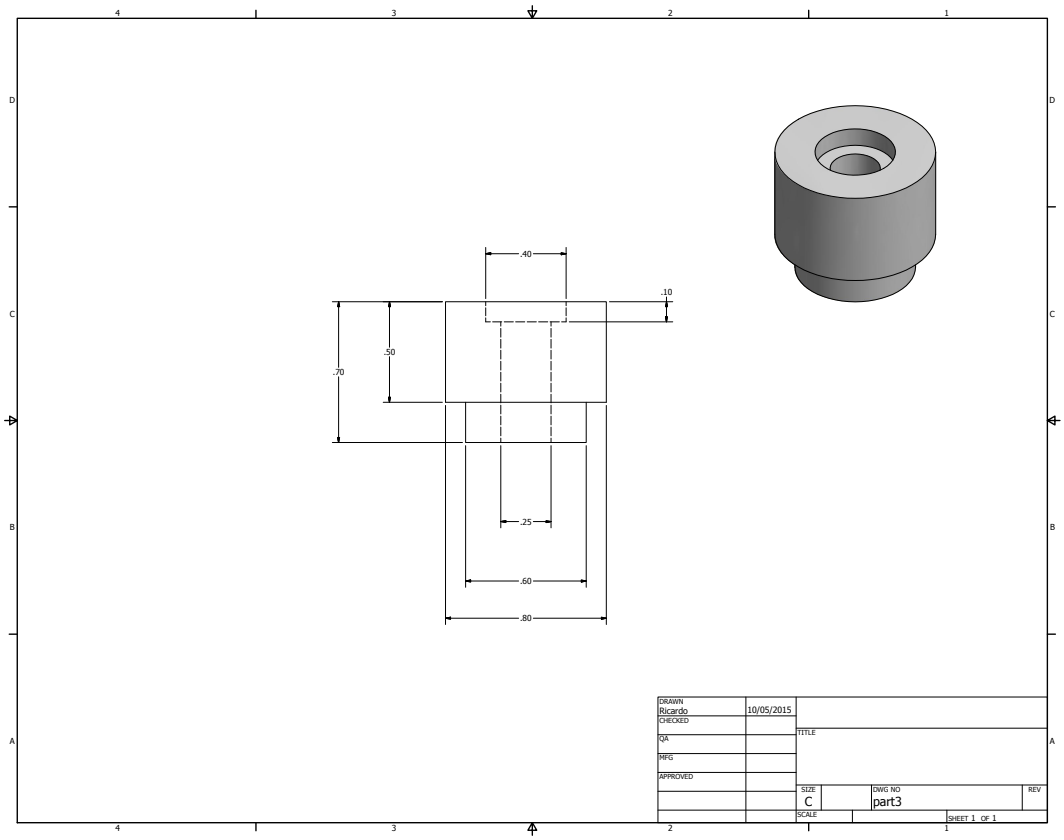
.40
.10
.50
.70
.25
.60
.80
DRAWN
Ricardo
10/05/2015
CHECKED
QA
MFG
APPROVED
TITLE
SIZE
C
DWG NO
part3
REV
SCALE
SHEET 1 OF 1

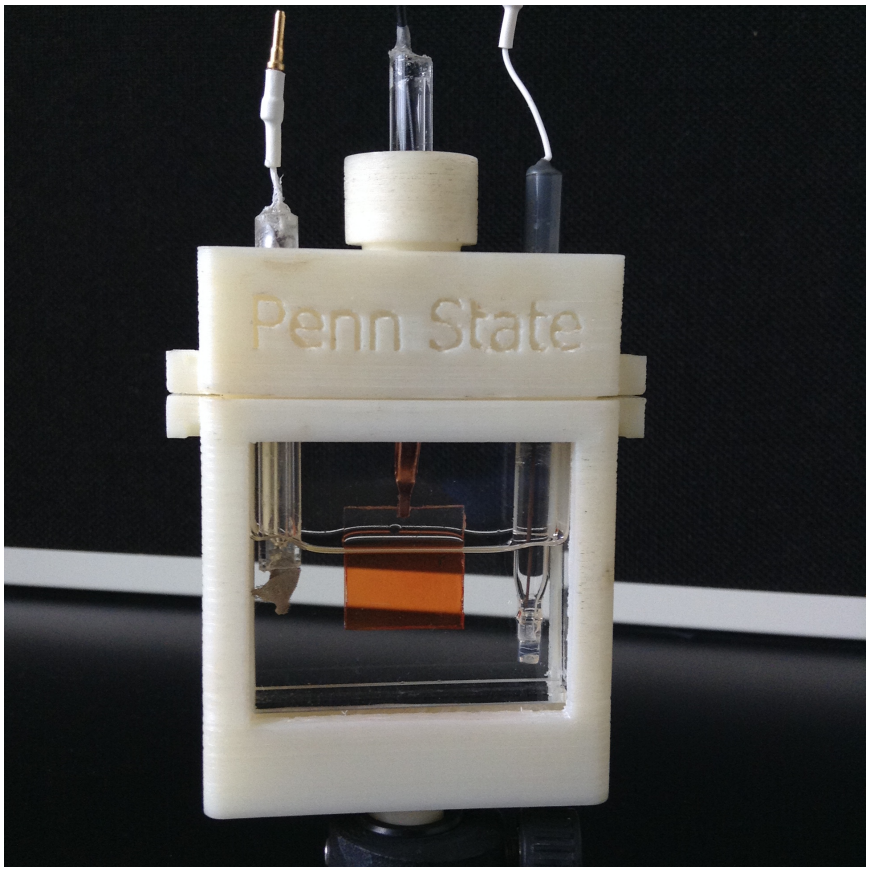
Penn State

Appendix B. Design of a PEC with Small Window

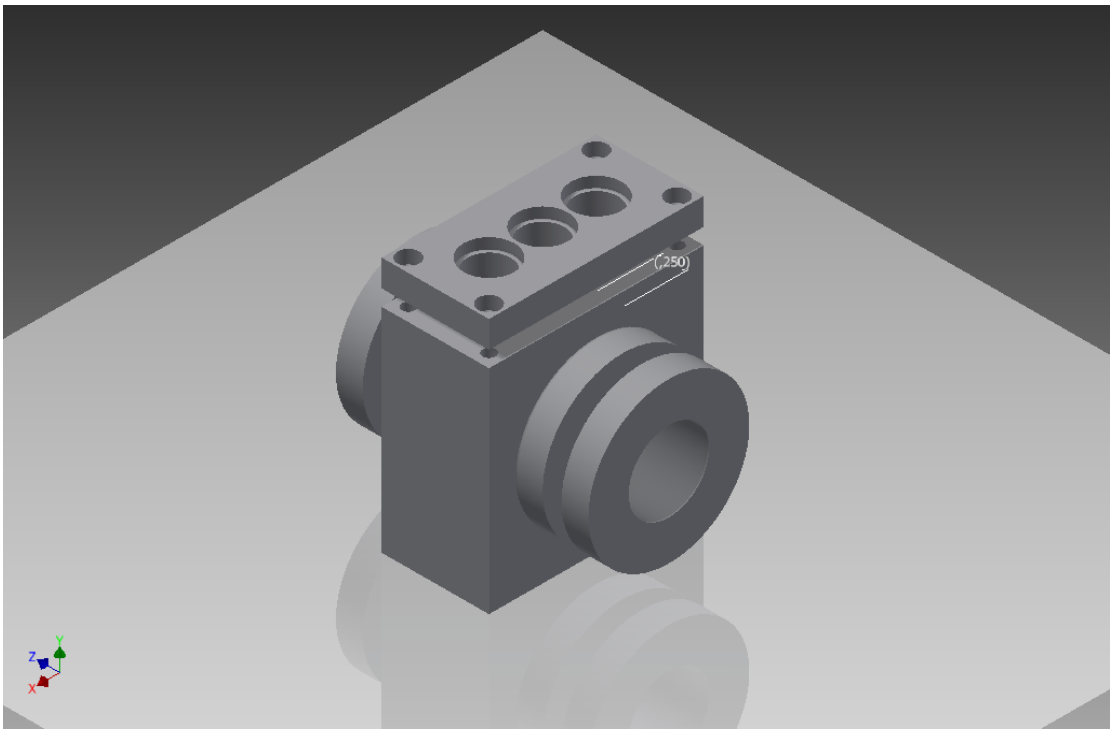

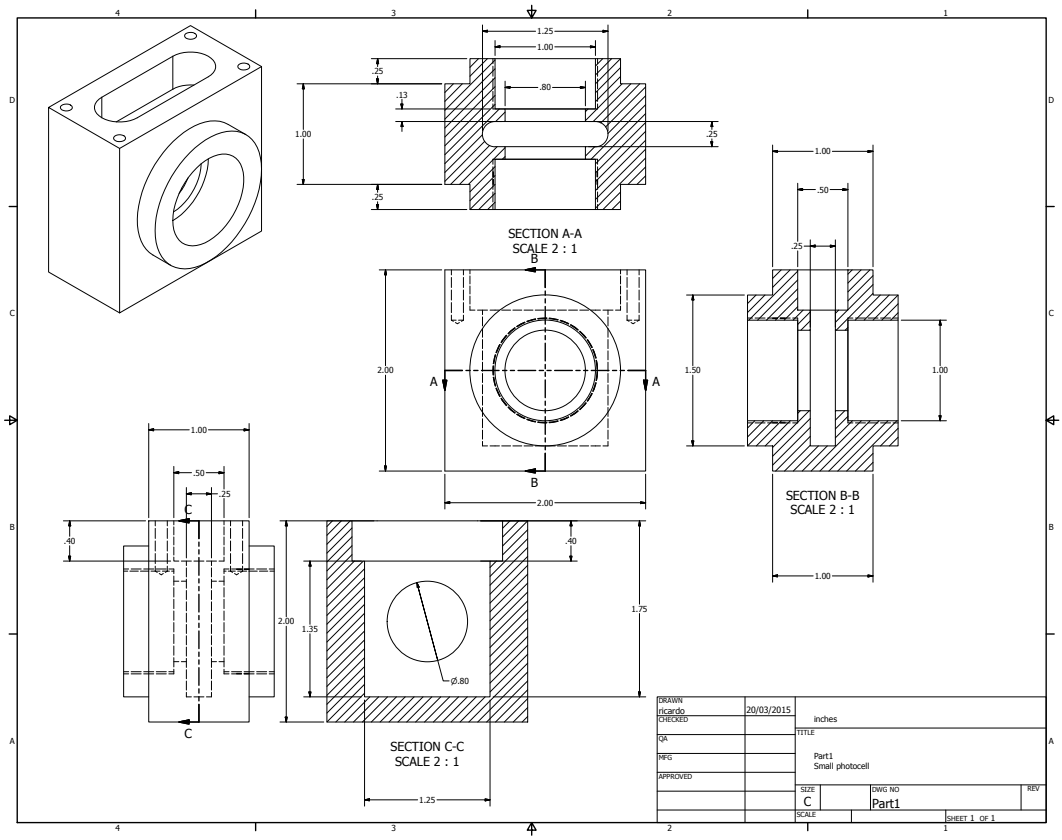

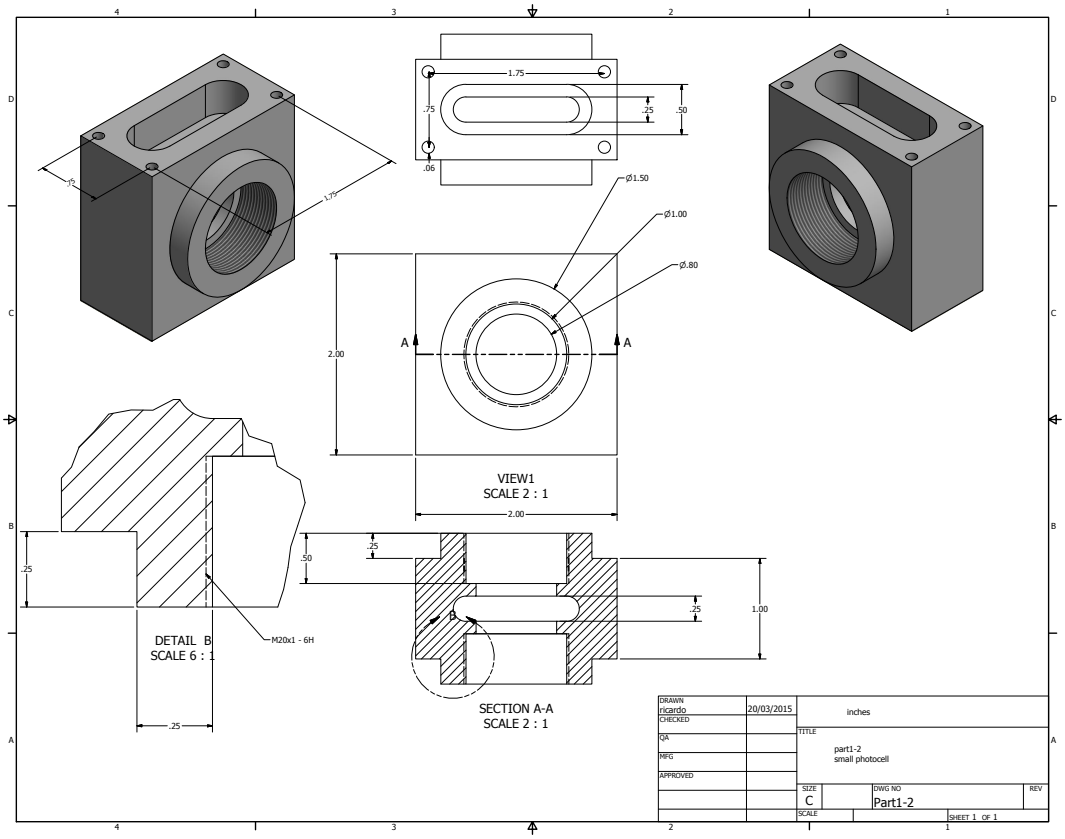
1.75
.75
.25
.50
.06
Ø1.50
Ø1.00
Ø.80
2.00
A
A
VIEW1
SCALE 2 : 1
2.00
.25
.50
.25
.25
1.00
B
DETAIL B
SCALE 6 : 1
M20x1 - 6H
.25
SECTION A-A
SCALE 2 : 1
DRAWN
ricardo
20/03/2015
inches
CHECKED
QA
MFG
APPROVED
TITLE
part1-2
small photocell
SIZE
C
DWG NO
Part1-2
REV
SCALE
SHEET 1 OF 1

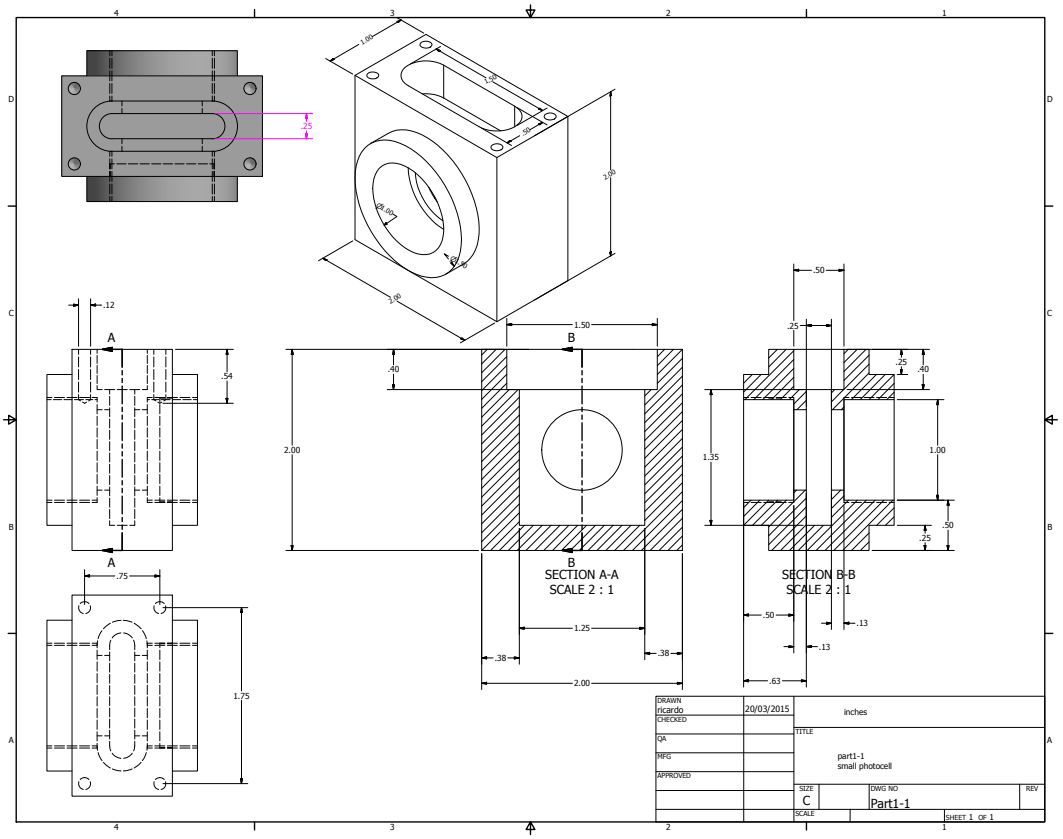
.25
.12
A
.54
A
.75
1.75
1.50
B
.40
2.00
B
SECTION A-A
SCALE 2 : 1
1.25
.38
.38
2.00
.50
.25
.25
.40
1.35
1.00
.50
.25
SECTION B-B
SCALE 2 : 1
.50
.13
.13
.63
DRAWN
ricardo
20/03/2015
inches
CHECKED
QA
MFG
APPROVED
TITLE
part1-1
small photocell
SIZE
C
DWG NO
Part1-1
REV
SCALE
SHEET 1 OF 1

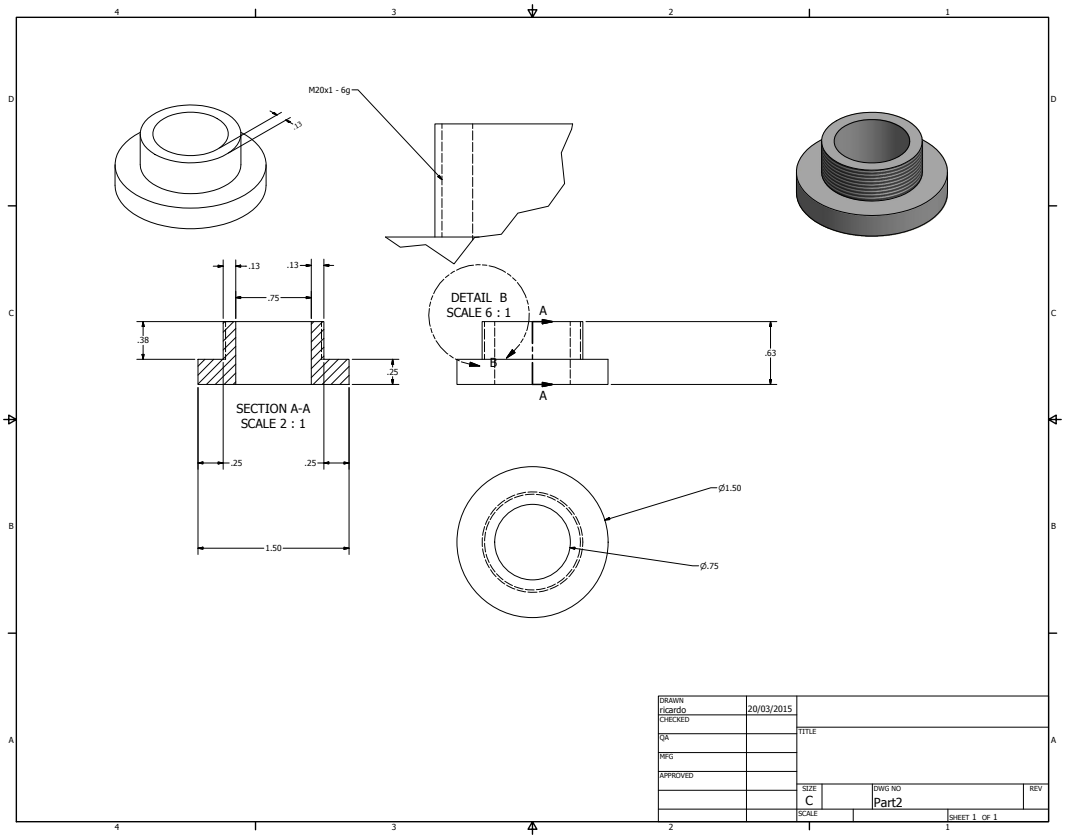
M20x1 - 6g
.13
.13
.75
.38
.25
SECTION A-A
SCALE 2 : 1
.25
.25
1.50
DETAIL B
SCALE 6 : 1
A
B
A
.63
Ø1.50
Ø.75
DRAWN
ricardo
20/03/2015
CHECKED
QA
MFG
APPROVED
TITLE
SIZE
C
DWG NO
Part2
REV
SCALE
SHEET 1 OF 1

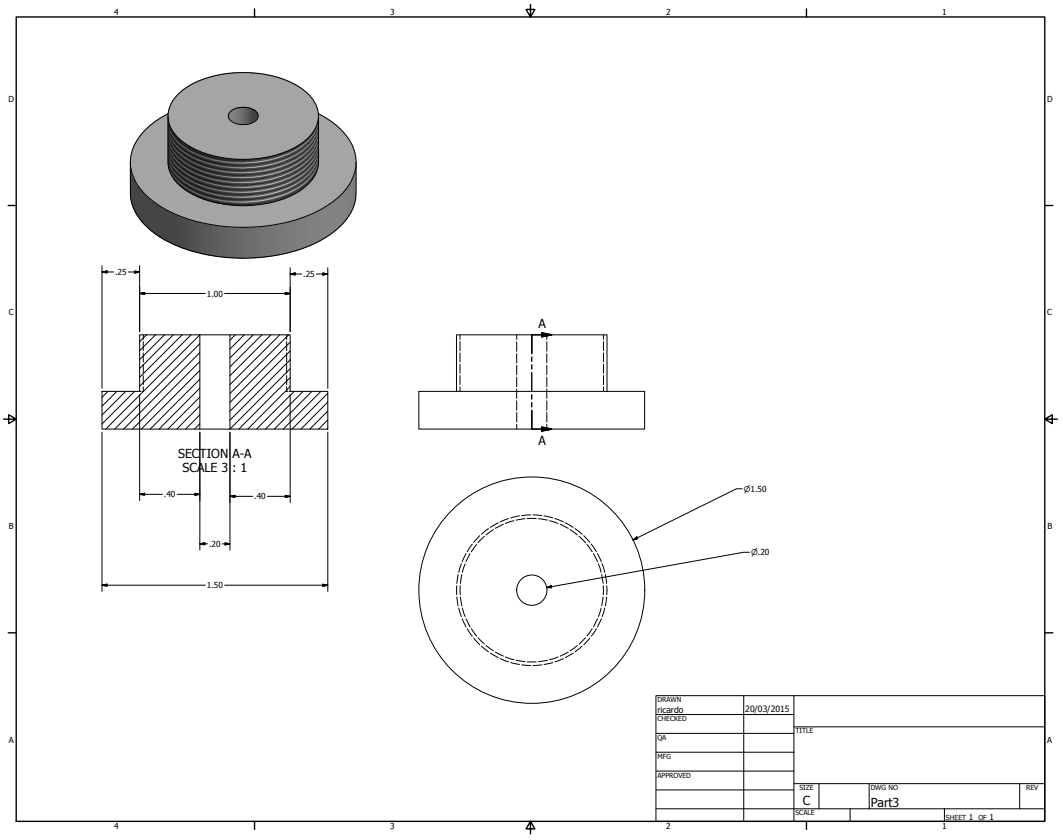
.25
.25
1.00
SECTION A-A
SCALE 3 : 1
.40
.40
.20
1.50
A
A
Ø1.50
Ø.20
DRAWN
ricardo
20/03/2015
CHECKED
QA
MFG
APPROVED
TITLE
SIZE
C
DWG NO
Part3
REV
SCALE
SHEET 1 OF 1

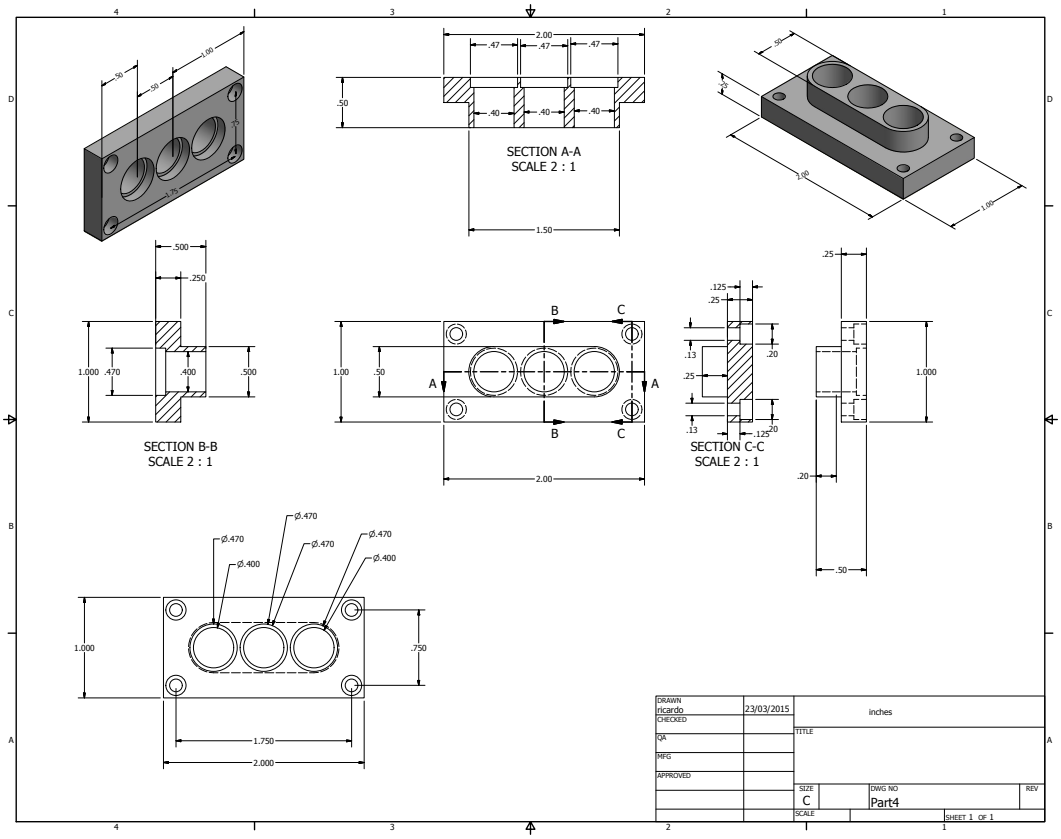
SECTION A-A
SCALE 2 : 1
SECTION B-B
SCALE 2 : 1
SECTION C-C
SCALE 2 : 1
DRAWN
ricardo
23/03/2015
CHECKED
QA
MFG
APPROVED
inches
TITLE
SIZE
C
DWG NO
Part4
REV
SCALE
SHEET 1 OF 1

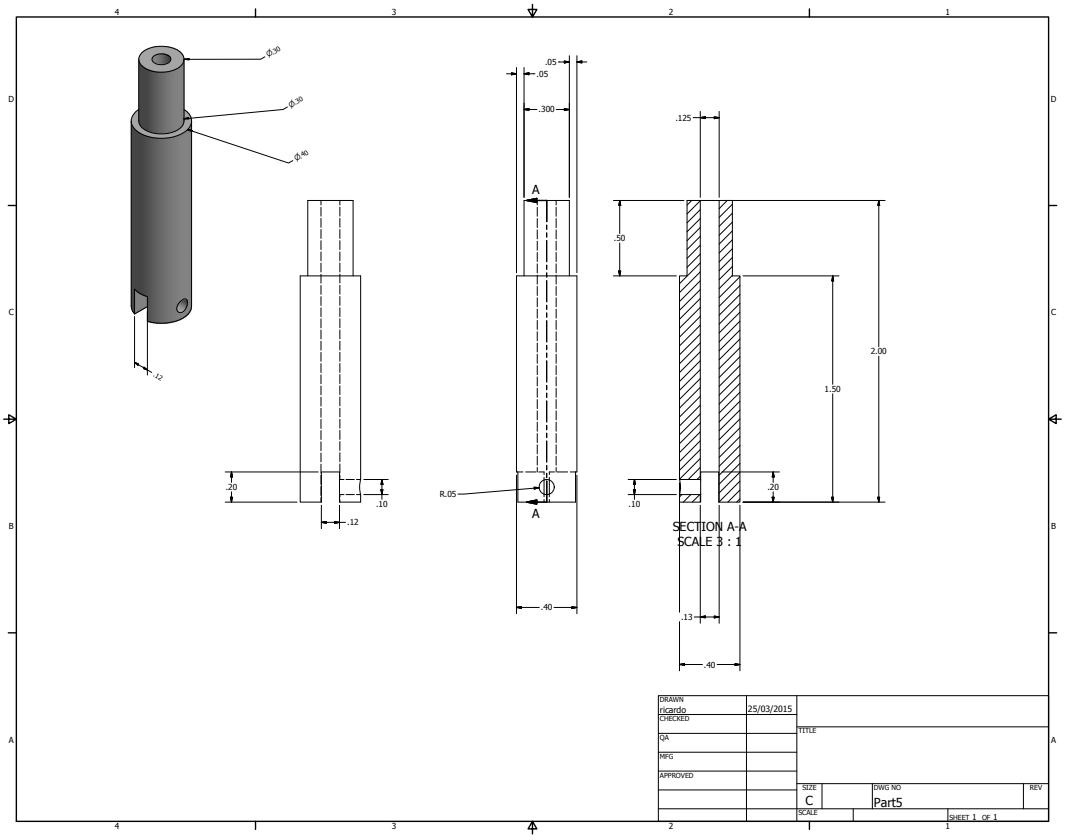
SECTION A-A
SCALE 3 : 1
DRAWN
ricardo
25/03/2015
CHECKED
QA
MFG
APPROVED
TITLE
SIZE
C
DWG NO
Part5
REV
SCALE
SHEET 1 OF 1